

Simulation Models for Exploring Magnetic Reconnection

Michael Shay^{1*}, Subash Adhikari², Naoki Beesho³, Joachim Birn⁴,
Jörg Büchner⁵, Paul Cassak², Li-Jen Chen⁶, Yuxi Chen⁷,
Giulia Cozzani⁸, Jim Drake^{9,10}, Fan Guo¹¹, Michael Hesse¹²,
Neeraj Jain¹³, Yann Pfau-Kempf⁸, Yu Lin¹⁴, Yi-Hsin Liu¹⁵,
Mitsuo Oka¹⁶, Yuri A. Omelchenko^{4,17}, Minna Palmroth⁸,
Oreste Pezzi¹⁸, Patricia H. Reiff¹⁹, Marc Swisdak¹⁰,
Frank Toffoletto¹⁹, Gabor Toth²⁰, Richard A. Wolf¹⁹

^{1*}Bartol Research Institute, Department of Physics and Astronomy,
University of Delaware, Newark, 19716, DE, USA.

²Department of Physics and Astronomy, West Virginia University,
Morgantown, 26506, WV, USA.

³Department of Astronomy, University of Maryland, College Park,
20742, MD, USA.

⁴Center for Space Plasma Physics, Space Science Institute, Boulder,
80301, CO, USA.

⁵Max Planck Institute for Solar System Research, Göttingen, 27077,
Germany.

⁶NASA Goddard Space Flight Center, Greenbelt, 20771, MD, USA.

⁷Center for Space Physics and Department of Astronomy, Boston
University, Boston, 02215, MA, USA.

⁸Department of Physics, University of Helsinki, P.O. Box 68, 00014,
Uusimaa, Finland.

⁹Department of Physics, University of Maryland, College Park, 20740,
MD, USA.

¹⁰Institute for Research in Electronics and Applied Physics, University
of Maryland, College Park, 20740, MD, USA.

¹¹Los Alamos National Laboratory, Los Alamos, 87545, NM, USA.

¹²NASA Ames Research Center, Moffett Field, 94035, CA, USA.

¹³Center for Astronomy and Astrophysics, Technical University Berlin,
Berlin, 10623, Germany.

- ¹⁴Physics Department, Auburn University, Auburn, 36832, AL, USA.
¹⁵Department of Physics and Astronomy, Dartmouth College, Hanover,
03750, NH, USA.
¹⁶Space Sciences Laboratory, University of California, Berkeley, 94720,
CA, USA.
¹⁷Trinum Research Inc., San Diego, 92126, CA, USA.
¹⁸Istituto per la Scienza e Tecnologia dei Plasmi (ISTP), Consiglio
Nazionale delle Ricerche, Bari, I-70126, Italy.
¹⁹Department of Physics and Astronomy, Rice University, Houston,
77005, TX, USA.
²⁰University of Michigan, Ann Arbor, 48109, MI, USA.

*Corresponding author(s). E-mail(s): shay@udel.edu;

Simulations have played a critical role in the advancement of our knowledge of magnetic reconnection. However, due to the inherently multiscale nature of reconnection, it is impossible to simulate all physics at all scales. For this reason, a wide range of simulation methods have been crafted to study particular aspects and consequences of magnetic reconnection. This chapter reviews many of these methods, laying out critical assumptions, numerical techniques, and giving examples of scientific results. Plasma models described include magnetohydrodynamics (MHD), Hall MHD, Hybrid, kinetic particle-in-cell (PIC), kinetic Vlasov, Fluid models with embedded PIC, Fluid models with direct feedback from energetic populations, and the Rice Convection Model (RCM).

1 Introduction

Numerical computation has always played an important role in science. The term “computer” was used during the Renaissance to describe a person who performed mathematical calculations, and such computers were used extensively to calculate the positions of the planets. However, with the advent of digital computers last century, the role of such computation has exploded and revolutionized science in general. The study of magnetic reconnection has seen such a revolution in the last several decades as both numerical power has increased and numerical techniques have become more sophisticated.

Magnetic reconnection is considered a multiscale process because it allows physics that emerges at very small length and time scales to have global consequences in the system. A straightforward example of this large separation of scales is magnetic reconnection on the sun side of Earth’s magnetosphere. In this region, magnetic field lines are finally broken on a length scale of the order of 5 km which is the electron inertial length $d_e \equiv c/\omega_{pe}$. However, the dynamical effects of this breaking of field

lines include driving global convection of the magnetosphere, a system spanning 100s of Earth radii (R_e) which is hundreds of thousands of d_e . A grid scale of $1 c/w_{pe}$ over 100 Earth Radii requires about 100,000 spatial grid points in only 1 dimension. Clearly, accurately resolving the physics breaking the frozen-in constraint while simulating global scales is impossible.

The impossibility of globally simulating the whole 3D system and resolving all scales has led to the generation of a wide range of simulation models, each of which has its own strengths of weaknesses. Through many decades of research, scientists have carefully crafted these models for the particular application or applications they are studying. Typically, the more realistic physics that is included in the simulation, the more computationally expensive it is. Studies of the basic physics of magnetic reconnection (Biskamp, 1996) have very often used kinetic PIC simulations which include all relevant physics, but require a simplified geometry and boundary conditions. Global magnetospheric simulations include the complex boundaries associated with the solar wind and the ionosphere, but until recently were required to be fluid models due to the cost of including kinetic effects.

In this paper we will provide an overview of the primary simulation models that are currently being used to study magnetic reconnection. Please note, however, that the topic of plasma simulation is extremely complex and detailed and cannot be fully covered in a single book, much less a single chapter. If the reader wishes to dive deeper into a particular model, there are many references available, many of which are cited in the individual sections of this paper. There are also excellent books devoted to the subject (e.g., Büchner et al. (2003)).

In the field of magnetic reconnection research, more than one system of units is used. As of this writing, one can generally say that scientists specializing in theory/simulation primarily use cgs units and scientist specializing in observational analysis use SI units. We have chosen as much as possible to use cgs units in this paper, although the chapter on the Rice Convection Model has been left in SI units. For an excellent description on how to convert units between cgs and SI, please see the *NRL Plasma Formulary* (Huba, 1998).

For the organization of the paper, we choose to move generally from fluid models to kinetic models; we start with magnetohydrodynamics (MHD) and gradually increase in physical complexity until reaching fully kinetic simulations. We end with the Rice Convection Model (RCM), a widely used model for the inner magnetosphere, which acts as an inner boundary for magnetic field lines which are reconnecting in the magnetosphere. Section 2 describes MHD. Section 3 describes Hall MHD. Section 4 describes Hybrid Simulations. Section 5 describes kinetic particle-in-cell simulations. Section 6 describes embedding PIC codes into fluid models like MHD. Section 7 describes Kglobal, an MHD model which self consistently evolves energetic particles. Section 8 describes kinetic Vlasov models. And Section 9 describes the Rice Convection Model.

2 MHD

2.1 Equations of MHD

Magnetohydrodynamics (MHD) is the simplest fluid model used to study large scale plasma dynamics. MHD is based on the assumption that the characteristic length and time scales of the system under study are much larger than the length and time scales of the plasma species, usually Debye length (λ_D) or gyroradius and gyroperiod. Therefore, MHD represents the slow evolution of plasmas, often electrons and ions as a single fluid. The macroscopic behavior of the fluid in presence of a magnetic field is described by MHD using hydrodynamics and Maxwell's equations.

Let us consider a fluid (in this case a plasma with ions and electrons), moving with a flow velocity \mathbf{u} , characterized by a mass density $\rho = m_i n_i$ where m_i is the mass of protons ($m_i \gg m_e$) and n_i is the number density of protons (with quasi-neutrality $n_i = n_e = n$), thermal pressure p , and a magnetic field \mathbf{B} . The evolution of these fields in space and time are governed by the MHD equations given by

$$\frac{\partial \rho}{\partial t} = -\nabla \cdot (\rho \mathbf{u}), \quad (1)$$

$$\rho \frac{\partial \mathbf{u}}{\partial t} + \rho (\mathbf{u} \cdot \nabla) \mathbf{u} = -\nabla p + \frac{1}{4\pi} (\nabla \times \mathbf{B}) \times \mathbf{B} + \nu \nabla^2 \mathbf{u}, \quad (2)$$

$$\frac{d}{dt} \left(\frac{p}{\rho^\gamma} \right) = 0, \quad (3)$$

$$\frac{\partial \mathbf{B}}{\partial t} = \nabla \times (\mathbf{u} \times \mathbf{B}) + \frac{\eta c^2}{4\pi} \nabla^2 \mathbf{B}, \quad (4)$$

where γ is the adiabatic index (usually 5/3), ν is the dynamic viscosity, η is the resistivity and $\eta c^2/4\pi$ collectively is known as the magnetic diffusivity. Here Eq. 1 is the continuity equation representing conservation of mass density, Eq. (2) is the momentum conservation equation, Eq. (3) is the simple adiabatic gas equation representing the conservation of energy and Eq. 4 is the induction equation, where the first term on the right is the advection term and the second one represents diffusion. Note, as a result of MHD approximations, the displacement current term is omitted in the induction equation. In an ideal situation, there are no dissipative processes and therefore ν and $\eta = 0$ gives ideal MHD equations. Studies have shown that ideal MHD description is a very good approximation to study dynamical properties of strongly magnetized plasmas.

2.2 Regional MHD Simulations

Several large-scale MHD approaches do not model the entire magnetosphere but only sections of it, such as certain magnetopause regions (dealt with elsewhere in this volume) or the magnetotail. Here we focus particularly on the magnetotail. The basic numerical approach used in regional MHD simulations is essentially similar to that used in (some) global simulations. It is typically based on explicit finite difference methods to solve the MHD equations. Minor differences might exist in adding resistive terms, which are usually necessary in local MHD to initiate reconnection.

The main difference, however, consists of the setup or initialization. Whereas global simulations typically involve a period of interaction with the solar wind to create a realistic magnetotail, local MHD simulations generally start from some equilibrium or near-equilibrium that models the stretched magnetotail (e.g., [Schindler \(1972\)](#)). This approach provides more flexibility in treating different scenarios, for instance, varying the tail flaring between y and z ([Birn and Hesse, 2000](#)) or including a local B_z hump ([Merkin and Sitnov, 2016](#); [Birn et al., 2018](#)). This flexibility has also proven useful in PIC simulations that go beyond the commonly used initial 1D Harris sheet, most notably in addressing the holy grail of reconnection onset (e.g., [Liu et al. \(2014\)](#); see also [Liu et al. \(2024\)](#)).

On the other side, interactions with the ionosphere or the solar wind are incorporated only in some ad hoc fashion, if at all. Regional magnetotail MHD simulations therefore have been most successful in treating dynamic tail phenomena on relatively short time scales that are typically substorm related. The successes include

1. The demonstration that x-line formation and plasmoid ejection can be part of a 2D or 3D tearing-type instability of the tail (e.g., [Birn and Hones Jr \(1981\)](#)).
2. The demonstration that the build-up of the substorm current wedge, involving dipolarization and Region-1-type field-aligned currents ([McPherron et al., 1973](#)), can be due to the braking and azimuthal diversion of earthward flow from a near-tail reconnection site ([Birn and Hesse, 1991](#); [Scholer and Otto, 1991](#)). This basic picture has been modified more recently, most notably by the addition of a Region-2 current system connecting to the ionosphere at lower latitude ([Birn and Hesse, 2014](#); [Kepko et al., 2015](#)), in agreement with observations ([Sergeev et al., 2014](#)). While the buildup of the SCW in the simulations is based on the shear and vorticity of the earthward flow, the persistence of the currents relies on the changes of the magnetic flux and pressure patterns brought about by the severance of a plasmoid and the resulting loss of entropy and redistribution of the pressure. It is noteworthy that these features can be, and have been, found also in global simulations. In the regional simulations, however, they arise as consequences of an instability without involvement of external driving or feedback from the ionosphere. This would be harder to extract from the global simulations.
3. Regional MHD simulations have also been used to address the evolution prior to the onset of reconnection in the tail, demonstrating, specifically, the formation of a thin concentrated current sheet embedded in the near-tail plasma sheet. These approaches have included interaction with the solar wind in two complementary, ad-hoc ways. In one approach magnetic flux is added to the tail lobes ([Birn and Schindler, 2002](#)), the other is based on low-latitude magnetic flux reduction from convection around the Earth toward the dayside ([Hsieh and Otto, 2014, 2015](#)). Both mechanisms are expected from solar wind interaction. For more details, see the review by [Sitnov et al. \(2019\)](#).
4. Recently, regional MHD simulations have also demonstrated that the magnetotail may become unstable even under ideal 2D MHD constraints, when it includes a region of inverse (i.e. tailward) gradient of the normal magnetic field B_z (denoted ‘ B_z hump’ instability; ([Merkin and Sitnov, 2016](#); [Birn et al., 2018](#))).

2.3 Global MHD

Global MHD models representing the (outer) magnetosphere of Earth typically extend around $100 - 200 R_E$ in the flank and tail directions, and around $30 R_E$ (beyond the bow shock) towards the Sun, where the solar wind is coming from. When, occasionally, the solar wind becomes sub-Alfvénic, the bow shock disappears and Alfvén wings form. In this case the upstream boundary has to be moved much further to minimize the boundary effects. It is computationally very demanding to obtain an accurate solution in such a large domain while resolving various structures such as the current sheets at the dayside magnetopause and in the tail. There are various approaches to overcome this difficulty, including the block-adaptive grid of the BATSRUS code (Powell et al., 1999; Tóth et al., 2012), the stretched Cartesian grid of OpenGGCM (Raeder et al., 1997) or the stretched spherical grid of LFM (Lyon et al., 2004).

Another interesting aspect of the upstream condition is the handling of the divergence of the magnetic field. Typically, we have observations at a single point near L1, and assume that the solar wind and IMF have no variation in the transverse direction. If B_x varies, and it certainly does, these assumptions lead to a finite $\nabla \cdot \mathbf{B} = \partial B_x / \partial x$ propagating into the domain. There are various approaches to handle this situation. One is to ignore the problem and propagate the finite $\nabla \cdot \mathbf{B}$ with the flow using some variation of the 8-wave scheme (Powell, 1994). Another common approach is to set B_x to a constant value, for example 0. Finally, one can relax the condition that the transverse gradients in the y and z directions are zero, and guess those gradients from the temporal evolution of B_x . Unfortunately this is an underspecified problem, so there is no unique solution. A typical approach is to smooth B_x in time, and apply some minimum variance constraint. While theoretically nice, in practice the minimum variance approach does not work great. The likely reason is that the magnetic field is turbulent, so local changes in B_x are not representative of the large scale tilt of the propagation plain.

The inner boundary conditions are usually applied at a sphere of radius $1.5 R_E$ to $3 R_E$ surrounding the Earth. One can use a semi-empirical electrodynamic solver (Ridley et al., 2004), or a fully empirical model (Weimer, 1996, 2001) to calculate the $\mathbf{E} \times \mathbf{B}$ drift velocity at the inner boundary. Another important use of an electrodynamic solver is that it can also provide the $\mathbf{E} \times \mathbf{B}$ drift to an inner magnetosphere model (Wolf et al., 1982; Toffoletto et al., 2003a; Buzulukova et al., 2010; Liemohn et al., 2001; Jordanova et al., 1994; Zaharia et al., 2006b), which can calculate realistic ring current and associated pressure (and density) in the closed field line region during geomagnetic storms (Liemohn et al., 2018). The global MHD model can then relax its pressure (and density) towards the values supplied by the inner magnetosphere model. In return, the global MHD model can supply the plasma boundary conditions for the inner magnetosphere model at the edge of the closed field region as well as the magnetic field configuration (De Zeeuw et al., 2004; Meng et al., 2013).

Global models can properly represent the overall dynamics of the interaction of the solar wind with the magnetosphere, including the formation of the bow shock and the magnetopause, as well as the main current sheet in the magnetotail. Magnetic reconnection will happen on the dayside magnetopause and in the magnetotail in

agreement with the theory of the Dungey cycle (Dungey, 1961). The magnetic reconnection in the MHD simulation is not represented by the actual kinetic physics but it is approximated by numerical diffusion or artificial resistivity. Despite these caveats, global MHD models generate reconnection sites where the magnetic field changes sign and the reconnection rate is approximately correct (see Appendix A of Wang et al. (2022a)).

When the grid is relatively coarse, the numerical diffusion will easily adjust to reconnect the incoming magnetic flux carried by the solar wind. For a constant solar wind and IMF driving the simulation will settle to a steady state solution. Using fine grids in combination with low dissipation numerical methods can lead to a more dynamic reconnection process in the model. On the dayside, simulations can produce Flux Transfer Events (Raeder, 2006) and in the tail flux ropes can be produced even by ideal MHD simulations. If the flux ropes in the tail are triggered by sign changes of the IMF B_z , the MHD simulations can match observations very well. A more challenging problem is reproducing substorms and sawtooth events. MHD models cannot do this well (Haiducek et al., 2020), and one needs to add either ionospheric outflow to regulate the reconnection rate (Brambles et al., 2013; Zhang et al., 2020), or kinetic reconnection physics (Wang et al., 2022c) to produce the typical spatial and temporal scales of sawtooth oscillations.

2.4 Test Particles in MHD Simulations

Test particle approaches consist of tracing charged particle orbits in electromagnetic fields that are either prescribed in some plausible fashion or obtained from a simulation that typically does not contain individual particle information, most commonly based on MHD. The approach bridges the gap between large-scale MHD and small-scale particle simulations. In contrast to the latter, it can treat together realistic 3D space and large evolution time scales and realistic electron mass. However, it is not self-consistent and relies on whether the MHD model or the postulated \mathbf{E} , \mathbf{B} fields capture the main physics. But that may also be considered an advantage as it permits studying the effects of large-scale fields in isolation.

In the magnetospheric context ions are usually treated by integration of the full orbit

$$\frac{D\mathbf{u}}{Dt} = \frac{e}{m} \left(\mathbf{E} + \frac{1}{\gamma c} \mathbf{u} \times \mathbf{B} \right). \quad (5)$$

Here γ is the relativistic factor, which may be more relevant for electrons, $\mathbf{u} = \gamma\mathbf{w}$, where \mathbf{w} is the particle velocity, c is the speed of light and $D/Dt = \partial/\partial t + \mathbf{w} \cdot \nabla$ denotes the derivative along the full orbit. Full integration of Equation 5 over extended orbits is not practical for electrons, as it is more time consuming and might accumulate too large errors. Also, the adiabatic drift approximation, based on conservation of the magnetic moment μ , is valid over larger areas in the magnetosphere and can be adequate for identifying typical acceleration mechanisms (e.g., Delcourt and Sauvaud (1994); Li et al. (1998); Zaharia et al. (2000); Gabrielse et al. (2012)).

However, when the full history of electron orbits is considered; this may involve encounters of the reconnection site and low magnetic field, or high curvature regions,

where the conservation of μ breaks down, and full orbit integration is required. Consequently, several codes have been developed that involve a transition between full orbits, integrated by eqn. 5, and drift orbits (e.g., [Birn et al. \(2004\)](#); [Schriver et al. \(2005\)](#); [Ashour-Abdalla et al. \(2011\)](#); [Sorathia et al. \(2017\)](#)). The drift is described by the guiding center drift velocity (e.g., [Birn et al. \(2004\)](#))

$$\mathbf{v}_d = \mathbf{v}_E - \frac{\mu c}{\gamma e} \frac{\mathbf{B} \times \nabla B}{B^2} - \frac{\gamma m_e c v_{\parallel}}{e} \frac{\mathbf{B}}{B^2} \times \frac{d\mathbf{b}}{dt} - \frac{m_e c}{e} \frac{\mathbf{B}}{B^2} \times \frac{d(\gamma \mathbf{v}_E)}{dt} \quad (6)$$

where μ is the (relativistic) magnetic moment, $\mathbf{v}_E = \mathbf{E} \times \mathbf{B}/B^2$ and $\mathbf{b} = \mathbf{B}/B$. In addition, the field-aligned velocity is advanced by

$$\frac{du_{\parallel}}{dt} = -\frac{e}{m_e} E_{\parallel} - \frac{\mu}{\gamma m_e} \frac{\partial B}{\partial s} - (\mathbf{u}_E + \mathbf{u}_{\nabla B}) \cdot \frac{d\mathbf{b}}{\partial t} \quad (7)$$

where now $\mathbf{u} = \gamma \mathbf{v}$ and $\mathbf{v} = \mathbf{v}_E + \mathbf{v}_d + \mathbf{v}_{\parallel}$ describes the guiding center velocity, $\mathbf{v}_{\nabla B}$ is the grad B drift, given by the second term on the right side of eqn. 6, and d/dt is the derivative along the guiding center path. The transition between full orbit and drift orbit is typically determined from an adiabaticity criterion that is based on the ratio between the local field line curvature radius and the gyro radius based on the local magnetic field strength (e.g., [Buchner and Zelenyi \(1989\)](#)). On the switch from drift to full orbit a phase has to be generated, which is typically chosen randomly. Although this can alter individual orbits and make them not reversible, it was found to have no significant effect on general conclusions about sources and properties of distributions (e.g., [Birn et al. \(2004\)](#)).

Two different techniques are used, tracing particle motion either forward or backward in time. Forward tracing requires larger numbers of particles, sometimes comparable to those in PIC simulations, to obtain sufficient numbers at the points of interest (e.g., [Scholer and Jamitzky \(1987\)](#); [Sachsenweger et al. \(1989\)](#); [Perroomian and El-Alaoui \(2008\)](#); [Ukhorskiy et al. \(2017, 2018\)](#)). However, since the particles are not interacting this approach is even more suitable for parallel processing than full particle simulations. In principle, this approach can also include wave scattering and collisions (albeit in an ad-hoc non self-consistent manner) to add to the simple collisionless advance.

Backward tracing is generally based on Liouville's theorem of the conservation of phase space density f to map f from source locations to the final location of interest (e.g., [Curran and Goertz \(1989\)](#); [Birn and Hesse \(1994\)](#); [Birn et al. \(2004\)](#)). It requires fewer orbits to identify properties at selected final locations, but relies on the validity of Liouville's theorem, i.e. the absence of collisions. Backward tracing permits an easier identification of different sources contributing to the final population. Thus, sometimes a combination of both techniques is employed (e.g., [Ashour-Abdalla et al. \(2011\)](#)).

Further complications are related to the use of MHD simulation results. Since the fields are given only on a finite grid, they have to be interpolated in space and time.

1. The advance of the drift equations 6 and 7 requires a third order spatial interpolation in \mathbf{B} for continuous transition between grid cells, which could lead to spurious maxima or minima. This can be avoided, however, by employing a monotonicity algorithm (Hyman, 1983; Birn et al., 2004).
2. Simple interpolation of the electric field could also yield spurious parallel components. This can be avoided, however, by various techniques, for instance, by interpolating E_{\parallel} and E_{\perp} separately (e.g., Birn et al. (2022)).

3 Hall MHD

3.1 Introduction

The ideal-MHD model, as discussed in Sec. 2.1, is well-suited for magnetized plasmas when the dynamics is slow compared to the gyration time of charged particles around the magnetic fields and the length scales over which quantities vary is much larger than the gyroradius of the charged particles. However, going back many years in the study of neutral fluids, fluid models can lead to incorrect and paradoxical results at boundaries layers [*e.g.*, d’Alembert’s paradox (Sec. 4.7 of Choudhuri (1998))]. In a magnetized plasma, these problems can occur where plasmas of two different origins abut against each other (such as at Earth’s magnetopause), at shocks and discontinuities such as Earth’s bow shock, and at localized regions where the magnetic field goes to zero, such as in the solar corona near sunspots.

Magnetic reconnection, in particular, occurs at a boundary layer at a region where at least two components of the magnetic field go to zero, so it is a key example of a physical process that cannot be faithfully modeled by ideal-MHD. Often in numerical simulations, ideal-MHD is used anyway, with numerical dissipation allowing reconnection to occur with the hope that it mimics the actual process. Another approach employs resistivity to model the effect of collisions; this is a useful approach in systems for which collisions are dynamically relevant, but many settings where reconnection occurs – especially in space and the solar corona – are weakly collisional or effectively collisionless (Priest and Forbes, 2000; Cassak and Shay, 2012). There are examples where either approach can be good enough for the questions being asked. For other questions that rely on a faithful representation of the physics in the regions where ideal- and resistive-MHD break down, a new model is necessary. In this section, we discuss a number of approaches within the fluid description that are used to go beyond ideal- and resistive-MHD simulations. In later sections, simulation techniques using the kinetic theory of gases are discussed. There are previous review papers discussing Hall-MHD and numerical approaches (Vasyliunas, 1975; Huba, 1995, 2003; Gomez, 2006).

3.2 The Hall-MHD Model

The equations of Hall-MHD are similar to those of MHD with one key difference. In resistive-MHD, Ohm’s law is given (in cgs units) by

$$\mathbf{E} + \frac{\mathbf{u} \times \mathbf{B}}{c} = \eta \mathbf{J}, \quad (8)$$

where \mathbf{E} and \mathbf{B} are the electric and magnetic fields, \mathbf{u} is the single fluid bulk flow velocity, η is the resistivity, and $\mathbf{J} = (c/4\pi)\nabla \times \mathbf{B}$ is the current density; in ideal-MHD, η is set to zero. To go beyond this model, we revisit where Ohm's law comes from.

The equation of motion of an electron fluid (*i.e.*, Newton's 2nd law) in a fully ionized plasma (in cgs units) is (Braginskii, 1965)

$$m_e \frac{d\mathbf{u}_e}{dt} = -e \left(\mathbf{E} + \frac{\mathbf{u}_e \times \mathbf{B}}{c} \right) - \frac{1}{n_e} \nabla \cdot \mathbf{p}_e + \mathbf{R}_e, \quad (9)$$

where m_e is the electron mass, \mathbf{u}_e is the electron bulk flow velocity, $-e$ is the electron charge, n_e is the electron density, \mathbf{p}_e is the electron pressure which we write more generally as a tensor for now, and \mathbf{R}_e represents the rate of change of momentum resulting from collisions between electrons and other electrons or other charged or neutral particles in the plasma. There are rigorous ways to determine the role of collisions (*e.g.*, Braginskii (1965)) that we do not employ here. Instead, we use the often used simpler approach that assumes $\mathbf{R}_e = m_e \nu_{ei} (\mathbf{u}_i - \mathbf{u}_e)$, where ν_{ei} is the electron-ion collision frequency, and \mathbf{u}_i is the ion bulk flow velocity, and for simplicity we assume the plasma has only electrons and ions (it is fully ionized).

To recover the resistive-MHD Ohm's law from this equation, first the "electron inertia term" $m_e d\mathbf{u}_e/dt$ and the "electron pressure gradient term" $-(\nabla \cdot \mathbf{p}_e)/n_e$ are ignored for reasons we return to in Sec. 3.7. Second, the single fluid bulk flow velocity used in MHD is $\mathbf{u} = (m_i n_i \mathbf{u}_i + m_e n_e \mathbf{u}_e)/(m_i n_i + m_e n_e)$ and the current density $\mathbf{J} = n_i q_i \mathbf{u}_i - n_e e \mathbf{u}_e \simeq n_e e (\mathbf{u}_i - \mathbf{u}_e)$, where the latter form uses the assumption of quasi-neutrality $n_i q_i - n_e e \simeq 0$. Using these expressions to write \mathbf{u}_e in terms of \mathbf{u} and \mathbf{J} gives $\mathbf{u}_e = \mathbf{u} - (\mathbf{J}/ne)[m_i n_i/(m_i n_i + m_e n_e)] \simeq \mathbf{u} - (\mathbf{J}/ne)$, where in the latter form, we use the approximation that $m_i \gg m_e$, since it is at least 1836 in an electron-ion plasma. Using these approximations in Eq. (9) and dividing by e gives

$$\mathbf{E} + \frac{\mathbf{u} \times \mathbf{B}}{c} = \frac{\mathbf{J} \times \mathbf{B}}{n_e e c} + \eta \mathbf{J}, \quad (10)$$

where the resistivity η is defined as $m_e \nu_{ei}/n_e e^2$. If one additionally ignores the $\mathbf{J} \times \mathbf{B}/n_e e c$ term, what remains is the resistive-MHD Ohm's law in Eq. (8). If instead, one ignores the resistive term $\eta \mathbf{J}$, the result is

$$\mathbf{E} + \frac{\mathbf{u} \times \mathbf{B}}{c} = \frac{\mathbf{J} \times \mathbf{B}}{n_e e c}. \quad (11)$$

The term on the right is called the "Hall electric field" \mathbf{E}_H (or simply the "Hall term"), and Eq. (11) is called the "Hall-MHD Ohm's law". Simply coupling this equation to the rest of the ideal-MHD equations gives the Hall-MHD model:

$$\frac{\partial \rho}{\partial t} + \nabla \cdot (\rho \mathbf{u}) = 0, \quad (12)$$

$$\rho \left[\frac{\partial \mathbf{u}}{\partial t} + (\mathbf{u} \cdot \nabla) \mathbf{u} \right] = -\nabla p + \frac{\mathbf{J} \times \mathbf{B}}{c}, \quad (13)$$

$$\frac{\partial p}{\partial t} + (\mathbf{u} \cdot \nabla)p = -\gamma p(\nabla \cdot \mathbf{u}) \quad (14)$$

$$\frac{\partial \mathbf{B}}{\partial t} = -c \nabla \times \mathbf{E}, \quad (15)$$

$$\mathbf{E} + \frac{\mathbf{u} \times \mathbf{B}}{c} = \frac{\mathbf{J} \times \mathbf{B}}{n_e e c} \quad (16)$$

$$\nabla \times \mathbf{B} = \frac{4\pi \mathbf{J}}{c} \quad (17)$$

with the auxiliary equation $\nabla \cdot \mathbf{B} = 0$, and where γ is the single fluid ratio of specific heats, typically taken to be $5/3$. Note n_e in Eq. (16) is related to the MHD mass density via $\rho = m_i n_i + m_e n_e$, so $n_e = \rho / (m_i e / q_i + m_e) \simeq Z \rho / m_i$, where we again assume $m_i \gg m_e$, we use quasi-neutrality to write $q_i n_i \simeq e n_e$, and define $Z = q_i / e$ as the degree of ionization. With these assumptions, Eqs. (12) - (17) form a closed set of equations, and therefore can be used to model physical systems. Technically, these equations actually give the “ideal Hall-MHD model” since resistivity is not retained here.

It is important to note a confusing aspect of these equations. The Hall term is proportional to $\mathbf{J} \times \mathbf{B}$, and Eq. (13) also contains a term including $\mathbf{J} \times \mathbf{B}$. It is tempting to draw relations between the two terms because of this outward similarity, but this should not be done. The two terms have different dimensions: $\mathbf{J} \times \mathbf{B} / c$ is a force density and $\mathbf{J} \times \mathbf{B} / n_e e c$ is an electric field. They have completely different manifestations and impacts on the physics, and therefore actually are not related despite their similar forms.

3.3 Hall-MHD Physics

The only difference between the ideal-MHD and Hall-MHD models is the Hall electric field, and here we investigate the physics introduced by this term. Let \tilde{L} be a characteristic length scale over which the plasma properties vary, and let \tilde{r}_{Li} be the characteristic (Larmor) radius of the ions as they gyrate around a magnetic field of characteristic strength \tilde{B} . The Hall electric field is small and can be neglected if $\tilde{L} \gg \tilde{r}_{Li}$, and doing so brings us back to ideal-MHD. It is important to retain the Hall electric field, and therefore use Hall-MHD, when $\tilde{L} \lesssim \tilde{r}_{Li}$.

To see why structure below the ion gyroscale gives rise to the Hall effect, consider a magnetic field \mathbf{B} that reverses direction over a scale \tilde{r}_{Li} or less, but on larger scales than the characteristic electron gyroradius \tilde{r}_{Le} . For specificity, consider a magnetic field pointing in the $\pm \hat{x}$ direction, as sketched as the black arrows in Fig. 1. The neutral line, where the magnetic field strength vanishes, is the dashed black line. Suppose also there is a uniform electric field \mathbf{E} pointing everywhere in the \hat{z} direction, as sketched as the green arrows. (We use a reversed magnetic field and uniform electric field for illustrative purposes due to its relation to the reconnection process, but the Hall effect is important for any magnetic field configuration that varies on \tilde{r}_{Li} scales.)

At distances from the magnetic field reversal that greatly exceed \tilde{r}_{Li} , ions and electrons undergo the $E \times B$ drift that gives rise to a bulk flow towards the neutral line; the bulk flow velocity of ions and electrons, \mathbf{u}_i and \mathbf{u}_e , respectively, are identical.

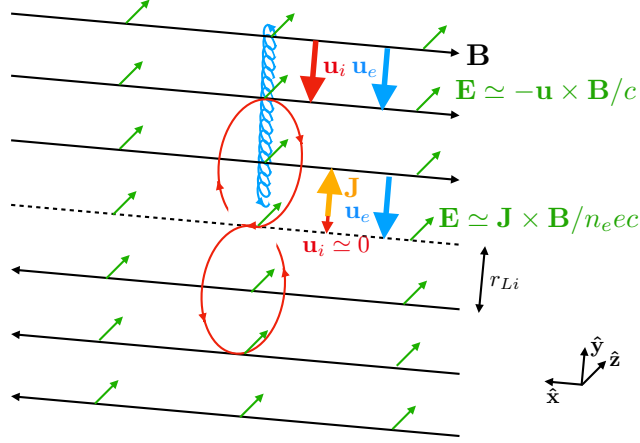


Fig. 1 Physics of the Hall effect in reversing magnetic fields. A reversing anti-parallel magnetic field in the $\pm\hat{x}$ direction is drawn using black arrows, with the neutral line as the dashed line. A uniform electric field in the \hat{z} direction is drawn in green. The smaller blue trajectory is that of an electron $E \times B$ drifting towards the neutral line with bulk velocity \mathbf{u}_e . An ion $E \times B$ drifting far from the neutral line has bulk ion velocity \mathbf{u}_i identical to \mathbf{u}_e , so the electric field in this region is given by $\mathbf{E} = -\mathbf{u} \times \mathbf{B}/c$, where \mathbf{u} is the single fluid (MHD) bulk flow velocity. Within an ion gyroradius r_{Li} of the neutral line, the electron continues with bulk flow \mathbf{u}_e , while the ion demagnetizes (in the red trajectory) and \mathbf{u}_i becomes small. In this region, there is a non-zero current density \mathbf{J} (orange), and the electric field in this region is predominantly given by the Hall electric field $\mathbf{E} = \mathbf{J} \times \mathbf{B}/n_e ec$.

The $E \times B$ drift of the electrons above the neutral line is sketched as the blue curve. In the region farther from the neutral line than \tilde{r}_{Li} , the electric field is given by $\mathbf{E} = -\mathbf{u} \times \mathbf{B}/c$, where $\mathbf{u} = \mathbf{u}_i = \mathbf{u}_e$ is the MHD bulk flow velocity.

As the ions reach a distance from the neutral line that is equal to its gyroradius, the ions cross the neutral line and are immersed in a magnetic field pointing in the opposite direction. Their gyromotion changes direction, and they make figure 8 orbits, sketched as the red curve. (They also accelerate in the \hat{z} direction due to the electric field, but this is omitted from the sketch.) Consequently, their bulk velocity becomes small, $\mathbf{u}_i \simeq 0$.

Since we assumed $\tilde{L} > \tilde{r}_{Le}$, the electrons have a smaller gyroradius and do not see the magnetic field reversal, so they continue to undergo the $E \times B$ drift towards the neutral line. The key is that the ions and electrons are undergoing different dynamics between distances from the neutral line of \tilde{r}_{Li} and \tilde{r}_{Le} !

In this region, the difference in the bulk motion between ions and electrons implies there is a net current density \mathbf{J} , sketched as the orange arrow, and called the Hall current. The current density is perpendicular to the magnetic field \mathbf{B} . Then, between \tilde{r}_{Li} and \tilde{r}_{Le} from the neutral line, the electric field is given by the Hall electric field $\mathbf{E}_H = \mathbf{J} \times \mathbf{B}/n_e ec$. This exemplifies why the Hall electric field is important between ion and electron gyroscals.

This situation in a plasma is analogous to the Hall effect in condensed matter physics, where it was originally discovered by Edwin Hall (a graduate student) in 1879 (Hall et al., 1879). It has extensive applications in that field of study. The

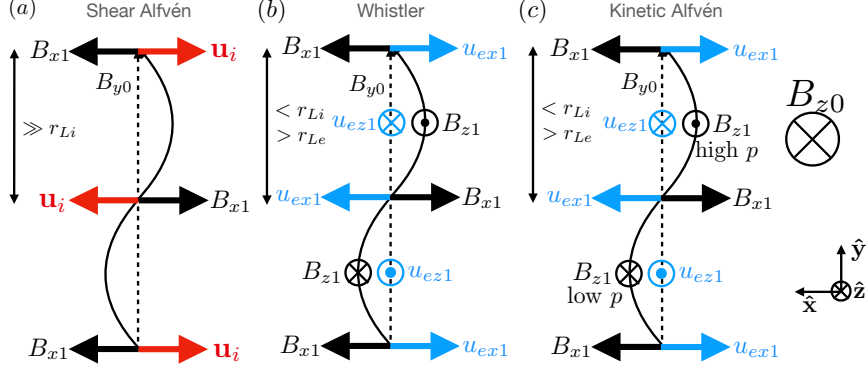


Fig. 2 Sketch of how the Hall effect impacts linear waves in MHD. The wave structure for (a) shear Alfvén waves, (b) parallel propagating whistler waves, and (c) kinetic Alfvén waves. The equilibrium magnetic field B_{y0} is the dashed black arrow. The perturbed magnetic field \mathbf{B}_1 are the black arrows. The perturbed ion bulk flow \mathbf{u}_i are the red arrows, which occur in (a) because the wavelength is much larger than the ion gyroradius. In (b) and (c), the wavelength is at or below ion gyroscaler, so the bulk flow is due to electron motion in the blue arrows. In (c), there is a large out-of-plane equilibrium magnetic field B_{z0} , so the magnetic perturbation B_{z1} changes the magnetic pressure which to first order and requires a change to the gas pressure p .

derivation generalizing shear Alfvén waves to include the Hall effect happened as early as 1954 by Jim Dungey (Dungey, 1954), the same person who first understood magnetic reconnection and gave the process its name.

3.4 Linear Waves in ideal Hall-MHD

It would take us too far afield to elucidate how the Hall electric field modifies all the physics of ideal-MHD. Rather, we highlight one important example – linear waves. In ideal-MHD, there are three propagating linear waves available to a uniform plasma: the shear Alfvén wave and the fast and slow magnetosonic waves. The Hall electric field introduces two wave modes that become important between ion and electron gyroscaler – the whistler wave and the kinetic Alfvén wave.

3.4.1 The Whistler Wave

First, we consider transverse waves propagating along a uniform background magnetic field of strength B_0 , which without loss of generality we take to be in the y direction, in a plasma of equilibrium mass density $\rho_0 \simeq m_i n_i$ and with no equilibrium bulk flow or current $\mathbf{u}_0 = 0$ and $\mathbf{J}_0 = 0$. The wave vector \mathbf{k} is also in the y direction. Linearizing the Hall-MHD equations (12)-(59) about the given equilibrium with \mathbf{k} parallel to \mathbf{B}_0 and solving for the dispersion relation gives

$$\omega^2 = k^2 c_{A0}^2 \left(1 + \frac{k^2 d_{i0}^2}{2} + \sqrt{k^2 d_{i0}^2 + \frac{k^4 d_{i0}^4}{4}} \right), \quad (18)$$

where ω is the wave frequency, $c_{A0} = B_0/(4\pi\rho_0)^{1/2}$ is the Alfvén speed, and $d_{i0} = (m_i c^2/4\pi n_0 q_i^2)^{1/2}$ is the ion inertial length.

In the limit of $kd_{i0} \rightarrow 0$, this dispersion relation reduces to $\omega^2 \rightarrow k^2 c_{A0}^2$, which is simply the shear Alfvén wave from ideal-MHD. In the other extreme, consider the limit $kd_{i0} \rightarrow \infty$. The 1 in Eq. (18) becomes negligible compared to $k^2 d_{i0}^2/2$ outside the square root, and the $k^2 d_{i0}^2$ is negligible compared to $k^4 d_{i0}^4/4$ inside the square root, so to low order the dispersion relation becomes

$$\omega^2 \rightarrow k^4 c_{A0}^2 d_{i0}^2 \quad (\text{as } kd_{i0} \rightarrow \infty). \quad (19)$$

This is the dispersion relation for the so-called “whistler wave.”

Physically, the whistler wave is the sub-ion gyroscale counterpart of the shear Alfvén wave. The plasma properties in a shear Alfvén wave are sketched in Fig. 2(a). The equilibrium magnetic field B_{y0} is the dashed black arrow. A magnetic perturbation transverse to the equilibrium B_{x1} is the large black arrow. Since the size of the wave is far larger than the ion gyroradius, the frozen-in ions and electrons feel a restoring force analogous to plucking a guitar string, generating bulk flows in the x direction (shown for ions as the red arrows). The shear Alfvén wave is a linearly polarized wave.

The whistler wave, sketched in panel (b), occurs when the magnetic field varies between ion and electron gyroscscales. Then, the ions are not frozen-in and do not respond to the plucked magnetic field line, but the electrons are frozen in and feel a restoring force. The x component of the perturbed electron flow u_{ex1} is sketched as the blue arrows. Since the electrons have a bulk velocity but the ions do not, this means there is a net current density, which induces an oscillating magnetic field out of the plane, labeled as B_{z1} . Similarly, the varying B_{x1} requires a u_{ez1} to sustain the current. This turns the wave into a circularly polarized wave. The polarization is right handed, *i.e.*, a receiver sees the magnetic field rotate in a counterclockwise direction.

There is a crucial difference between the shear Alfvén wave and the whistler wave. The shear Alfvén wave has a phase speed $\omega/k = c_{A0}$, which is a constant independent of ω and k , so a shear Alfvén wave travels at the same speed regardless of its wavelength. It is an example of a non-dispersive wave that retains its waveform as it propagates (like a light wave in vacuum or a sound wave in a neutral fluid). In contrast, the phase speed for the whistler wave, from Eq. (19), is $\omega/k = kc_{A0}d_{i0}$. Thus, the phase speed is faster for shorter wavelength waves. This is an example of a dispersive wave, since a wave packet does not retain its shape. The dispersive nature is what gives the wave its name; it makes a characteristic “whistle” from high frequencies descending to low frequencies when it is detected at a location away from where it was generated. For example, when a lightning strike in one hemisphere excites a whistler wave on Earth’s magnetic field, the high frequencies arrive before the low frequencies in the other hemisphere.

This analysis reveals the critical scale at which the Hall effect becomes important for transverse bending of the magnetic field. The three terms in Eq. (19) proportional to d_{i0} are absent if the Hall term is left out of the governing equations (*i.e.*, in ideal-MHD). By comparing the first term (1) to the other terms, we see they become

important when kd_{i0} is on the order of 1. This means that the Hall term becomes important at length scales below d_{i0} .

The ion inertial scale is related to a form of the ion gyroradius. To see this, note that an ion moving at the Alfvén speed c_{A0} that gyrates around a magnetic field of strength B_0 has a gyroradius r_{Li} given by

$$r_{Li} = \frac{c_{A0}}{\Omega_{ci0}} = d_{i0}, \quad (20)$$

where $\Omega_{ci0} = q_i B_0 / m_i c$ is the ion gyrofrequency. Thus, the scale at which the Hall effect becomes important for transverse perturbations is when gradient scales are comparable to the ion inertial scale. Using characteristic scales for Earth's dayside magnetosheath, $d_{i0} \simeq 70$ km; for the solar corona, $d_{i0} \simeq 2$ m. Thus, we have a feel for length scales over which we need to use Hall-MHD instead of ideal-MHD in two important space applications.

3.4.2 The Kinetic Alfvén Wave

Now, we consider the kinetic Alfvén wave. These waves are almost completely longitudinal, but not perfectly longitudinal. To allow for a strong analogy to the whistler wave, consider a uniform magnetic field that has a very large z component $B_{z0} \gg 0$ and very small y component B_{y0} , as sketched in Fig. 2(c). As in panels (a) and (b), the wave propagates in the y direction. If B_{z0} were zero, it would be the whistler wave. Physically, if the wavelength is between ion and electron gyroscscales, this perturbation reacts similar to a whistler in that it sets up an electron flow that bends the magnetic field out of the plane. The perturbed magnetic field therefore has a component in the same or opposite direction as B_{z0} . Where B_{z0} and the perturbed magnetic field are parallel, the magnetic pressure $(B_{z0} + B_{z1})^2 / 8\pi$ is greater than the initial pressure $B_{z0}^2 / 8\pi$ to first order in the perturbed field. (Note, for the whistler wave, the pressure difference $B_{z1}^2 / 8\pi$ is second order in the perturbed magnetic field, so it is negligible.) Similarly, where B_{z1} opposes B_{z0} , the magnetic pressure decreases to first order. Now, if the plasma is overall low β (since we took B_{z0} to be large), this magnetic pressure imbalance cannot be maintained, so the gas pressure has to change in order to balance pressure. Electrons move along the magnetic field and ions move across the magnetic field to move from the high magnetic pressure region to the low magnetic pressure region, setting up a high and low gas pressure region as denoted in panel (c). This describes the physics of the kinetic Alfvén wave.

To find the dispersion relation of the kinetic Alfvén wave, we back up to the full dispersion relation of any wave in Hall-MHD. Linearizing Eqs. (12) - (59) around a uniform magnetic field, density, and pressure with an arbitrary linear perturbation and solving gives the following dispersion relation (Rogers et al., 2001):

$$\omega^6 - (c_{ms}^2 + c_{Ak}^2 + k^2 c_{Ak}^2 d_{i0}^2) k^2 \omega^4 + [c_{ms}^2 + c_s^2 (1 + k^2 d_{i0}^2)] k^4 c_{Ak}^2 \omega^2 - k^6 c_{Ak}^4 c_s^2 = 0, \quad (21)$$

where $c_A^2 = B_0^2/(4\pi\rho_0)$ is the total Alfvén speed, $c_s^2 = \gamma p_0/\rho_0$ is the sound speed, $c_{ms}^2 = c_s^2 + c_A^2$ is the total fast magnetosonic speed, and $c_{Ak}^2 = B_{y0}^2/4\pi\rho_0$ is the Alfvén speed based only on B_{y0} . In the $k^2 d_{i0} \rightarrow 0$ long wavelength limit, this equation reduces to the dispersion relation for ideal-MHD waves. In the limit of large kd_{i0} , one solution is a high frequency solution which is approximately given by balancing the first two terms in Eq. (21), which gives $\omega^2 \simeq k^4 c_{Ak}^4 d_{i0}^2$, the whistler wave dispersion relation in Eq. (19). There is also a medium frequency solution which arises from balancing the middle two terms in Eq. (21). This ratio in general is

$$\omega^2 \simeq \frac{c_{ms}^2 + c_s^2(1 + k^2 d_{i0}^2)}{c_{ms}^2 + c_{Ak}^2 + k^2 c_{Ak}^2 d_{i0}^2} k^2 c_{Ak}^2. \quad (22)$$

In the limit in which $c_{ms}^2 \ll c_s^2 k^2 d_{i0}^2$ and $c_{ms}^2 \gg c_{Ak}^2 + k^2 c_{Ak}^2 d_{i0}^2$, the resulting dispersion relation is $\omega^2 \simeq (c_s^2/c_{ms}^2) k^4 d_{i0}^2 c_{Ak}^2$, which in the $c_A^2 \gg c_s^2$ (low β) limit gives $\omega^2 \simeq (c_s^2/c_A^2) k^4 d_{i0}^2 c_{Ak}^2$. Since $k^2 c_{Ak}^2 = k_{\parallel}^2 c_A^2$, this becomes

$$\omega^2 \simeq k_{\parallel}^2 k^2 c_A^2 \rho_s^2, \quad (23)$$

where $\rho_s^2 = c_s^2/\Omega_{ci}^2$ is the ion Larmor radius based on the sound speed. This is the dispersion relation for the kinetic Alfvén wave. As with the whistler wave, the kinetic Alfvén wave is dispersive with $\omega/k \propto k_{\parallel}$, so it gets faster for smaller wavelengths. The length scale at which the Hall term becomes important for the kinetic Alfvén wave is ρ_s (as opposed to d_{i0} for the whistler wave).

3.5 A Numerical Algorithm for Hall-MHD

Including the Hall electric field has a significant impact on numerical simulations relative to MHD simulations. One way to think of why this is the case is that the waves in ideal-MHD are non-dispersive, so waves at any scale from the large scale down to the computational grid scale travel at the same speed. In Hall-MHD, as discussed in the previous section, both whistler and kinetic Alfvén waves are dispersive, so waves at the grid scale (which needs to be sub-ion gyroscale to capture the Hall electric field) are considerably faster than waves at the large scale. This makes the Hall-MHD equations “stiff” – one must use a much smaller time step in Hall-MHD than in ideal-MHD, leading to a significant increase in the run time and expense of the simulation.

There are numerous algorithms that can be used to numerically evolve the equations in time. We provide one in detail, and mention references to other algorithms that have been used. We highlight the F3D code (Shay et al., 2004), which has been used for many years to study magnetic reconnection. First, the evolution equations are written in conservative form as

$$\frac{\partial n}{\partial t} + \nabla \cdot \mathbf{J}_i = 0, \quad (24)$$

$$\frac{\partial \mathbf{J}_i}{\partial t} + \nabla \cdot \left(\frac{\mathbf{J}_i \mathbf{J}_i}{n} + \frac{p \mathbf{I}}{m_i} + \frac{\mathbf{B} \mathbf{B}}{4\pi m_i} - \frac{B^2 \mathbf{I}}{8\pi m_i} \right) = 0, \quad (25)$$

$$\frac{\partial p}{\partial t} + \nabla \cdot (\mathbf{u}p) + (\gamma - 1)p(\nabla \cdot \mathbf{u}) = 0, \quad (26)$$

$$\frac{\partial \mathbf{B}}{\partial t} + c\nabla \times \mathbf{E} = 0, \quad (27)$$

with auxiliary equations $\mathbf{E} = \mathbf{J} \times \mathbf{B}/nec - \mathbf{J}_i \times \mathbf{B}/nc$ and $\mathbf{J} = (c/4\pi)\nabla \times \mathbf{B}$. Here, $n \simeq \rho/m_i$ is the number density of ions (approximately equal to the number density of electrons due to quasi-neutrality) and $\mathbf{J}_i = n\mathbf{u}$ is the ion flux density.

In F3D, these equations are stepped forward using the trapezoidal leapfrog technique, a predictor-corrector method that is well-equipped to handle conservative equations (Zalesak, 1979, 1981). Each of the above equations can be written as a conservative equation of the form

$$\frac{\partial \psi}{\partial t} + \nabla \cdot \mathcal{F} - D\nabla^2\psi + F(\xi) = 0, \quad (28)$$

where ψ is the plasma variable in question, \mathcal{F} is a suitably defined flux, D is a second order diffusion coefficient which can be added to the equations to represent resistivity, viscosity, or a numerical dissipation to improve code stability, and $F(\xi)$ is a suitably defined source term in terms of any other plasma variables ξ . (Equation 27 is not exactly in this form, but an analogous expression holds.)

To write the numerical algorithm, we use the standard notation where a superscript n on a plasma variable refers to the time step in question, so the initial values are set at $n = 0$, the first time step is $n = 1$, and so on. To evolve ψ^n to ψ^{n+1} in a time step Δt , the trapezoidal leapfrog algorithm is

$$\begin{aligned} \psi^{n+1/2} = & \frac{\psi^{n-1} + \psi^n}{2} + \Delta t [-\nabla \cdot \mathcal{F}^n \\ & + D\nabla^2\psi^{n-1} - F(\xi^n)] \end{aligned} \quad (29)$$

$$\begin{aligned} \psi^{n+1} = & \psi^n \Delta t [-\nabla \cdot \mathcal{F}^{n+1/2} \\ & + D\nabla^2\psi^n - F(\xi^{n+1/2})]. \end{aligned} \quad (30)$$

The first equation uses the data at the n 'th time step and the data at the previous $n - 1$ 'st time step to “predict” ψ half a time step in the future. Then, the flux and source terms are evaluated at this intermediate time step to evolve ψ the next half time step to the desired step $n + 1$. To go from $n = 0$ to $n = 1$, data is needed at $n = -1$, which is simply taken to be the same as the data at $n = 0$. This algorithm is second order in the time step Δt , meaning that the error from the algorithm is approximately a coefficient times the square of the time step. This is an example of an “explicit” time stepping algorithm because the data at the future time step is found completely using known data at the current or previous time steps.

The above shows how the equation is stepped forward temporally, but one also needs to calculate spatial derivatives. The approach F3D uses to calculate spatial derivatives is with a finite difference technique, which means the spatial derivatives are simply approximated by the derivative over the size of a grid scale instead of over

an infinitesimal distance. For example, one approximation for the partial derivative in the x direction on a grid with grid scale Δx is $\partial\psi_j/\partial x \simeq (\psi_{j+1} - \psi_{j-1})/2\Delta x$, where the j subscript refers to the index of the spatial cell for which the derivative is desired. This is a second-order scheme because the error relative to the exact derivative scales like Δx^2 . The F3D code uses the approximation

$$\frac{\partial\psi_j}{\partial x} \simeq \frac{2}{3\Delta x}(\psi_{j+1} - \psi_{j-1}) - \frac{1}{12\Delta x}(\psi_{j+2} - \psi_{j-2}), \quad (31)$$

which is fourth order (the error scales like Δx^4), and the cost for this higher order derivative is that it requires data from two adjacent cells on each side rather than one. Analogous expressions hold for derivatives in the y and z directions.

The F3D code is written in Fortran 90 and is parallelized using Message Passing Interface (MPI) for use on supercomputers. The computational domain is rectangular with a fixed, regular grid. It can be run in two or three dimensions. When in two dimensions, the vectors can have an out of plane component even though all quantities are invariant in the out-of-plane direction; this is often referred to in the literature as “2.5 dimensional”. The F3D code does not explicitly enforce that $\nabla \cdot \mathbf{B} = 0$, but it has been demonstrated that the value is small when the initial magnetic field is divergence free. Numerous aspects of the F3D code are on user-controlled switches that can turn terms or effects on or off, and the initial plasma variable profiles and values are controlled by the user. Other features of F3D that are used to go beyond the Hall-MHD model will be treated in Sec. 3.7.

To run the F3D code, the user chooses the simulation domain size and desired grid scale to resolve the relevant physics, which is typically at least 5 times smaller than the relevant ion gyroradius. As F3D is an explicit finite difference code, the time step Δt can be no larger than allowed by the so-called Courant-Friedrichs-Lewy (CFL) condition (Press et al., 1992), which requires $\Delta t \leq \Delta x/v_{\text{fastest}}$, where v_{fastest} is the fastest speed that can occur in the system. For Hall-MHD, the fastest speed is typically the whistler or kinetic Alfvén wave speed at or near the grid scale, but can be the fast magnetosonic speed for some ambient plasma conditions. F3D simulations are typically performed with time step about 80% of the CFL condition.

Any employed diffusion coefficients then need to be chosen. Often, the resistivity is not used for Hall-MHD, but a fourth-order diffusion numerical dissipation of the form $+D_4\nabla^2\nabla^2$ on the right hand side of Eq. (28) is included to damp structures at the grid scale while minimally affecting larger scale structures. It is handled numerically using the same finite difference approach as the other terms. The appropriate diffusion coefficient scales with $D_4 \sim v_{\text{fastest}}[\pi/(\Delta x)]^3$. An appropriate value for this coefficient is when it is large enough to control numerical issues at the grid scale while not impacting the large scale physics. A good approach to optimize this value is to run multiple simulations with only varying D_4 , and finding a range of values for which the numerics are good and the large scale features are only weakly dependent on D_4 ; it is typically within an order of magnitude of the scaling prediction.

We have focused on F3D as an example of a Hall-MHD code because of its algorithmic simplicity and because it has long been used to study reconnection. There are drawbacks to the code. As a finite difference code, it does not capture shocks,

and therefore if the number density gets fairly small in any given simulation the code typically crashes. The code performs well up to about 1,000-2,000 processors on high powered supercomputers; MHD codes without the Hall effect can be made to scale much better to 10s of thousands of processors. It is also restricted to a rectangular geometry with a regular grid.

There are a number of other Hall-MHD codes that have been used to study magnetic reconnection, some of which we gather here. Some codes used to study Hall-MHD reconnection in a rectangular domain have included VOODOO (Huba, 2003), HMHD (Lottermoser and Scholar, 1997), another code called HMHD (Huang et al., 2011), and the UI Hall-MHD code (Ma and Bhattacharjee, 2001). Codes that have been used to study Hall-MHD in the context of planetary magnetospheres (including Earth’s) are a multi-fluid code (Winglee, submitted, 2004), BATS-R-US (Tóth et al., 2008), and Gkyell (Wang et al., 2018). Codes used in the tokamak geometry include NIMROD (Glasser et al., 1999) and M3D-C1 (Jardin et al., 2008).

3.6 Boundary Conditions in Hall-MHD

Boundary conditions for Hall-MHD codes can be challenging. The boundary conditions are set using “guard cells” (sometimes called “ghost cells”). For example, if the desired spatial domain for a simulation has 100 cells in a particular direction, the array is padded by some number of cells to execute the boundary conditions. For example, the fourth-order finite difference technique used for spatial derivatives in F3D requires two cells on either side of the grid point in question. Thus, for a cell on the boundary, there needs to be two cells worth of information to evolve those cells. This is accomplished by using two guard cells on each side, so a 100 cell domain requires an array of 104 cells. For a second-order finite difference, only a single guard cell is needed on each side.

The simplest set of boundary conditions is to use periodic boundaries, which is the technique employed for most F3D studies. Suppose we have N physical grid cells. Let the cell index j go over all spatial cells including the guard cells. Then, the two guard cells have indices $j = 1, 2, N + 3$, and $N + 4$, and the physical cells have $j = 3, 4, \dots, N + 2$. For a variable ψ , periodic boundary conditions are implemented using

$$\psi_1^{n+1} = \psi_{N+1}^{n+1}, \quad (32)$$

$$\psi_2^{n+1} = \psi_{N+2}^{n+1}, \quad (33)$$

$$\psi_{N+3}^{n+1} = \psi_1^{n+1}, \quad (34)$$

$$\psi_{N+4}^{n+1} = \psi_2^{n+1}, \quad (35)$$

where the superscript $n + 1$ again refers to the time slice. The advantage of periodic boundary conditions is that there is no additional error introduced to the plasma variables at the boundaries as a result of the boundary conditions. The primary disadvantage is that plasma from one side comes back through the other side which may not be realistic for the intended application.

Another boundary condition is zero derivative, *i.e.*, Neumann, boundary conditions. To implement this, the guard cells are defined as

$$\psi_1^{n+1} = \psi_5^{n+1}, \quad (36)$$

$$\psi_2^{n+1} = \psi_4^{n+1}, \quad (37)$$

$$\psi_{N+3}^{n+1} = \psi_{N+1}^{n+1}, \quad (38)$$

$$\psi_{N+4}^{n+1} = \psi_N^{n+1}. \quad (39)$$

This boundary condition can be successful if the dynamics take place away from the boundaries.

Other choices for boundary conditions can be employed, but we finish our treatment with a discussion of “conducting wall” boundary conditions. These boundary conditions are common for ideal MHD simulations. Consider a boundary with its normal in the y direction, representing the upstream/inflow direction. In MHD, a conducting wall has a vanishing electric field in the plane of the boundary, $E_x = E_z = 0$ (Dirichlet boundary conditions), but the normal electric field E_y can be nonzero (Neumann boundary conditions). The magnetic field can be tangential (B_x and B_z are Neumann), but Faraday’s law implies the normal magnetic field cannot change in time (B_y is Dirichlet) because doing so would generate a tangential electric field. With this magnetic field, there is no curl of B_y , so J_x and J_z must vanish at the boundary (Dirichlet), but there can be a non-zero J_y (Neumann). Finally, the bulk flow velocity can be tangential (v_x and v_z are Neumann) while the normal bulk flow must vanish (v_y is Dirichlet) for Ohm’s law to be satisfied at the boundary. This set of boundary conditions is consistent with the governing equations.

In Hall-MHD, these conducting wall boundary conditions do not work. The reason is that instead of Ohm’s law being $\mathbf{E} + \mathbf{v} \times \mathbf{B}/c = 0$, it is $\mathbf{E} + \mathbf{v} \times \mathbf{B}/c = \mathbf{J} \times \mathbf{B}/n_e ec$. The boundary conditions in the previous paragraph for \mathbf{v} and \mathbf{J} are opposite. Thus, there is no way to have the Hall term be consistent with the requirement that the electric field can only be normal to the boundary.

3.7 Further Extensions of Hall-MHD

Here, we briefly discuss fluid model extensions beyond ideal-MHD that contain the Hall electric field and other terms. We start with terms that were dropped from Eq. (9).

3.7.1 Hall-MHD with Electron Inertia

One extension of Hall-MHD is to retain the electron inertia term $m_e d\mathbf{u}_e/dt$ from Eq. (9). We call this model “Hall-MHD with electron inertia;” it is often called the “two-fluid model” in the literature, but we refrain from this nomenclature since a completely different set of equations is also typically given the same name.

Using the electron inertia term as is would lead to a new variable \mathbf{u}_e with a time derivative in the model. Instead, the standard approach is to recognize that the prefactor m_e is small for electron-ion plasmas, so the only way this term important is if the electrons are moving very fast. The ions would be too slow to keep up in such a case, so on time scales where this term is important, we can treat the ions

as approximately stationary. Then, the electron bulk flow velocity \mathbf{u}_e is related to the current density via $\mathbf{u}_e = -\mathbf{J}/n_e e$. Since \mathbf{J} and n_e are already included in the Hall-MHD description, the set of equations remains closed. Such a simplification is convenient but not absolutely necessary. For example, Sec. 4.4 describes a hybrid code in which the ion flows and density effects in the electron inertia term are included.

Analytically, the inertial electric field from dividing Eq. (9) by $-e$ is given by $-(m_e/e)d\mathbf{u}_e/dt$, and replacing \mathbf{u}_e by $-\mathbf{J}/n_e e$ gives $(m_e/e^2)d(\mathbf{J}/n_e)/dt$. Then, Ohm's law in Hall-MHD with electron inertia becomes

$$\mathbf{E} + \frac{\mathbf{u} \times \mathbf{B}}{c} = \frac{\mathbf{J} \times \mathbf{B}}{n_e e c} + \frac{m_e}{e^2} \frac{d}{dt} \left(\frac{\mathbf{J}}{n_e} \right). \quad (40)$$

It is important to note that the same approximation $\mathbf{u}_e \simeq -\mathbf{J}/n_e e$ is used in the convective derivative term, so that $d/dt \simeq \partial/\partial t - (1/n_e e)\mathbf{J} \cdot \nabla$.

One needs to treat the $\partial/\partial t$ term on the right hand side of Eq. (40). To do so, we eliminate \mathbf{E} in Faraday's law using Eq. (40); some algebra reveals that the equation becomes

$$\frac{\partial \mathbf{B}'}{\partial t} = -c \nabla \times \mathbf{E}', \quad (41)$$

where $\mathbf{B}' = (1 - d_e^2 \nabla^2)\mathbf{B}$ is an auxiliary magnetic field and $\mathbf{E}' = \mathbf{J} \times \mathbf{B}'/n_e e c - \mathbf{J}_i \times \mathbf{B}/n_e e c$ is an auxiliary electric field, and the factor of n in the inertia term is treated as a constant on the time scales of interest. Coupling this equation with Eqs. (24)-(26) gives a closed set of equations.

To solve these equations, we note that Eq. (41) looks just like the usual Faraday's law except for the primes, so the same numerical technique can be used to solve for \mathbf{B}' . Once \mathbf{B}' is found, one uses that variable as the known source term in the equation $(1 - d_e^2 \nabla^2)\mathbf{B} = \mathbf{B}'$ to solve for \mathbf{B} . This is an elliptic differential equation with many algorithms that can be used to solve it. The simplest may be a relaxation technique (Press et al., 1992), but it is relatively slow, especially when used for codes that have been parallelized for use on a supercomputer. A faster version of relaxation is called multigrid (Trottenberg et al., 2000). F3D employs the Fast Fourier Transform approach.

We now briefly discuss the physics introduced by the electron inertia term and the advantages for including it in simulations. By comparing the electron inertia term to the Hall term, we determine the condition under which it is important to retain the electron inertia term. We know the Hall electric field is important at scales below the ion inertial scale d_i , but vanishes at the X-line where $\mathbf{B} = 0$. The electron inertia term can be important at small scales, so we seek the scale at which it becomes comparable to the Hall electric field. Setting them equal gives $J_y B_x / n_e c \sim (m_e/e^2)[(\mathbf{J}/n_e) \cdot \nabla](J_z/n)$. In the scaling sense, we use $B_x \sim B_{up}$, $J_z \sim c B_{up} / 4\pi \delta$ where δ is the scale at which the two terms are equal, so $J_y B_{up} / n_e c \sim (m_e/e^2)(J_y/n e \delta)(c B_{up} / 4\pi \delta n)$, which simplifies to $\delta^2 \sim d_e^2$, where $d_e^2 = m_e c^2 / 4\pi n e^2$ is the electron inertial scale. Thus, at length scales below d_e , the electron inertia term can be important.

Consequently, one reason researchers include the electron inertia term into their Hall-MHD model is to aim to capture electron scale physics more accurately than without it. We point out, however, that the MHD model itself was derived with the

assumption that m_e/m_i is small, and therefore including the electron inertia term as we have done does not actually provide a self-consistent treatment of sub- d_e scale physics. The two fluid model or the kinetic approach is needed to more accurately capture electron scale physics.

Then why include electron inertia? The answer is that it helps with the numerics. To see this, we consider waves in the Hall-MHD with electron inertia system, generalizing the treatment in Secs. 3.4.1 and 3.4.2. The dispersion relation for perfectly parallel propagating waves in Hall-MHD with electron inertia, generalizing Eq. (18), becomes

$$\omega^2 = \frac{k^2 c_{A0}^2}{D_e} \left(1 + \frac{k^2 d_{i0}^2}{2D_e} + \sqrt{\frac{k^2 d_{i0}^2}{D_e} + \frac{k^4 d_{i0}^4}{4D_e^2}} \right), \quad (42)$$

where $D_e = 1 + k^2 d_e^2$. When kd_e is negligible, this dispersion relation reduces to the Hall-MHD result in Eq. (18). When $kd_e \gg 1$, the waves become electron cyclotron waves with $\omega^2 = \Omega_{ce}^2$, where $\Omega_{ce} = eB_0/m_e c$. The reason this is useful numerically is that the whistler wave is dispersive, and in Hall-MHD the phase speed goes to infinity as the wavelength goes to zero. In Hall-MHD with electron inertia, the whistler rolls over to the electron cyclotron wave which does not propagate, so there is a maximum speed of the waves. This means that the time step required to run the simulation does not go to zero, and the simulations with very high resolution are less stiff and therefore cheaper to carry out.

3.7.2 Electron Magnetohydrodynamics (EMHD)

The electron-MHD (EMHD) model (Kingsep et al., 1990) is used when the large (MHD) scales are not of interest, and only the scales between electron and ion scales are of interest. In such a limit, the MHD terms concerning ion velocity are dropped. Because of this, the density and pressure can no longer change (on the time scales of interest), so the only remaining governing equation is Faraday's law, with the electric field given solely by the Hall electric field:

$$\frac{\partial \mathbf{B}}{\partial t} = -c \nabla \times \mathbf{E}, \quad (43)$$

$$\mathbf{E} = \frac{\mathbf{J} \times \mathbf{B}}{nec}. \quad (44)$$

Using Ampère's law $\mathbf{J} = (c/4\pi)\nabla \times \mathbf{B}$, it is common to combine these equations into a single equation for \mathbf{B} ,

$$\frac{\partial \mathbf{B}}{\partial t} = -\frac{c}{4\pi ne} \nabla \times [(\nabla \times \mathbf{B}) \times \mathbf{B}]. \quad (45)$$

This closed vector equation comprises the EMHD model. One can include electron inertia in a manner analogous to the full Hall-MHD model: $\partial \mathbf{B}' / \partial t = -(1/n_e e) \nabla \times (\mathbf{J} \times \mathbf{B}')$, where $\mathbf{J} = (c/4\pi)\nabla \times \mathbf{B}$ and $\mathbf{B}' = (1 - d_e^2 \nabla^2) \mathbf{B}$.

3.7.3 The Electron Pressure Term in Hall-MHD

We now consider the electron pressure term in Eq. (9). There, electron pressure is written as a tensor \mathbf{p}_e , which is the most general form following directly from the Vlasov/Boltzmann equation in kinetic theory. Retaining it in Ohm's law would give a term on the right hand side of Eq. (40) of the form $-(1/n_e e)\nabla \cdot \mathbf{p}_e$. We now consider a few commonly used approximations to simplify this.

Isotropic Electron Pressure -

In MHD, the total pressure is assumed to be isotropic, so that $\mathbf{p} = p\mathbf{I}$. In this case, the term entering Ohm's law is $-(1/n_e e)\nabla p_e$. When substituted into Faraday's law [Eq. (15)], this term gives a contribution of $(c/e)\nabla \times (\nabla p_e/n) = (c/e)\nabla(1/n_e) \times \nabla p_e = -(c/en_e^2)\nabla n_e \times \nabla p_e$. This contribution to the electric field is called the ‘‘Biermann battery’’ (Biermann, 1950) and it is often of great importance in reconnection in high energy density plasmas (Fox et al., 2012). In most space applications that employ a fluid model, the electrons are assumed to be adiabatic with p_e/n_e^γ equal to a constant or isothermal with p_e/n_e equal to a constant. In either limit, the Biermann battery term vanishes identically.

One may presume from this result that the electron pressure gradient term does not have any contribution to Hall-MHD, but this is not true. Including the scalar electron pressure gradient in the Hall-MHD Ohm's law gives

$$\mathbf{E} + \frac{\mathbf{u}_e \times \mathbf{B}}{c} = -\frac{1}{n_e e} \nabla p_e, \quad (46)$$

where we write $\mathbf{u}_e \simeq \mathbf{u} - \mathbf{J}/n_e e$ for the bulk electron velocity. Taking the cross product of this equation with \mathbf{B} and solving for the bulk flow velocity $\mathbf{u}_{e,\perp}$ perpendicular to the magnetic field \mathbf{B} gives

$$\mathbf{u}_{e,\perp} = c \frac{\mathbf{E} \times \mathbf{B}}{B^2} + \frac{c}{n_e e B^2} \nabla p_e \times \mathbf{B}. \quad (47)$$

This equation implies the electron perpendicular bulk flow velocity is a sum of the $E \times B$ drift $c\mathbf{E} \times \mathbf{B}/B^2$ and the electron diamagnetic drift speed $\mathbf{u}_{*e} = c\nabla p_e \times \mathbf{B}/n_e e B^2$. This important result shows that the electron diamagnetic drift is captured in Hall-MHD provided the electron pressure is non-zero. An important implication of this is that magnetic flux convects at the sum of the $E \times B$ and electron diamagnetic drift speed when the electron pressure is retained in Ohm's law.

Gyrotropic Electron Pressure -

The next level of approximation for the electron pressure tensor is motivated by the fact that electrons in a magnetic field often have a different temperature in the directions parallel and perpendicular to the magnetic field, *i.e.*, the electrons are gyrotropic. The electron pressure parallel to the magnetic field is $p_{e,\parallel}$ and perpendicular to the magnetic field is $p_{e,\perp}$. The general way to write a gyrotropic electron pressure tensor

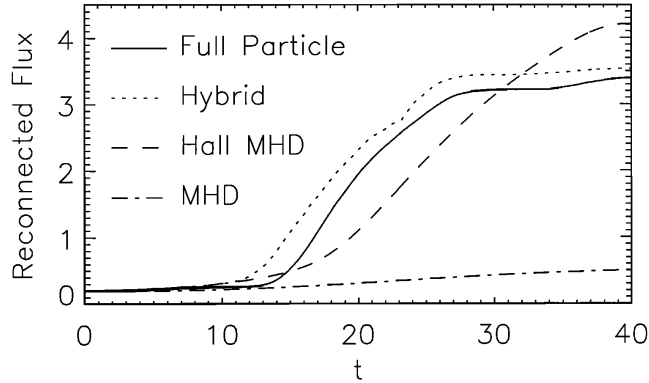


Fig. 3 “GEM Challenge” result showing Hall-MHD simulations faithfully obtain the rate of change of reconnected flux obtained in kinetic models. The legend describes the simulation approach for each curve; resistive-MHD is far slower than the other models. Adapted from [Birn et al. \(2001b\)](#).

$\mathbf{p}_{e,g}$ for a magnetic field in an arbitrary direction $\hat{\mathbf{b}} = \mathbf{B}/B$ is ([Parker, 1957a](#))

$$\mathbf{p}_{e,g} = p_{e,\perp} \mathbf{I} + (p_{e,\parallel} - p_{e,\perp}) \hat{\mathbf{b}} \hat{\mathbf{b}}. \quad (48)$$

Using this form in the generalized Ohm’s law for the electron pressure, and an analogous term in the pressure gradient force in the momentum equation allows for the modeling of a plasma with a gyrotropic pressure.

Having a closed set of equations requires closures on the parallel and perpendicular pressures. The most widely known closure is the Chew-Goldberger-Low (CGL) closure, which assumes that there is no heat flux and the plasma is magnetized ([Chew et al., 1956](#)). A direct calculation using the Vlasov equation and these assumptions gives the CGL “double adiabatic laws”

$$\frac{d}{dt} \left(\frac{p_{\perp}}{nB} \right) = 0, \quad \frac{d}{dt} \left(\frac{p_{\parallel} B^2}{n^3} \right) = 0, \quad (49)$$

A second model of great importance to reconnection is the Egedal closure ([Egedal et al., 2013](#)). This arises in the upstream and downstream regions of magnetic reconnection regions. The key physics is that the magnetic fields in this region are mirror fields that can trap electrons. The presence of an electric field heats them parallel to the electric field, leading to elongated gyrotropic distributions in the parallel direction. For large magnetic field strength, the equations reduce to the isothermal equation of state. For small magnetic field strength, the equations reduce to the CGL equations. The two limits were interpolated to find a closure that could be implemented into a fluid code; see [Egedal et al. \(2013\)](#) for details.

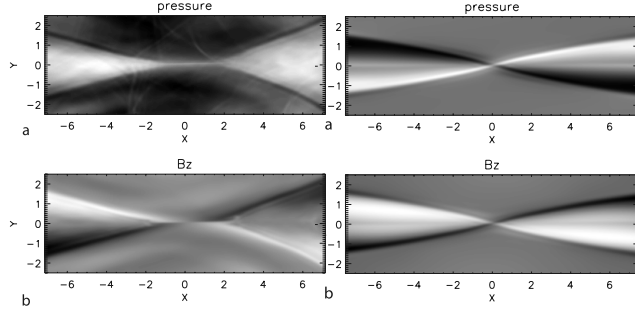


Fig. 4 Pressure and out-of-plane magnetic field in Hall MHD reconnection simulations. The legend describes the simulation approach for each curve; resistive-MHD is far slower than the other models. Adapted from [Rogers et al. \(2003\)](#).

3.8 Examples of Reconnection Simulation Results with the Hall Electric Field

The Hall-MHD model holds a significant place of importance in the history of reconnection simulations. From the earliest days of reconnection research, it was known that the Sweet-Parker model ([Sweet, 1958](#); [Parker, 1957b](#)) was too slow to explain solar flares ([Parker, 1963](#)), and it is also too slow to explain magnetotail reconnection ([Parker, 1973](#)) and the sawtooth crash in tokamaks ([Edwards et al., 1986](#); [Yamada et al., 1994](#)). It was discovered that using a localized resistivity leads to reconnection fast enough to explain the observed reconnection rates ([Ugai and Tsuda, 1977](#); [Sato and Hayashi, 1979](#)), but the resistivity model was not derived from first principles and it remains inconclusive whether it can be. Then, reconnection with the Hall electric field was found to also produce rates comparable to observed values without relying on ad hoc terms ([Aydemir, 1992](#); [Wang and Bhattacharjee, 1993](#); [Kleva et al., 1995](#); [Ma and Bhattacharjee, 1996](#)). The ‘‘GEM Challenge’’ study ([\(Birn et al., 2001a\)](#) and references therein), one of the most cited papers ever about reconnection, compared comparable simulations with different simulation models, and all models containing the Hall electric field led to fast reconnection with a reconnection rate approximately 0.1, as shown in [Fig. 3](#). It was only recently that an explanation of why the Hall electric field contributes to make the reconnection rate 0.1 was presented ([Liu et al., 2022](#)). Thus, Hall-MHD represents the minimal first-principles physics model that reproduces the reconnection rate achieved in kinetic models.

Another characteristic feature of collisionless reconnection is the quadrupolar structure of the out-of-plane magnetic field. For anti-parallel reconnection, it was posited that the Hall electric field would cause there to be a quadrupolar out-of-plane magnetic field due to the in-plane currents within the ion diffusion region (where the ions decouple from the magnetic field but the electrons remain frozen-in) ([Sonnerup, 1979](#)). Although this is a completely nonlinear effect, it is analogous to the out-of-plane magnetic field generation in the whistler wave shown in [Fig. 2\(b\)](#) ([Drake and Shay, 2007](#)). It can also be thought of as the out-of-plane current dragging the reconnecting field out of the reconnection plane ([Mandt et al., 1994a](#)). Hall-MHD simulations of reconnection produce a quadrupolar out-of-plane magnetic field ([Huba and Rudakov,](#)

2002), as shown in the lower left plot in Fig. 4 from simulations in Rogers et al. (2003). When there is a strong out-of-plane (guide) magnetic field, the quadrupolar structure persists, but a quadrupolar structure in the gas pressure also arises with opposite polarity (Kleva et al., 1995). The physical reason is analogous to the gas pressure perturbation formation in kinetic Alfvén waves as shown in Fig. 2(c). These quadrupolar structures arise in Hall-MHD simulations of reconnection, as shown in the right two panels of Fig. 4 from a simulation with guide field three times as strong as the reconnecting magnetic field. Despite the ability to produce quadrupolar structure in these quantities, it is now known that the detailed structure of the quadrupolar structures is not precisely the same as observed in kinetic simulations (Shay et al., 2007; Karimabadi et al., 2007) or magnetospheric observations (Phan et al., 2007). It was shown that the inclusion of an electron pressure anisotropy leads to better agreement with kinetic modeling (Ohia et al., 2012). An electron pressure anisotropy with the CGL relations and without the Hall term can also produce reconnection rates comparable to Hall reconnection (Cassak et al., 2015).

Another aspect of Hall-MHD reconnection that is not captured in collisional (Sweet-Parker) reconnection is how reconnection that is localized in the out-of-plane direction spreads in that direction. Spreading has been studied in a number of Hall-MHD studies (Huba and Rudakov, 2002; Shay et al., 2003; Huba and Rudakov, 2003; Karimabadi et al., 2004b; Nakamura et al., 2012; Shepherd and Cassak, 2012; Arencibia et al., 2021, 2022) and EMHD studies (Jain et al., 2013) and they agree with kinetic simulations of reconnection spreading (Lapenta et al., 2006). In particular, it was shown that anti-parallel reconnection does not spread in resistive-MHD, but it does spread in Hall-MHD and kinetic models (Nakamura et al., 2012; Arencibia et al., 2021).

An important issue related to Hall-MHD reconnection is its relation to the production of secondary islands. Secondary islands are rapidly produced during Sweet-Parker reconnection for large enough Lundquist number (Biskamp, 1986; Loureiro et al., 2007). It was argued on the basis of Hall-MHD simulations that the Hall effect prevents collisional reconnection effects from taking place (Cassak et al., 2005), and suppresses secondary islands via collisional effects once it starts (Shepherd and Cassak, 2010), which was also reported in kinetic simulations (Daughton et al., 2009). However, in Hall-MHD studies using island coalescence instead of a double Harris sheet, it was argued that collisionless secondary islands occur even after Hall-MHD effects take place (Huang et al., 2011). Collisionless secondary islands also arise in particle-in-cell kinetic simulations (Daughton et al., 2006).

3.9 The Future of Hall-MHD

Interestingly, many computational plasma physicists in the reconnection community are moving away from the Hall-MHD model and its fluid extensions to study the small-scale properties of reconnection. The Hall-MHD model was crucial for understanding the minimal physics that gives rise to a 0.1 reconnection rate. As questions have moved to other aspects of reconnection including heating and particle acceleration, many researchers opt for kinetic models to more realistically capture the small scale physics

than can be done with Hall-MHD. Treatments of particle acceleration and heating at large scales (Arnold et al., 2021) do not require the Hall electric field.

As example of an avenue of modern reconnection research and modeling where the Hall-MHD model remains highly beneficial is in the MHD-EPIC approach to global magnetospheric modeling (Daldorff et al., 2014a), as is discussed more fully in Sec. 6. In this approach, the fluid model is used in regions of the magnetosphere where no small important scale physics takes place, which allows for faster run times. In regions where small scale physics does take place, the code couples to a particle-in-cell code that captures this physics. The numerical results between the two models are passed back and forth to each other across their boundaries. The Hall-MHD model is well suited to be used in the transition region between the PIC and MHD models to facilitate a more accurate transition between the two models. The Hall-MHD model has been used to study global magnetospheric systems for Earth and other planets and moons to great effect (Paty and Winglee, 2004; Dorelli et al., 2015; Dong et al., 2019; Li et al., 2023), and it is anticipated that further advances will continue to be made with the Hall-MHD approach for systems too large to employ global kinetic codes.

4 Hybrid Simulations

The Earth’s magnetosphere is a complex plasma system characterized by a multitude of multiscale processes governing the interaction of the solar wind with the Earth’s dipole magnetic field. Modeling small-scale turbulent processes in the foreshock and magnetosheath requires inclusion of ion kinetic effects and Hall physics (Karimabadi et al., 2014; Omelchenko et al., 2021b). Furthermore, kinetic treatment of hot and cold ion populations is greatly needed for improved modeling of ionospheric outflows and their impact on the magnetopause and magnetotail. To study magnetic reconnection, one also needs to incorporate finite electron-mass effects (e.g. Biskamp, 2000; Birn and Priest, 2007; Gonzalez and Parker, 2016), or mimic these effects with *ad hoc* (resistivity) models.

The necessity to account for smaller and faster scales in kinetic simulations in a manner that would guarantee their numerical accuracy and computational efficiency creates challenges in global modeling of the Earth’s magnetosphere. Since describing plasma kinetics with pure “first-principles” models is still not feasible, various approximations have been developed as candidates for future “beyond MHD” operational modeling, with multiple levels of physical fidelity included. However, to what degree kinetic processes may influence the “fluid-like” behavior of the magnetosphere on global scales still remains an open question. As we argue below, many of these challenges can be addressed by self-consistent hybrid modeling, where Maxwell’s equations are solved in the quasi-neutral Darwin limit, ion species are treated kinetically, and the plasma electrons are approximated as an inertialess fluid. These hybrid models can be broken into two categories, according to the computational techniques used to represent kinetic ions: Particle-in-Cell (PIC) models (Winske et al., 2003; Lipatov, 2002b) and Vlasov models (von Alfthan et al., 2014). In what follows we discuss only the hybrid-PIC approach because it has already been applied successfully to perform three-dimensional (3D) simulations of global plasma systems that range from

the Earth’s magnetosphere (e.g. Lin and Wang, 2005; Omelchenko et al., 2021b), planets (Herčík et al., 2013; Jarvinen et al., 2020), and small space bodies (Fatemi et al., 2017; Kallio et al., 2019) to compact laboratory plasmas (Omelchenko and Sudan, 1997; Lin et al., 2008; Thoma et al., 2013; Omelchenko, 2015; Omelchenko and Karimabadi, 2022). The hybrid-Vlasov approach (von Alfthan et al., 2014) is relatively new and considerably more computationally expensive, with production runs being still restricted to quasi-3D setups (Pfau-Kempf et al., 2020a).

An important issue to grasp reconnection correctly is the consideration of the finite electron inertia, as it has been shown by EMHD simulations. This could reveal not only the properties of electron-only reconnection, proposed by (Jain and Sharma, 2009) and recently discovered by MMS in the magnetosheath (Phan et al., 2018), but also the transition from electron- to ion reconnection. These effects can be treated by hybrid-approach with kinetic ions and an inertial electron fluid 4.4.

4.1 Model Equations - massless electrons

The standard hybrid model (Winske et al., 2003) assumes plasma quasi-neutrality, neglects the displacement current in Maxwell’s equations, and treats ions as full-orbit macro-particles (in the PIC approach) moving in self-consistent electric and magnetic fields. The plasma electrons are approximated as an inertialess fluid with scalar pressure described by either an adiabatic law or evolution equation. Together with a self-consistent PIC method for the ion components, this leads to a set of hybrid equations that include Ampere’s law in the magnetostatic limit, Faraday’s law, and an algebraic expression for electric field (generalized Ohm’s law) with the Hall, electron pressure gradient, and resistive terms (e.g. Omelchenko and Karimabadi, 2012):

$$\nabla \times \mathbf{B} = \frac{4\pi}{c} \mathbf{J}, \quad \mathbf{J} = \mathbf{J}_e + \mathbf{J}_i, \quad (50)$$

$$\frac{\partial \mathbf{B}}{\partial t} = -c \nabla \times \mathbf{E}, \quad (51)$$

$$\mathbf{E} = \frac{\mathbf{J}_e \times \mathbf{B}_t}{en_e c} - \frac{\nabla p_e}{en_e} + \eta \mathbf{J}, \quad \mathbf{B}_t = \mathbf{B} + \mathbf{B}_{ext}, \quad (52)$$

$$en_e = \rho_i, \quad (53)$$

$$p_e = n_e T_e \sim n_e^\gamma. \quad (54)$$

In Eqs. (52-54) n_e, \mathbf{J}_e are the electron number and current density, respectively; p_e is the electron pressure, here assumed to be governed by Eq. (54) with an adiabatic constant of γ ; T_e is the electron temperature; ρ_i, \mathbf{J}_i are the total ion charge and current density (found by the PIC method); \mathbf{E} is the electric field; $\mathbf{B}, \mathbf{B}_{ext}$ are the “self-generated” ($\mathbf{B}|_{t=0} = 0$) and “external” (steady state) magnetic fields, respectively.

The applied plasma resistivity, η is either constant or chosen to be a function of plasma parameters (e.g. Lin et al., 2007; Omelchenko et al., 2021b). The resistive term in the generalized Ohm’s law (Eq. (52)) may (i) describe finite conductivity of plasma or space bodies (e.g., the Moon (Fatemi et al., 2017; Omelchenko et al., 2021c)), (ii) imitate finite electron inertia effects in magnetic reconnection events, and (iii) enable fast magnetic field diffusion at low-density (“vacuum”) cells, $n_e \leq n_{min}$, where n_{min} is

a small density cutoff value (Omelchenko et al., 2021c). Failure to properly treat low-density regions in hybrid simulations may lead to non-physical results (Omelchenko et al., 2021c; Poppe, 2019).

4.2 Key Physics Beyond MHD in Hybrid Models

The “mesoscale” hybrid model occupies the middle ground between the “large-scale” fluid and “micro-scale” first-principles modeling paradigms. For global magnetospheric simulations, the hybrid model enables a number of “beyond MHD” capabilities, as explained below.

Modeling turbulent processes in the foreshock and magnetosheath. Unless large resistive damping (or smoothing) is applied, the hybrid model accurately captures the Hall physics for mesh cell sizes, $\Delta \leq d_i$, where $d_i = c/\omega_{pi}$ and ω_{pi} are the local ion inertial length and plasma frequency, respectively. The Hall effects phase out on coarser meshes, $\Delta \gg d_i$, where the Alfvén term becomes greater than the Hall term in Eq. (52) and the whistler mode frequency, $\propto \Delta^{-2}$ becomes lower than the Alfvén mode frequency, $\propto \Delta^{-1}$. In fact, in this case the Hall term can completely be removed from the electric field in Faraday’s law (Eq. (51)) and kept only in the equations of ion motion (Karimabadi et al., 2004a). The ability of a hybrid code with the Hall term to run stably on coarser meshes ($\Delta \gtrsim d_i$) may depend on the numerical implementation of Faraday’s law (Omelchenko and Karimabadi, 2012).

Global hybrid codes have been used to address the ultra-low frequency (ULF) physics of the curved bow shock on the ion inertial/Larmor radius scales as the physics of the bow shock is predominantly determined by kinetic physics associated with charged particles from the solar wind. Of particular interest are the foreshock waves and diffuse ion distributions (Wang et al., 2009) and transient perturbations originating from the wave-particle processes in the quasi-parallel shock or due to the shock interaction with incoming solar wind discontinuities, including hot flow anomalies (Lin, 2002; Lin et al., 2022b), foreshock bubbles (Omidi et al., 2010; Wang et al., 2020a), foreshock cavities (Lin and Wang, 2005; Blanco-Cano et al., 2011), and high-speed jets (Omelchenko et al., 2021a; Palmroth et al., 2018b). The 3D hybrid simulations with ANGIE3D link the foreshock perturbations to the surface perturbations and kinetic-scale shear Alfvén waves (KAWs) at the magnetopause through mode conversion from the incoming compressional waves (Lin and Wang, 2005; Shi et al., 2013), as well as the subsequent excitation of toroidal-mode field line resonances in the magnetosphere (Shi et al., 2021). It has also been shown that 3D models are essential for addressing the nonlinear physics of mode coupling and ion diffusion at the magnetopause (Lin et al., 2012).

The whistler mode plays a significant role in regulating turbulence in the magnetosheath and mediating magnetic reconnection in the Earth’s magnetosphere (e.g. Dorelli and Birn, 2003; Drake et al., 2008). Hybrid simulations generally have to resolve the quadratic dispersion of this mode, $\omega \propto k^2$. This requirement may create computational bottlenecks in simulations of strongly inhomogeneous magnetospheric and laboratory plasmas, where whistler timescales typically span several orders of magnitude (Omelchenko and Karimabadi, 2012, 2022). If not accurately integrated in time (or resistively damped), the spurious short-wavelength oscillations may grow

explosively unstable from noise and terminate simulation (Lin et al., 2008). It should also be noted that although particle noise in hybrid-PIC simulations typically degrades their physical resolution, the Lagrangian (particle) approach enables transport of ion species with less numerical diffusion compared to the Eulerian approach to solving the Vlasov equation on velocity meshes (von Alfthan et al., 2014).

Collisionless reconnection at the magnetopause and in the tail plasma sheet. The physics of magnetic reconnection in the magnetosphere can be investigated by carrying out global hybrid simulations with an ad-hoc current-dependent resistivity. For the dayside magnetopause, the modeling topics include the structures of ion diffusion region and outflow regions (Tan et al., 2011), global evolution of flux transfer events (FTEs) and magnetic flux ropes (Omidi and Sibeck, 2007; Guo et al., 2020, 2021a), propagation of kinetic Alfvén waves and Poynting flux from reconnection (Wang et al., 2019), ion cusp precipitation and energy spectrum (Omidi and Sibeck, 2007; Tan et al., 2012), the triggering of reconnection by solar wind discontinuities (Omidi et al., 2009; Pang et al., 2010; Guo et al., 2021d), and magnetosheath turbulence (Chen et al., 2021; Ng et al., 2021). Likewise, high-latitude reconnection tailward of the cusp under northward IMF has also been simulated (Lin and Wang, 2006; Guo et al., 2021b). The 3D global physics of storm-time magnetotail reconnection, fast flow and entropy bubbles, the Hall-effects control of dawn-dusk asymmetry (Lin et al., 2014; Lu et al., 2016; Lin et al., 2017), and the associated global Alfvénic coupling between the magnetotail and the ionosphere under southward IMF have been simulated using the ANGIE3D code (Cheng et al., 2020). Attempt has also been made to investigate the subsequent connection of fast flows to the ring current and radiation belt by combining ANGIE3D with the CIMI inner magnetosphere model (Lin et al., 2021a).

Inclusion of multi-species plasma ion populations of solar wind origin and improved representation of ionospheric outflow. In general, global hybrid models may include multiple ion species for representing solar wind and ionospheric outflow plasmas. Ionospheric outflow ions should be treated kinetically and self-consistently in order to properly account for their impact on the Earth’s magnetosphere. Multi-fluid MHD models do not account for ion resonance acceleration and cyclotron effects, especially for heavy ions (Toledo-Redondo et al., 2021). Self-consistent 3D hybrid simulations of the impact of oxygen outflow on the magnetotail configuration and stability have recently been performed with the HYPERS code (Mouikis et al., 2021; Omelchenko et al., 2022).

Modeling local reconnection and electron scale physics. In MHD simulations, magnetic reconnection is often a result of mesh-dependent diffusion that is difficult to control numerically. The hybrid-PIC model is inherently more robust in this regard because ions are modeled as Lagrangian particles. As a result, reconnection onset and dynamics are controlled by the Hall physics and parameter-dependent resistivity. The hybrid-PIC model is also known to accurately reproduce reconnection rate when the ion inertial and cyclotron scales are properly resolved (Stanier et al., 2015). Further modifications of the hybrid model, which for instance may incorporate finite electron mass effects (e.g. Omelchenko et al., 2021d), could increase physical fidelity of reconnection modeling in the future.

Modeling non-MHD waves in a global context. The standard hybrid model supports ion cyclotron, whistler, and kinetic-Alfvén wave modes, which play an important role in regulating plasma turbulence in the Earth’s magnetosphere and impact its global behavior. Modern observations report streams of non-Maxwellian ions that excite plasma turbulence through numerous kinetic instabilities that cannot be modeled within MHD. Global hybrid modeling naturally incorporates the ion kinetic effects into global models of the Earth’s magnetosphere, which helps advance our understanding of the effects of turbulent plasma dynamics on global physical processes.

Other applications. 3D hybrid codes in space physics have been used to simulate shock-driven ion acceleration (Caprioli, 2014; Guo and Giacalone, 2013), solar wind turbulence (Franci et al., 2018; Roytershteyn et al., 2015), the Moon’s wake (Fatemi et al., 2017; Kallio et al., 2019; Omelchenko et al., 2021c), planetary magnetospheres (Jarvinen et al., 2020), and small space bodies (Alho et al., 2019; Delamere, 2009). Comparing results from full-scale 3D hybrid simulations of small space bodies with satellite observations provides yet another important route for validation and further extension of the hybrid approach to plasma modeling. Importantly, the recent advances in ionosphere-magnetosphere coupling (Lin et al., 2022c), code optimization (Dong et al., 2021) and multiscale computing (Omelchenko et al., 2021b) have greatly improved the prospects for hybrid simulations to become a key factor to consider in the overall theory of global solar wind-magnetosphere-ionosphere interactions.

4.3 Numerics

Eqs. (52-54), together with the self-consistent equations of motion for the ion macroparticles, may present computational challenges when used for modeling complex 3D plasma systems, such as the Earth’s magnetosphere. Below we discuss some recent computational advances aimed at overcoming these problems.

4.3.1 Spatial Scales

Hybrid-PIC simulations typically intend to resolve the spatial scales of the order of the ion inertial length, d_i and ion cyclotron radius, r_{ci} . The physical validity regime of the hybrid model ranges from large MHD scales down to $kr_{ci} \sim 1$ and $\omega t \sim 1$. The actual physical resolution of a hybrid simulation is largely determined by (i) how well these characteristic lengths are resolved on a mesh, (ii) how many particles are used. For the typical solar wind proton inertial length, $d_i \sim 100 \text{ km}$, the Earth’s radius, $R_E \sim 60d_i$. To encompass the whole magnetosphere, the computational mesh in a global simulation should cover the magnetopause with a typical standoff distance, $R_{MP} \sim 10R_E \sim 600d_i$ and the magnetotail stretching from the Earth to far distances, $R \sim 100R_E \sim 6000d_i$. The need to accurately account for the “far-field” inflow and outflow boundary conditions in the presence of a magnetic dipole may additionally require multiplying these dimensions by a factor of 2-3. Approximating such large 3D domains with uniform meshes with cell sizes of the order of $\sim 1d_i$ is prohibitively expensive for the hybrid model because of the need to advance ions and fields at all cells on kinetic scales.

To overcome these restrictions, several options are available. First, one may increase the cell size beyond $1d_i$ at the expense of lower accuracy in resolving the Hall physics (Omelchenko and Karimabadi, 2012). Second, one may artificially increase the ratio between the solar wind ion inertial length d_i ($d_i \sim r_{ci}$ for the outer magnetosphere regions with ion $\beta \sim 1$) and the magnetopause distance R_{MP} , in order to better accommodate the available computation resources while still choosing a sufficiently large value of R_{MP}/d_i for assuring the separation between the global and local-kinetic scales (Omidi et al., 2004). Both approaches efficiently “downscale” the Earth’s magnetosphere. For instance, ANGIE3D (Lin et al., 2014; Lin and Wang, 2005) does it by artificially reducing the solar wind plasma density, i.e. by inflating the characteristic inertial ion length and proportionally increasing the Alfvén speed. Alternatively, H3D (Karimabadi et al., 2014), hybrid-VPIC (Dong et al., 2021), and HYPERS (Omelchenko and Karimabadi, 2012) employ the physical ion inertial length but scale the realistic magnetopause standoff distance down by a factor of 4-6 by using a weaker magnetic dipole.

Regardless of a chosen magnetosphere scaling method, present-day 3D hybrid codes typically use $R_{MP}/d_i \geq 100$. One of the largest 3D hybrid simulations to date was performed with HYPERS for $R_{MP}/d_i \simeq 160$ on a uniform mesh with approximately $1000 \times 2000 \times 2000$ cells (Omelchenko et al., 2021c). To speed up global 3D simulations, hybrid codes may employ nonuniform meshes, among which ‘stretched’ (logically mapped) Cartesian meshes are the simplest. Nonuniform meshes typically maintain high resolution in a central domain of interest, while expanding cells towards domain boundaries (Omelchenko et al., 2021b; Lin and Wang, 2005) to guarantee that the dipole field vanishes at the inflow/outflow (GSM X) and lateral (GSM Y and Z) boundaries so that robust local boundary conditions can be implemented. Sometimes, for simplicity, the lateral domain boundaries may be assumed to be periodic ((e.g. Turc et al., 2015; Müller et al., 2011)). This simplification, however, makes a global simulation valid for shorter simulation periods, until reflected particles or electromagnetic perturbations reach the periodic boundaries. To improve the counting statistics for macro-particles, splitting techniques may be used to enhance energetic particle distributions in the dayside magnetosphere (Omelchenko et al., 2021a) and magnetotail (Lin et al., 2007; Wang et al., 2009).

To further reduce the number of computational cells in global simulations, one may employ curvilinear (e.g., spherical) meshes ((e.g. Dyadechkin et al., 2013; Guo et al., 2021c)). For example, to capture the short-wavelength physics along the shock normal and the magnetopause, early hybrid simulations, focusing on the dayside regions, employed cylindrical (2D) (Swift, 1996; Lin et al., 1996; Lin, 2002) and spherical (3D) (Lin and Wang, 2005) coordinate systems. The spherical coordinate lines, however, have a singularity on the polar axis, which was handled by rotating the polar coordinates to the equator and omitting a conic region around them, while keeping the physical polar regions inside the domain (Lin and Wang, 2005). A 2D hybrid simulation of the magnetotail also used curvilinear coordinates to accommodate the tail geometry (Swift and Lin, 2001; Lin, 2002). Similar to the need of assuring proper numerical resolution for resolving the kinetic scales along the curved or oblique boundary surfaces on the Cartesian meshes, special care is also necessary for the curvilinear

meshes, especially when their coordinate lines are not orthogonal (Swift and Lin, 2001). Compared to Cartesian meshes, curvilinear meshes may introduce additional discretization errors due to their (i) typically lower orders of numerical approximation, (ii) anisotropic particle-mesh weighting. These errors lead to various numerical artefacts and non-conservation of particle momentum (“self-forces”). As a result, it is necessary to benchmark results from simulations obtained with curvilinear meshes with similar simulations performed with Cartesian meshes (Dyadechkin et al., 2013).

Some global hybrid codes employ adaptive mesh refinement (AMR) (Leclercq et al., 2016; Müller et al., 2011). Hybrid AMR simulations, however, may suffer from spurious particle “self-forces” and wave reflections that occur at the mesh refinement interfaces. To mitigate these artefacts, AMR algorithms are typically complemented with smoothing procedures, which, however, should be performed with caution in order to avoid affecting underlying physics in the regions of interest.

4.3.2 Temporal Scales

In addition to the “slow” Alfvénic (MHD) timescales, hybrid codes need to follow the “fast” ion kinetic, ion cyclotron and whistler timescales. This requirement typically makes global hybrid simulations numerically “stiff” in the near-Earth space, where timesteps, required for numerical accuracy and stability, may become prohibitively small (Omelchenko and Karimabadi, 2012). To partially mitigate these effects, the kinetic ions may be replaced in this region by a dense fluid (Swift, 1996; Lin et al., 2021b). Hybrid-PIC simulations inherently generate spurious oscillations with large wave numbers, $k \sim 1/\Delta$ and high frequencies, $\omega \sim k^2 \sim 1/\Delta^2$. If not properly integrated or resistively damped, these noisy oscillations may explosively grow and abort simulation (Lin et al., 2008). Deleterious instabilities may be avoided by applying “noise filtering” (smoothing) or/and various “flux-limiting” techniques for electric and magnetic fields. These modifications, however, need to be implemented with caution, as they may produce artificial solutions not supported by the hybrid model.

For accuracy, typical full-orbit particle solvers (“pushers”) require that timesteps, Δt_p should be small enough that $\Omega \Delta t_p \ll 1$, where Ω is the local ion gyro-frequency. Using the same timestep for all particles may create another numerical bottleneck in global hybrid simulations of the Earth’s magnetosphere. For instance, particle timesteps of the order of $\Omega_0 \Delta t_p \sim 0.05$ (where Ω_0 is the ion gyro-frequency computed with respect to the IMF strength, B_{IMF}) fairly well describe ion gyro-motion in the solar wind ((e.g. Turc et al., 2015; Guo et al., 2021c)). At the same time, gyro-orbits and drifts of ions with $\Omega \gtrsim 10 \Omega_0$ (e.g. found in the cusp or some parts of the magnetosheath), will not be reproduced with accuracy. As a remedy, in some simulations, sub gyro-orbit time steps may be employed in these (large magnetic field) regions of the magnetosphere (Lin et al., 2014).

To summarize, predicting optimum global timesteps for the particles and fields in global hybrid simulations is difficult in practice. This challenge has been addressed by replacing time stepping with an asynchronous approach to time integration, which combines discrete-event simulation (DES) with elements of artificial intelligence: Event-driven Multi-Agent Planning System (EMAPS) (Omelchenko and Karimabadi, 2006b, 2022). EMAPS enables time advance of individual particles and local fields

on meshes of arbitrary topology by integrating them on their self-adaptive timescales in a “game of life” fashion. Thus, EMAPS effectively performs the role of an intelligent “simulation time operating system”. This approach was first applied to model 1D collisionless plasma shocks (Omelchenko and Karimabadi, 2006a) and fluids (Omelchenko and Karimabadi, 2006b, 2007). Implemented in HYPERS (Omelchenko and Karimabadi, 2012), EMAPS has enabled efficient and accurate global 3D hybrid simulations of the Earth’s magnetosphere (Omelchenko et al., 2021b,c, 2022).

Global 3D hybrid simulations of the Earth’s magnetosphere are typically performed for simulation periods, $\Omega_0 t \sim 100 - 500$, where Ω_0 is the IMF based proton cyclotron frequency. Assuming $B_{IMF} = 5 \text{ nT}$, these simulations formally span relatively short (compared to MHD) magnetospheric times, $t < 20 \text{ min}$. For convenience, in order to present physical results in “magnetospheric hours”, some modelers multiply this simulation time by a model scaling factor (Lin et al., 2022c). Although this scaling is useful for comparing “macro-scale” simulation phenomena with observations, it is not appropriate for describing ion kinetic effects, e.g. those that drive the “magnetokinetic” formation of high-speed jets (Omelchenko et al., 2021b).

4.3.3 Plasmasphere and Ionosphere

Currently, hybrid codes cannot model global magnetospheric convection lasting many hours or days, e.g. a steady-state process of magnetotail loading and unloading. Therefore, global hybrid models typically assume a simple perfectly conducting or resistive ionosphere, where dipole magnetic field lines are “tied up” to the inner boundary (zero electric field) or allowed to diffuse due to its finite resistivity, respectively. model (e.g. Lin et al., 2021b),

To avoid computing fast kinetic timescales, a cold, incompressible, dense ion fluid may be assumed to co-exist together with low-density particle ions in the inner magnetosphere within the distance of plasmasphere, where the plasma density is high (Swift, 1996; Lin and Wang, 2005; Lin et al., 2014). In ANGIE3D, this region is bounded by the near-Earth (inner) boundary, which is located at a radial distance at $r \simeq 3.5 R_E$ in the inner magnetosphere. The field-aligned currents, calculated near this inner boundary and mapped along the geomagnetic dipole field lines down to the ionospheric altitude (1,000 km), are used as input to the ionospheric potential equation solved on a sphere (Lin et al., 2014, 2021a):

$$\nabla \cdot (-\Sigma \cdot \nabla \Phi) = J_{\parallel} \sin I, \quad (55)$$

where Σ is the conductance tensor, Φ is the electric potential, J_{\parallel} is the mapped field-aligned current density, and I is the inclination of the dipole field at the ionosphere. The static analytical model of Hall and Pederson conductance that accounts for EUV and diffuse auroral contributions can be used for the conductance tensor. Similarly to the global MHD models, the ionospheric electric field is mapped along the dipole lines back to the inner magnetospheric boundary, to serve as a boundary condition for the cold ion fluid (Lin et al., 2021b).

4.4 Hybrid simulations with inertial electrons and EMHD simulations

The MMS mission investigates physical processes like magnetic reconnection, shock waves and turbulence, which span from ion to electron scales. Simulation studies of these processes should ideally cover full kinetic physics from ion to electron scales for which the necessary present and near-future computational resources are prohibitively expensive. Therefore simulation models, which cover different scale ranges and physical phenomena, are used.

Hybrid-kinetic plasma simulation model, introduced in the previous section 4.1, treats ions as kinetic species and electrons as a massless fluid. This restricts their applicability to physical processes in which not only electron kinetic effects are not important but also to the scales exceeding by far the electron scales. Hybrid-kinetic codes with inertia-less electrons, discussed in section 4.1, can, therefore, be used to simulate global phenomena and in some cases for specifically limited physics studies of magnetic reconnection, plasma turbulence and shock waves.

The validity of hybrid-kinetic model can, however, be extended down to electron length scales, viz., to electron inertial length by considering electrons as an inertial fluid (Jain et al., 2023). Since the electron kinetic physics is still ignored such plasma model might computationally be more feasible than the fully kinetic model and describe larger scale phenomena and plasma process like magnetic reconnection, plasma turbulence and shock formation in collisionless plasmas, in which electron scale structures develop.

4.4.1 Model equations - inertial electrons

Hybrid-kinetic model treats ions as kinetic species and electrons as an inertial fluid. In hybrid-kinetic simulation codes, ion dynamics can be described by solving either the ion's Vlasov equation using Eulerian methods or the equations of motion for ion macro-particles using semi-Lagrangian Particle-in-Cell (PIC) method. Solving Vlasov equation is computationally more expensive. Here we discuss the hybrid-PIC codes which treat ions as Lagrangian macro-particles modelled via the PIC method. Following are the governing equations of hybrid-PIC model.

$$\frac{d\mathbf{x}_i}{dt} = \mathbf{v}_i, \quad (56)$$

$$m_i \frac{d\mathbf{v}_i}{dt} = e(\mathbf{E} + \frac{\mathbf{v}_i \times \mathbf{B}}{c}), \quad (57)$$

$$\nabla \times \mathbf{E} = -\frac{1}{c} \frac{\partial \mathbf{B}}{\partial t}, \quad (58)$$

$$\nabla \times \mathbf{B} = \frac{4\pi}{c} \mathbf{J}, \quad (59)$$

$$\mathbf{J} = e(n_i \mathbf{u}_i - n_e \mathbf{u}_e), \quad (60)$$

$$n_i = n_e \quad (61)$$

$$\mathbf{E} = -\frac{\mathbf{u}_e \times \mathbf{B}}{c} - \frac{1}{en} \nabla p_e - \frac{m_e}{e} \left(\frac{\partial \mathbf{u}_e}{\partial t} + (\mathbf{u}_e \cdot \nabla) \mathbf{u}_e \right) + \eta \mathbf{J}, \quad (62)$$

$$p_e = C n_e^\gamma \quad (63)$$

The electric and magnetic fields (\mathbf{E} and \mathbf{B} respectively) in Maxwell's equations, Eqs. (58) and (59), are coupled to the plasma dynamics via the total current density $\mathbf{J} = e(n_i \mathbf{u}_i - n_e \mathbf{u}_e)$ resulting from the bulk motion of ions (number density n_i , bulk velocity \mathbf{u}_i) and electrons (number density n_e , bulk velocity \mathbf{u}_e). Ion's number density n_i and the bulk velocity \mathbf{u}_i is obtained from their positions \mathbf{x}_i and velocities \mathbf{v}_i governed by Eqs. (56) and (57). Electron dynamics is governed by quasi-neutrality condition, Eq. (61), momentum equation of the inertial electron fluid, Eq. (62), and equation of state relating electron scalar pressure p_e with electron number density n_e , Eq. (63). Here, e is the fundamental charge, m_i ion mass, m_e electron mass, μ_0 magnetic permeability of vacuum, η collisional resistivity, γ the adiabatic constant and C is a constant (to be determined from initial conditions). Eqs. (56)-(63) are the fundamental equations of the hybrid-kinetic model with inertial electron fluid (Jain et al., 2023). These equations differ from the equations of hybrid-kinetic model with inertia-less electron fluid only by the electron inertial terms proportional to m_e on the RHS of Eq. (62). Addition of electron inertial terms in Eq. (62) makes the numerical solution of these equations much more involved in comparison to the case of inertia-less electron fluid. The algebraic calculation of electric field from Eq. (62) is not as straightforward as in the case of the inertia-less electron fluid. One needs to now calculate time derivative of \mathbf{u}_e or find some other way to obtain electric field. The calculation of magnetic field also now requires numerical solution of additional elliptic partial differential equations arising because of the finite electron inertia.

In majority of the hybrid-kinetic codes with inertial electrons, evolution of magnetic field is followed by solving an evolution equation for the generalized vorticity $\mathbf{W} = \nabla \times \mathbf{u}_e - e\mathbf{B}/m_e c$ obtained by taking curl of Eq. (62) and using Eq. (58). This equation is,

$$\frac{\partial \mathbf{W}}{\partial t} = \nabla \times [\mathbf{u}_e \times \mathbf{W}] - \nabla \times \left(\frac{\nabla p_e}{m_e n} \right) - \nabla \times \left(\frac{e\eta}{m_e} \mathbf{J} \right). \quad (64)$$

The magnetic field is then calculated by solving an elliptic partial differential equation (PDE) which is obtained by substituting for \mathbf{u}_e from Eq. (59) and (60), $\mathbf{u}_e = \mathbf{u}_i - c \nabla \times \mathbf{B} / (4\pi en)$, in the expression for $\mathbf{W} = \nabla \times \mathbf{u}_e - e\mathbf{B}/m_e c$.

$$\frac{c}{4\pi e} \nabla \times \left(\frac{\nabla \times \mathbf{B}}{n} \right) + \frac{e\mathbf{B}}{m_e c} = \nabla \times \mathbf{u}_i - \mathbf{W}. \quad (65)$$

Some of the hybrid-kinetic codes make approximations of electron inertial terms in Eq. (62) and (65) to simplify their numerical solutions (Lipatov, 2002a; Shay et al., 1998; Kuznetsova et al., 1998). Spatial density variations are neglected in Eq. (65) (Shay et al., 1998; Kuznetsova et al., 1998). The electric field was then calculated from the generalized Ohm's law by neglecting the electron inertial term with

time derivatives of the electron fluid velocity (Kuznetsova et al., 1998). Some codes neglected even the convective electron acceleration term (Shay et al., 1998). These approximations are valid when length scale of variations is much larger than the electron inertial length. For a detailed discussion of these approximations, see Munoz et al. (2018) (Muñoz et al., 2018). These hybrid-kinetic codes which partially included electron inertial effects have mainly been used to study collisionless magnetic reconnection (Shay et al., 1999; Kuznetsova, 2000; Kuznetsova et al., 2001). In particular Shay et al. (1998) used an evolution equation for a scalar electron pressure (Shay et al., 1998) while Kuznetsova et al. (1998) included the full electron pressure tensor to take into account the non-gyrotropic effects (Kuznetsova et al., 1998).

More recently a hybrid-kinetic code CHIEF (Code Hybrid With Inertial Electron Fluid) was developed (Muñoz et al., 2018). This code solves Eqs. (62) and (65) without making any of the electron inertia related approximations used by other codes. The details of the numerical algorithm to solve Eqs. (56)-(63) are discussed by Munoz et al. (2018) (Muñoz et al., 2018). CHIEF was used to simulate kinetic plasma turbulence and it was found that the electron inertia related approximations are not valid in electron scale current sheets formed in the turbulence (Jain et al., 2022; Muñoz et al., 2023).

Some hybrid-kinetic codes with electron inertia calculate electric field from an elliptic PDE instead of Eq. (62) (Amano et al., 2014; Valentini et al., 2007). The elliptic PDE for the electric field is obtained by taking curl of Faraday’s law, Eq. (58), and utilizing Eqs. (59) and (62). Electron inertia effects were considered in the elliptic equation for the electric field while, still, the electron inertia term was ignored that contains the divergence of the electric field. Two dimensional simulations of kinetic plasma turbulence have shown that this approximation is not valid from ion to electron scales (Jain et al., 2022).

4.4.2 EMHD model: A special case of Hybrid-kinetic model with electron inertia in the limit of static ions

Electron-magnetohydrodynamic (EMHD) model can be obtained as a special case of hybrid-kinetic model by taking the limit of stationary ions. However, it can also be obtained in the same manner from the Hall MHD equations (see Sec. 3.7.2). In this model, ions provide a stationary charge neutralizing background for the electron dynamics. It can be applied to non-kinetic plasma processes at electron space and time scales during which ions do not respond or even at scales larger than electron scales as long as ions are stationary by some mechanism, e.g., fixed in lattice (Gordeev et al., 1994). EMHD model has been applied in the past to electron scale magnetic reconnection (Bulanov et al., 1992; Mandt et al., 1994b; Drake et al., 1994, 1997; Attico et al., 2000; Chacón et al., 2007; Zocco et al., 2009; Jain and Sharma, 2009; Jain et al., 2012; Jain and Büchner, 2015; Jain and Sharma, 2015a,b) and is applicable to the electron-only reconnection recently discovered by MMS observations (Phan et al., 2018).

Equations of EMHD can be derived from the equations of hybrid kinetic model with electron inertia, Eqs. (56)-(63), by setting $\mathbf{u}_i = 0$. In this limit, Eq. (59) and (65)

become,

$$\mathbf{u}_e = -\frac{c}{4\pi ne} \nabla \times \mathbf{B}, \quad (66)$$

$$\mathbf{W} = -\frac{c}{4\pi e} \nabla \times \left(\frac{\nabla \times \mathbf{B}}{n} \right) - \frac{e\mathbf{B}}{m_e c}. \quad (67)$$

Here $n = n_i = n_e$ is constant as ions are stationary. Equations (64), (66) and (67) form a closed set of equations for the evolution of magnetic field in EMHD model.

4.4.3 Electron only reconnection: importance of electron inertia

In many of electron only reconnection events observed by MMS, guide magnetic field is significantly larger than the asymptotic value of the reconnecting component of magnetic field (Phan et al., 2018; Zhou et al., 2021; Man et al., 2020; Stawarz et al., 2022). In the statistical survey of electron only reconnection events in Earth's magnetosheath, guide field in majority of the events is 1 to 10 times larger than the reconnecting component of the magnetic field (Stawarz et al., 2022). MMS observations of electron scale reconnection in Earth's magnetosheath show that the electron non-gyrotropy, which balances the reconnection electric field in weak or zero guide field case, reduces with the increasing strength of the guide magnetic field (Wilder et al., 2018). No evidence of agyrotropy was found in another MMS observations of large guide field reconnection (Eriksson et al., 2016). This is consistent with the fact that a strong guide magnetic field will magnetize electrons in the electron diffusion region not allowing non-gyrotropy to develop if the scale length of the diffusion region is larger than the electron Larmor radius in the guide field.

In the case of the large guide magnetic field and thus weak or zero non-gyrotropy, the reconnection electric field is expected to be balanced by electron inertial terms in generalized Ohm's law. Indeed, PIC simulations of magnetic reconnection have shown that electron inertial terms are significant to balance the reconnection electric field when guide field is large and/or current sheet has electron scale thickness (Hesse and Winske, 1998; Hesse et al., 2016; Liu et al., 2013; Pritchett, 2005). For the electron only events observed with large guide magnetic field and/or absence of non-gyrotropy, electrons can be modeled as an inertial electron fluid as is done in hybrid kinetic simulations with electron inertia which are computationally less expensive in comparison to fully kinetic simulations.

4.4.4 Magnetic reconnection through electron scale current sheets: EMHD simulations

Hybrid kinetic simulations of turbulence with electron inertia show that the physics of electron only reconnection can be described by equations of an Electron-magnetohydrodynamic (EMHD) model which is a special case of hybrid-kinetic model with electron inertia in the limit of stationary and un-magnetized ions (see section 4.4.2). This is expected as the ions do not couple in electron only reconnection events. Collisionless magnetic reconnection in electron scale current sheets has been investigated using EMHD model for several decades before the observational discovery of

electron-only reconnection by MMS (Bulanov et al., 1992; Mandt et al., 1994b; Drake et al., 1994, 1997; Attico et al., 2000; Chacón et al., 2007; Zocco et al., 2009; Jain and Sharma, 2009; Jain et al., 2012; Jain and Büchner, 2015; Jain and Sharma, 2015a,b). It was, however, not termed as electron only reconnection as it was not conceived at that time that reconnection without ion participation is possible. It was rather termed as “early phase of reconnection” (Jain and Sharma, 2009; Jain et al., 2012; Jain and Sharma, 2015a,b). Later, electron only reconnection in Earth’s magnetotail was also interpreted as an early phase of the standard reconnection (Hubbert et al., 2022; Farugia et al., 2021) and there is ongoing discussion if the observed reconnection events without ion coupling are electron-only reconnection events or just an early phase of standard reconnection (Lu et al., 2020, 2022; Wang et al., 2020b; Yi et al., 2022).

Jain and Sharma (2009) were the first to propose that the early phase of reconnection after its onset in electron scale current sheets will be dominated by electron dynamics without coupling to ion dynamics and carried out EMHD simulations to study the physics of the early phase. This study was followed by further theoretical and simulation studies, both in 2-D and 3-D, using EMHD model and comparison with space observations by Cluster spacecraft (Jain et al., 2012; Jain and Sharma, 2015a,b; Jain and Büchner, 2014a,b, 2015; Jain et al., 2017b,a). These and other EMHD studies are also relevant for electron only reconnection.

Fig. 5 shows results from the 2-D EMHD (x-z plane) simulations of magnetic reconnection in electron scale current sheets of different half-thicknesses (ϵ) (Jain and Sharma, 2015b). In these simulations, the equilibrium current density is $\mathbf{J} = -n_0 e u_{ey0} \hat{y} = (B_\infty c / (4\pi \epsilon)) \text{sech}^2(z/\epsilon) \hat{y}$ corresponding to the equilibrium anti-parallel magnetic field $\mathbf{B} = B_\infty \tanh(z/\epsilon) \hat{x}$. The density n_0 is uniform and thus the current is due to the electron flow u_{ey0} . The results are shown in the normalized units: length by electron inertial length $d_e = c/\omega_{pe} = c/(4\pi n_0 e^2/m_e)^{1/2}$, magnetic field by B_∞ and time by $\omega_{ce}^{-1} = (eB_\infty/m_e c)^{-1}$. Reconnection rate, measured by out-of-plane electric field E_y at the X-point and shown in Fig. 5a, reaches its peak value when the growth of the rms values of B_z begins to slow down, consistent with the Faraday law which gives $\partial E_y / \partial x = -1/c \partial B_z / \partial t$. The peak reconnection rate E_y^{peak} scales with ϵ as $E_y^{peak} = 0.05/\epsilon^{1.15}$ and drops from $E_y^{peak} = 0.05 v_{Ae} B_\infty / c$ to $E_y^{peak} = 0.01 v_{Ae} B_\infty / c$ as the ϵ increases from $\epsilon = d_e$ to $\epsilon = 4 d_e$. This range of reconnection rate in units based on ion Alfvén speed is $E_y^{peak} = 0.43 - 2.15 v_{Ai} B_\infty / c$ (using ion $m_i/m_e = 1836$) which is much larger than the value of the reconnection rate ($0.1 v_{Ai} B_\infty / c$) for the standard ion-coupled reconnection. Reconnection rates for the electron only reconnection have been reported in the similar range by MMS observations (Burch et al., 2020) and PIC simulations (Sharma Pyakurel et al., 2019).

Note that the EMHD simulation results in Fig. 5 are independent of the strength of the guide magnetic field because a uniform guide field does not appear in 2-D EMHD equations (Jain and Büchner, 2015). However, in 3-D, guide field can introduce current aligned instabilities in addition to the tearing instability as has been predicted by 3-D EMHD eigen value analysis (Jain and Büchner, 2015) and simulations (Jain et al., 2017a). In 3-D, current aligned electron Kelvin-Helmholtz instabilities can grow in electron scale current sheets even in the absence of guide magnetic field (Jain and Büchner, 2014a,b; Greess et al., 2021). These EMHD studies are relevant for the MMS

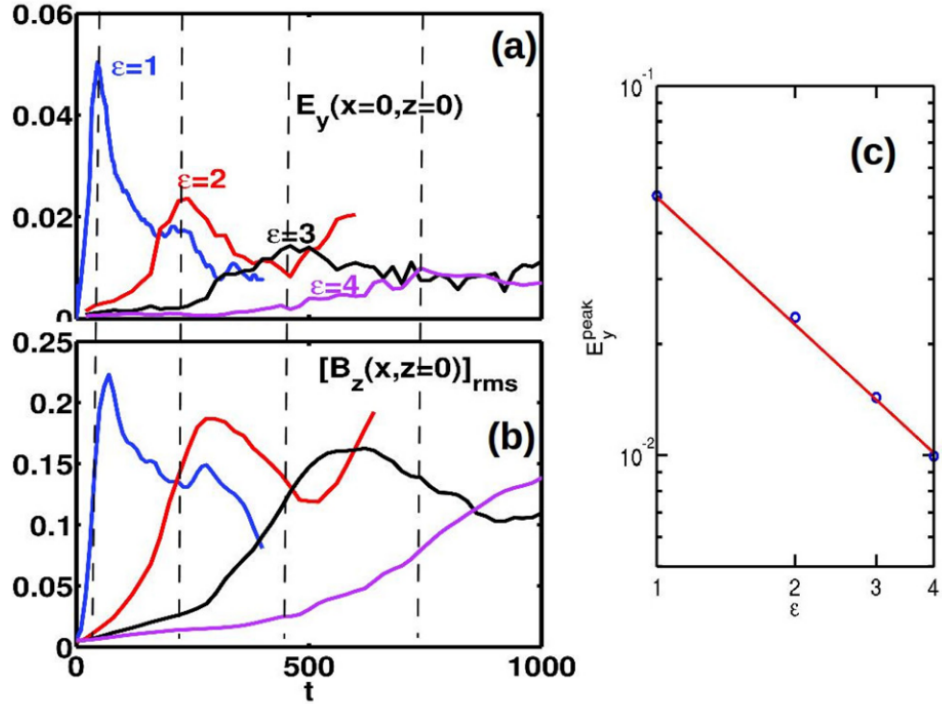


Fig. 5 Evolution of (a) out-of-plane electric field E_y at the X-point ($x = 0, z = 0$) and (b) root-mean-square value of the normal component of magnetic field B_z evaluated over the length of the reconnecting current sheet (between two outflow regions) on the line $z = 0$. Vertical dashed lines mark the times at which E_y attains its peak value E_y^{peak} for different values of the current sheet half-thickness ϵ . (c) Scaling of E_y^{peak} with ϵ (in log-scale) from simulations (blue circles) and a fit $E_y^{peak} = 0.05/\epsilon^{1.15}$ (red line). Adapted from [Jain and Sharma \(2015b\)](#).

observations of the electron shear flow generated electron Kelvin-Helmholtz vortices within the diffusion region of collisionless magnetic reconnection ([Zhong et al., 2022, 2018](#); [Hwang et al., 2019](#)).

4.4.5 Outlook

Hybrid-kinetic simulations with electron inertia provide a computationally less expensive (in comparison to fully kinetic simulations) tool to study magnetic reconnection with guide field in which bulk electron inertia is the dominant mechanism breaking the frozen-in condition of magnetic field. There have been some hybrid-kinetic simulations studies with electron inertia of guide field magnetic reconnection ([Kuznetsova et al., 1998](#); [Kuznetsova, 2000](#); [Shay et al., 1998](#); [Califano et al., 2020](#); [Muñoz et al., 2023](#)). More studies are, however, required to address still many open questions about the guide field magnetic reconnection. The EMHD limit (stationary ions) of the hybrid-kinetic model with electron inertia is particularly useful to study the nature

of reconnection in electron scale current sheets and is relevant for the recently discovered electron-only reconnection (Phan et al., 2018). At the same time, simulations of kinetic plasma turbulence from ion to electron scales using hybrid-kinetic model with electron inertia will shed light on the conditions under which electron scale current sheets form and reconnect with or without ion coupling in the turbulence.

5 Fully Kinetic Particle-in-Cell Simulations

5.1 Introduction

The particle-in-cell (PIC) method is a simulation method in which the plasma is treated as a collection of particles (electrons and ions), where each species is typically composed of up to 10^{12} particles in 3D cases. In PIC simulations, the motions of individual particles and the evolution of electric and magnetic fields are solved self-consistently. The electric and magnetic fields are defined on discrete grid points. In this subsection, we will explain an explicit PIC simulation, where all the quantities are updated based on the quantities obtained in the previous time step. Let us assume that the total particle number in a simulation is N_p (in other words, $N_p/2$ for ions, and $N_p/2$ for electrons). The equation of motion for the j -th particle's position $\mathbf{x}_j(t)$ and momentum $\mathbf{p}_j(t)$, where j represents an integer between 1 to N_p , is discretized in time, while Maxwell's equations for electromagnetic fields $\mathbf{E}(\mathbf{x}, t)$ and $\mathbf{B}(\mathbf{x}, t)$ are discretized in both space and time, using a grid spacing Δx (assuming that the grids are uniform in all the coordinates, i.e. $\Delta x = \Delta y = \Delta z$) and a time step Δt , respectively. They are given as

$$\frac{\mathbf{x}_j(t_n) - \mathbf{x}_j(t_{n-1})}{\Delta t} = \frac{\mathbf{p}_j(t_{n-1/2})}{\gamma_j(t_{n-1/2})}, \quad (68)$$

$$\frac{\mathbf{p}_j(t_{n+1/2}) - \mathbf{p}_j(t_{n-1/2})}{\Delta t} = q_j \left[\mathbf{E}(\mathbf{x}_j(t_n), t_n) + \frac{\mathbf{p}_j(t_n)}{c\gamma_j(t_n)} \times \mathbf{B}(\mathbf{x}_j(t_n), t_n) \right], \quad (69)$$

$$\frac{\mathbf{E}(\mathbf{x}, t_{n+1}) - \mathbf{E}(\mathbf{x}, t_n)}{\Delta t} = -4\pi\mathbf{J}(\mathbf{x}, t_{n+1/2}) + c\nabla_f \times \mathbf{B}(\mathbf{x}, t_{n+1/2}), \quad (70)$$

$$\frac{\mathbf{B}(\mathbf{x}, t_{n+3/2}) - \mathbf{B}(\mathbf{x}, t_{n+1/2})}{\Delta t} = -c\nabla_f \times \mathbf{E}(\mathbf{x}, t_{n+1}), \quad (71)$$

where γ_j is the Lorentz factor, q_j is a charge, c is the speed of light, and the operator $\nabla_f \times$ represents the finite difference version of the curl operation. The time is discretized to be $t_a = a\Delta t$, where a represents an integer n or a half integer $n + 1/2$. Note that $\mathbf{B}(\mathbf{x}_j(t_n), t_n)$ in the right-hand side of Eq. (69) represents the mean of $\mathbf{B}(\mathbf{x}_j(t_n), t_{n+1/2})$ and $\mathbf{B}(\mathbf{x}_j(t_n), t_{n-1/2})$. As seen in Eqs. (68) and (69), the position \mathbf{x}_j is computed at integer time, $t = t_n$, while the momentum \mathbf{p}_j is computed at half-integer time, $t = t_{n+1/2}$. This time staggering gives the second-order accuracy, i.e. the error is $O(\Delta t^2)$. In the same way, for the spatial discretization for $\mathbf{E}(\mathbf{x}, t)$ and $\mathbf{B}(\mathbf{x}, t)$, the Yee lattice (Yee, 1966) is used, in which each component of electric and magnetic fields is defined as in Fig. 6. Also, each component of the current density $\mathbf{J}(\mathbf{x}, t)$ is defined at the same position as $\mathbf{E}(\mathbf{x}, t)$. These fields, which are spatially and temporarily staggered, are advanced using Eqs. (70) and (71), keeping the second-order accuracy in space and time. Eq. (71) guarantees that the Gauss's law for the

magnetic field, $\nabla_f \cdot \mathbf{B} = 0$, where $\nabla_f \cdot$ represents the finite difference version of the divergence, is satisfied when it is satisfied at $t = 0$.

To solve Eq. (69), the Boris method (Boris, 1970) is commonly used. This method has three steps: (1) The momentum is updated from $\mathbf{p}_j(t_{n-1/2})$ to $\mathbf{p}_j(t_n)^*$, using only the electric field $\mathbf{E}(\mathbf{x}_j(t_n), t_n)$ for a half time step $\Delta t/2$. (2) The momentum vector $\mathbf{p}_j(t_n)^*$ is rotated to be $\mathbf{p}_j(t_n)^{**}$ using only the magnetic field $\mathbf{B}(\mathbf{x}_j(t_n), t_n)$ for a full time step Δt . (3) The rotated momentum is further updated from $\mathbf{p}_j(t_n)^{**}$ to $\mathbf{p}_j(t_{n+1/2})$, using the electric field $\mathbf{E}(\mathbf{x}_j(t_n), t_n)$ for another half time step $\Delta t/2$.

In the PIC method, each particle is not a point particle, but it has a finite size to reduce noise. The shape of a particle depends on simulation codes, but the most commonly used shape function is a triangular function, $S_x(x - x_j) = (1 - |x - x_j|/\Delta x)$ when $|x - x_j|/\Delta x < 1$ and zero otherwise, where only the x component is considered. In 2D and 3D simulations, the y and z components of the shape functions are multiplied, as $S(\mathbf{x} - \mathbf{x}_j) = S_x(x - x_j)S_y(y - y_j)$ for 2D and $S(\mathbf{x} - \mathbf{x}_j) = S_x(x - x_j)S_y(y - y_j)S_z(z - z_j)$ for 3D. Using these shape functions, the charge density $\rho(\mathbf{x}, t)$ is computed as $\rho(\mathbf{x}, t) = \sum_j q_j S(\mathbf{x} - \mathbf{x}_j)$. This way of charge assignment is reversed to compute the electric field exerted from each grid point to a particle's position. To avoid the self-force (the force due to the electric field generated by the particle itself), we must first average the electric fields defined on half-integer grids to obtain the mean electric field on each integer grid, before assigning the electric fields to the particle. The magnetic fields are assigned from grids to the particle position in the same way.

The current density can also be calculated using $\mathbf{J}(\mathbf{x}, t) = \sum_j q_j \mathbf{v}_j S(\mathbf{x} - \mathbf{x}_j)$, where \mathbf{v}_j is the velocity, but the calculated $\mathbf{J}(\mathbf{x}, t)$ does not satisfy the continuum equation, $[\rho(\mathbf{x}, t_{n+1}) - \rho(\mathbf{x}, t_n)]/\Delta t + \nabla_f \cdot \mathbf{J}(\mathbf{x}, t_{n+1/2}) = 0$; therefore, the electric field calculated using Eq. (70) with this $\mathbf{J}(\mathbf{x}, t)$ does not satisfy the Gauss's law, $\nabla_f \cdot \mathbf{E}(\mathbf{x}, t_{n+1}) = 4\pi\rho(\mathbf{x}, t_{n+1})$. This means that we must either correct the electric field $\mathbf{E}(\mathbf{x}, t_{n+1})$ to satisfy the Gauss's law, or use another method to compute $\mathbf{J}(\mathbf{x}, t)$. A technique for the former is explained in Birdsall and Langdon (1991). For the latter, for example, Villasenor and Bunemann (1992) developed a rigorous charge conservation method for 2D and 3D PIC simulations, which guarantees that both the Gauss' law and the continuum equation are satisfied at the same time, when they are satisfied at $t = 0$.

The time step Δt must satisfy the Courant–Friedrichs–Lewy condition, $\Delta t < \Delta x/(cN_d^{1/2})$, where N_d represents the dimensionality ($N_d = 1, 2$, or 3). Also, the grid spacing Δx should be close to the Debye length λ_D , otherwise strong numerical heating occurs. Even when those conditions are satisfied, if particles are relativistic, a numerical Cherenkov instability can occur and the noise field becomes extremely large. When this occurs, a noise reduction method such as by Godfrey (1980) can be used.

Various boundary conditions can be implemented including periodic, conducting wall, and open boundaries (Daughton and J.Scudder, 2006; Ohtani and Horiuchi, 2009).

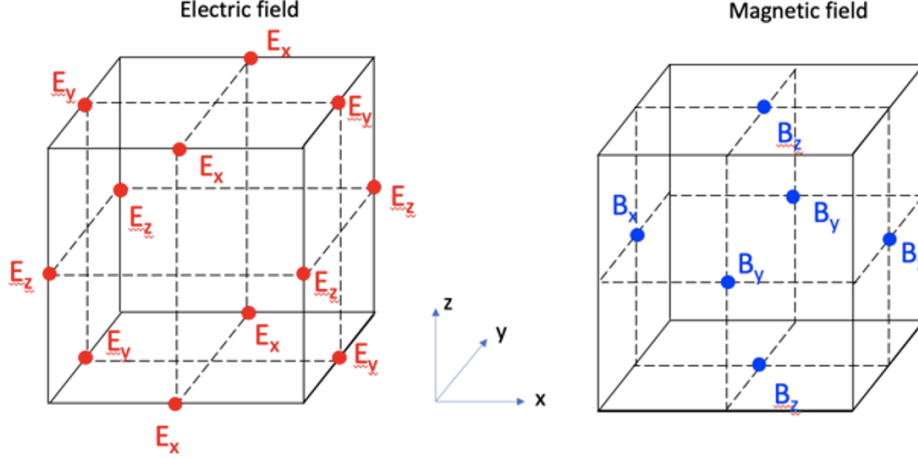


Fig. 6 Yee lattice and electric and magnetic fields in a cell in a 3D case, where the length of each side is Δx . Electric fields \mathbf{E} are defined at the midpoint of each side of the cube, while magnetic fields \mathbf{B} are defined at the center of each face of the cube. In a 2D case, all the quantities are defined in the x - y plane, projecting each position onto the cell in the x - y plane.

5.2 Magnetotail reconnection

In the Earth's magnetotail, the strength of magnetic field across the current sheet is symmetric, and the guide field (B_y field in the GSM coordinates) is small in many reconnection events. Many authors have been studying symmetric magnetic reconnection with zero guide-field, using the Earth's magnetotail parameters (Hoshino, 1987; Pritchett et al., 1991; Horiuchi and Sato, 1994; Dreher et al., 1996; Zhu and Winglee, 1996; Hesse et al., 1996). In these simulations, the initial plasma is set up based on a Harris equilibrium (Harris, 1962a): the magnetic field $B_x = B_0 \tanh(z/w)$, and the density $n = n_0 \operatorname{sech}^2(z/w) + n_b$, where B_0 is the asymptotic magnetic field, w is the sheet thickness, n_0 is the peak density of the current sheet, and n_b is the background density. Also the conditions for the Harris equilibrium, $B_0^2/(8\pi) = n_0(T_i + T_e)$ and $|V_{di} - V_{de}| = [2c/(weB_0)](T_i + T_e)$, and $V_{di}/V_{de} = -T_i/T_e$, are satisfied, where T_i and T_e are the ion and electron temperatures, respectively, e is the elementary charge, and V_{di} and V_{de} are the y -directional drift velocity in the current sheet component of ions and electrons, respectively.

The following describes an example of a 2D PIC simulation of magnetotail reconnection, Hesse et al. (2018a). The system size is $L_x \times L_z = 102.4d_i \times 51.2d_i$, where d_i is the ion skin depth, c/ω_{pi} with ω_{pi} being the ion plasma frequency based on n_0 ($\omega_{pi} = (4\pi n_0 e^2/m_i)^{1/2}$), and 3200×3200 grids are used. The mass ratio is $m_i/m_e = 100$, the sheet thickness is $w = 0.5d_i$, the temperature ratio is $T_i/T_e = 5$, the density ratio $n_b/n_0 = 0.2$, and the ratio of the plasma frequency (based on n_0) to the electron cyclotron frequency (based on B_0) is $\omega_{pe}/\Omega_e = (4\pi n_0 e^2/m_e)^{1/2}/[eB_0/(m_e c)] = 2.0$, which gives the ratio of the light speed to the Alfvén speed (based on B_0 and n_0 , $v_{A0} = B_0/(4\pi m_i n_0)^{1/2}$) to be $c/v_{A0} = 20.0$. The x boundaries are periodic, and the

z boundaries are conducting walls. To initiate magnetic reconnection, a perturbation is added to the magnetic field as $\delta B_x = (a_0\pi/L_z)\cos(2\pi x/L_x)\sin(\pi z/L_z)$ and $\delta B_z = -(a_02\pi/L_z)\sin(2\pi x/L_x)\cos(\pi z/L_z)$, which gives a reconnection X-line at the origin $x = 0$ and $z = 0$. The total number of particles used in the simulation is 7×10^{10} .

After the simulation starts, the reconnection electric field E_y is generated in the diffusion region near the X line, where both the ion and electron motions are decoupled from the magnetic field line motion, which allows a pair of magnetic field lines across the current sheet, one is in the positive z region ($B_x > 0$) and the other is in the negative z region ($B_x < 0$), are reconnected and energy conversion occurs from the magnetic energy to the kinetic and thermal energies of ions and electrons. The reconnection rate is measured as $E_y/(B_0v_{A0}/c)$, and in this simulation it is around 0.2 (Hesse et al., 2018b). Both ion and electron outflows are produced from the X line toward the positive and negative x directions. Fig. 7(a) shows the electron fluid velocity V_{ex} , where the bipolar positive and negative V_{ex} peaks appear along the $z = 0$ in $40 < x/d_i < 60$, and each peak value reaches near the electron Alfvén speed, $v_{Ae} = B_0/(4\pi m_e n_0)^{1/2} = (m_i/m_e)^{1/2}v_{A0}$. Outside the region of $40 < x/d_i < 60$, there are strong inflows, which also reach near v_{Ae} , toward the X line along the separatrices. Because of these strong counter streaming electron flows (outflows and inflows), an electrostatic instability occurs that produces waves propagating along the separatrices toward the X line, and electrons are heated due to wave-particle interactions. Fig. 7(b) and (c) show the electron temperature in the entire box and a zoom-in view that includes a separatrix. Electrons are heated inside the separatrices (panel (b)), and the zoom-in view (panel (c)) shows that there are two solitary structures due to the nonlinear evolution of the wave (at $x = 64d_i$ and $66d_i$ along the separatrix) where electron temperature significantly enhances.

The locations of the instability, along the separatrices, correspond to the boundary of the high electron temperature, which suggests the importance of the electrostatic instability to heat electrons. To understand the effect of the instability on the heating, Hesse et al. (2018a) analyzed the pressure equation:

$$\frac{\partial p}{\partial t} = -\nabla \cdot (\mathbf{V}p) - \frac{2}{3} \sum_l P_{ll} \frac{\partial}{\partial x_l} V_l - \frac{1}{3} \sum_{l,j} \frac{\partial}{\partial x_i} Q_{lij} - \frac{2}{3} \sum_{l,i(l \neq i)} P_{li} \frac{\partial}{\partial x_i} V_l, \quad (72)$$

where all the quantities are for electrons (the subscript e is omitted): p is the scalar pressure, \mathbf{V} is the fluid velocity, and P_{ij} and Q_{ijl} are the pressure tensor and the heat tensor, respectively. The first two terms represent the compression effect, the third term is due to the heat flux, and the fourth term represents the quasi-viscous effect due to the off-diagonal components of the pressure tensor. Fig. 7(d) shows the contribution of each term in Eq.(72), integrated over the region of $A > A_0$, where A is the y component of the magnetic flux function (i.e., $B_x = \partial A/\partial z$ and $B_z = -\partial A/\partial x$). Note that $A = 0$ at the outermost z boundaries, and A is decreasing as we approach $z = 0$. Fig. 7(d) indicates that the quasi-viscous term (the fourth term) is the dominant term to provide the pressure increase, leading heating in the reconnection region.

5.3 Magnetopause reconnection

PIC simulations of magnetopause reconnection can include certain challenges due to asymmetries in the densities, temperatures and magnetic field strengths of the abutting plasmas (Sonnerup et al., 1986; Cassak and Shay, 2007). Specifically, magnetospheric plasma is usually relatively sparse, hot, and threaded by a strong magnetic field, while magnetosheath plasma (which arises from shocked solar wind) is denser, cooler, and includes a somewhat weaker field.

From a simulation perspective, the density asymmetry – which can exceed an order of magnitude – can be particularly problematic. PIC simulations are inherently noisy. The random fluctuations tend to follow Poissonian statistics with an amplitude scaling as $1/\sqrt{N_{pc}}$, with N_{pc} the number of (macro) particles per computational cell. If variations in the number of macroparticles directly translate to variations in density, a 16 : 1 ratio between the magnetosheath and magnetospheric plasma densities will produce noise levels an unacceptable four times larger in the latter than the former. One obvious approach – throwing more particles at the problem – can quickly become computationally burdensome. An alternative is the use of particle weighting, in which each particle is assigned a weight w (ranging, say, from 0 to 255) that determines its significance in the calculation of particle moments (e.g., charge and current density). Doing so allows for an initially uniform distribution of particles with a roughly constant noise level. More sophisticated algorithms allow for the splitting and joining of particles as the simulation progresses to account for the development of density variations and to address computational load imbalances.

A 2D simulation of the magnetopause with `p3d`, a PIC code employing weighted particles (Zeiler et al., 2002), was presented in Swisdak et al. (2018). In its normalization, a reference magnetic field strength B_0 and density n_0 define the velocity unit $v_{A0} = B_0/(4\pi m_i n_0)^{1/2}$. Times are normalized to the inverse ion cyclotron frequency $\Omega_{i0}^{-1} = m_i c/(eB_0)$, lengths to the ion inertial length $d_{i0} = c/\omega_{pi0}$ (where $\omega_{pi0} = (4\pi n_0 e^2/m_i)^{1/2}$ is the ion plasma frequency), electric fields to $v_{A0} B_0/c$, and temperatures to $m_i v_{A0}^2$.

The initial conditions closely mimic those observed during the diffusion region encounter described in Burch et al. (2016). In the system considered here, B_0 and n_0 correspond to their asymptotic magnetosheath values: $B_0 = 23$ nT and $n_0 = 11.3$ cm⁻³. The simulation uses an *LMN* coordinate system in which the reconnecting field parallels the *L* axis (roughly north-south), the *M* axis runs roughly east-west, with downward positive, and the *N* axis points radially away from Earth and completes the right-handed triad. The computational domain has dimensions $(L_L, L_N) = (40.96, 20.48)$ with periodic boundary conditions used in all directions. While particles can move in the *M* direction, variations in physical quantities are not permitted: $\partial/\partial M = 0$.

The reconnecting component of the field B_L and the ion and electron temperatures, T_i and T_e , vary as functions of *N* with hyperbolic tangent profiles of width 1. The asymptotic values of n , B_L , T_i , and T_e in code units are 1.0, 1.0, 1.37, and 0.12 in the magnetosheath and 0.06, 1.70, 7.73, and 1.28 in the magnetosphere. Pressure balance determines the initial density profile. The guide field $B_M = 0.099$ is much smaller than B_L (i.e., the reconnection is nearly anti-parallel) and initially uniform. While not

an exact kinetic equilibrium, the unperturbed configuration is in force balance and would not undergo significant evolution during the timescales of interest. Instead, a small initial perturbation is introduced to trigger reconnection onset.

The ion-to-electron mass ratio is chosen to be 100, which is sufficient to separate the electron and ion scales (the electron inertial length $d_{e0} = 0.1d_{i0}$). The normalized speed of light is $c = 15$ so that $\omega_{pe}/\Omega_e = 1.5$ in the asymptotic magnetosheath and ≈ 0.2 in the asymptotic magnetosphere; the observed ratios are larger, ≈ 46 and 7, and as a consequence the simulation's Debye length is larger than in the real system. However, since the development of reconnection does not appreciably depend on physical effects at the Debye scale the expected impact is minimal. The spatial grid has resolution $\Delta = 0.01$ in normalized units while the Debye length in the simulation's magnetosheath, ≈ 0.03 , is the smallest physical scale. To ameliorate numerical noise, particularly in the low-density magnetosphere, each grid cell initially contains 3000 weighted macroparticles.

Figure 8 shows results. The asymmetry in the field strength is apparent in the distribution of the field lines, with the separatrices extending much farther (in the N direction) into the plasma of the magnetosheath (top) than the magnetosphere (bottom). The Hall electric and magnetic fields (panels c and e) differ significantly from the case of symmetric reconnection, with the former concentrated almost exclusively on the magnetospheric side while the latter is almost completely dipolar rather than quadrupolar. Due to the use of weighted particles, the numerical noise is similar on both sides.

5.4 The 3D nature of magnetic reconnection

The third dimension out of the 2D reconnection plane introduces numerous additional plasma instabilities (e.g. [Daughton et al. \(2011\)](#)). In this subsection, we will focus more on the inherent 3D nature of reconnection X-line itself, including the effect of limited X-line extent, its tendency of spreading, and its orientation preference.

To sustain a current sheet, electrons and ions drift in the opposite directions. This fact introduces the asymmetry along the X-line (current) direction. To reveal this effect, [Liu et al. \(2019\)](#) and [Huang et al. \(2020\)](#) studied magnetic reconnection with the X-line being spatially confined in the current direction. They included thick current layers to prevent reconnection from spreading out of the two ends of a thin current sheet that has a thickness on an ion inertial (d_i) scale. The x component of the magnetic field is given as $B_x = B_0 \tanh[z/L(y)]$, where the half-thickness $L(y) = L_{min} + (L_{max} - L_{min})[1 - f(y)]$ and $f(y) = [\tanh((y + w_0)/S) - \tanh((y - w_0)/S)]/[2\tanh(w_0/S)]$, $L_{min} = 0.5d_i$, $L_{max} = 4d_i$, and $S = 5d_i$. The parameter w_0 , which controls the y -extent of the thin current region (L_{y-thin}), is varied from $w_0 = 2d_i$ to $20d_i$, corresponding to the y -extent of the thin current region from $L_{y-thin} \sim 4d_i$ ($w_0 = 2d_i$) to $L_{y-thin} \sim 30d_i$ ($w_0 = 20d_i$). The density is $n = n_0 \text{sech}^2[z/L(y)] + n_b$, and $n_b = 0.3n_0$. The system size is $L_x \times L_y \times L_z = 32d_i \times 64d_i \times 16d_i$. The periodic boundary condition is used for x and y , and the conducting walls are placed in the z boundaries. Over 2.6×10^{10} particles for each species are used.

The resulting reconnection is shown in Fig. 9, which is for $L_{y-thin} \sim 30d_i$. [Liu et al. \(2019\)](#) found that the reconnection rate and the outflow speed drop significantly

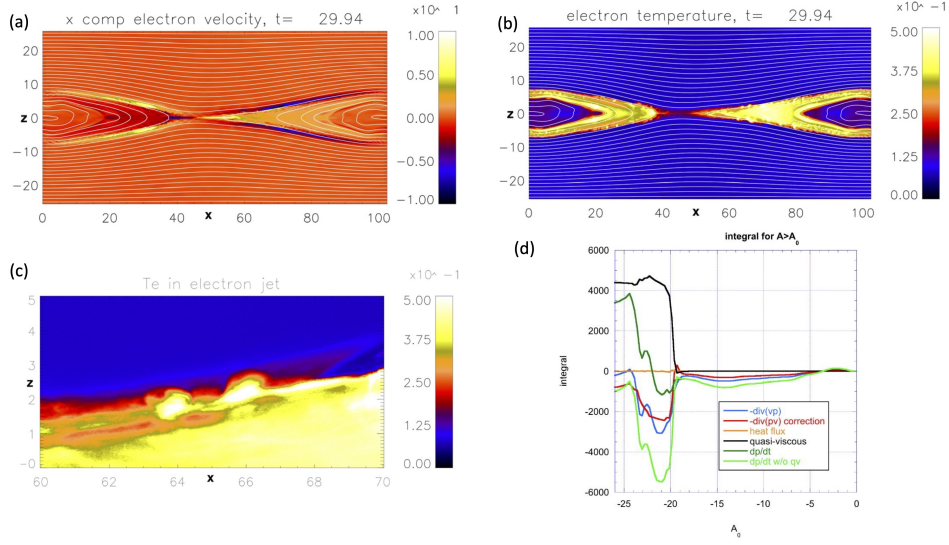


Fig. 7 2D PIC simulation result for magnetotail reconnection. (a) Electron fluid velocity V_{ex} , (b) electron temperature T_e , (c) zoom-in view of T_e , and (d) the heating term in Eq.(72). Adapted from Hesse et al. (2018a, 2019).

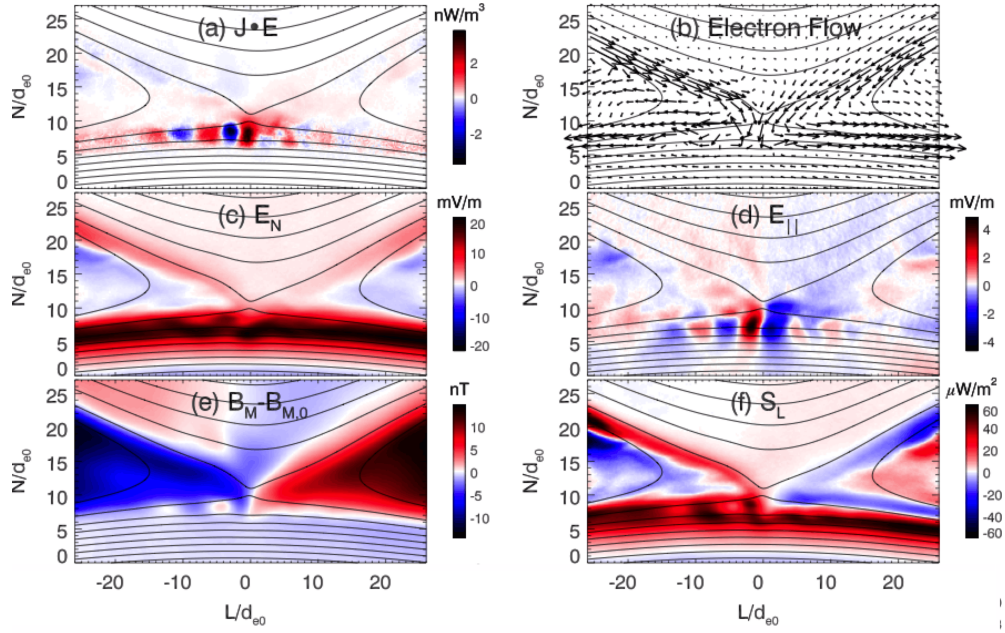


Fig. 8 Simulation results overlaid with magnetic field lines. (a) The $\mathbf{J} \cdot \mathbf{E}$ term from Poynting's theorem; (b) In-plane electron flow field; (c) E_N , the normal component of the electric field; (d) $E_{||}$, the component of the electric field parallel to the magnetic field; (e) $B_M - B_{M,0}$, the change in the out-of-plane component of the magnetic field from its (spatially constant) initial value; (f) S_L , the horizontal component of the Poynting flux. Adapted from Swisdak et al. (2018).

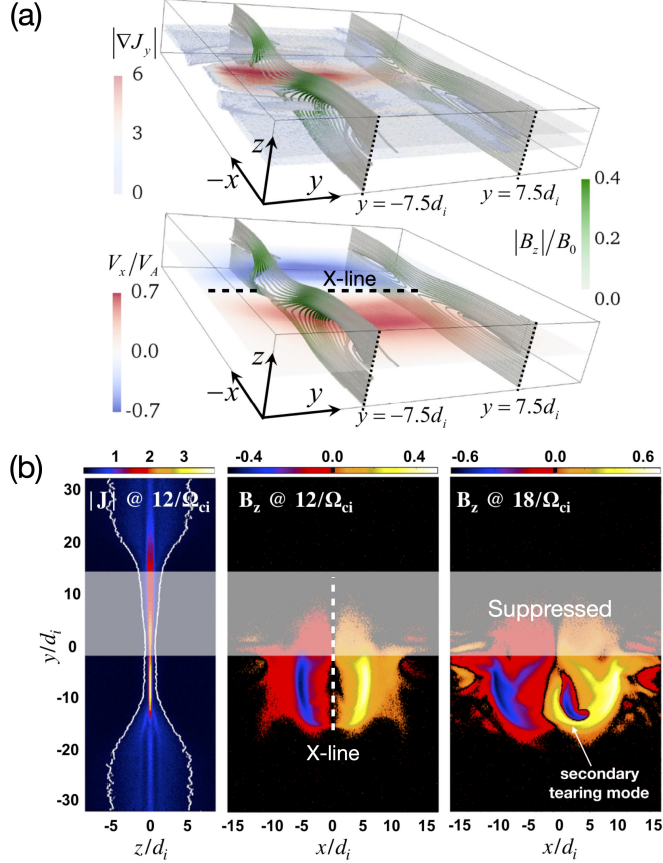


Fig. 9 3D PIC simulation results. (a) 3D view of reconnection with a limited X-line extent, where the thin current sheet region extends $30d_i$ in y (Huang et al., 2020). The mass ratio in the simulation is 25. (b) The current density on the $x = 0$ plane (left) and magnetic field B_z on the $z = 0$ plane (middle and right) (Liu et al., 2019). The mass ratio is 75. The gray shaded area represents the “suppressed reconnecting region”. Adapted from Huang et al. (2020) and Liu et al. (2019).

when the extent of the thin current sheet, L_{y-thin} , is less than $\mathcal{O}(10d_i)$. When the thin current sheet extent is long enough, it consists of two distinct regions: a suppressed reconnecting region (on the ion-drifting side) exists adjacent to the active region where reconnection proceeds normally as in a 2D case with a typical fast rate value ≈ 0.1 . The extent of this suppression region is $\mathcal{O}(10d_i)$, and it suppresses reconnection when L_{y-thin} is comparable or shorter. The time scale of current sheet thinning toward fast reconnection can be translated into the spatial scale of this suppression region, because the electron drifts inside the ion diffusion region transport the reconnected magnetic flux (that is critical in driving outflows and furthers the current sheet thinning) away from this region. This is a consequence of the Hall effect in 3D.

Huang et al. (2020) incorporated the length scale of this suppression region $\mathcal{O}(10d_i)$ to quantitatively model the reduction of the reconnection rate and the maximum outflow speed observed in the short X-line limit. The average reconnection rate drops

because of the limited active region (where the current sheet thins down to the electron inertial scale) within the X-line. The outflow speed reduction correlates with the decrease of the $J \times B$ force, which can be modeled by the phase shift between the J and B profiles, also as a consequence of the flux transport out of the reconnection plane.

While the existence of this suppression region may explain the shortest possible azimuthal extent of dipolarizing flux bundles at Earth (Liu et al., 2015), it may also explain the dawn-dusk asymmetry observed at the magnetotail of Mercury (Sun et al., 2016, 2022), which has a global dawn-dusk extent much shorter than that of Earth.

5.5 Particle acceleration

There have been quite remarkable advances in using PIC simulations to understand particle acceleration processes in magnetic reconnection, discussed in Oka et al. (2023), Drake et al., and Guo et al. (2023) of this issue. The simulation provided energetic particle flux, spectra and even detailed distributions that can be compared with in situ observations. We introduce several key diagnostics recently used for gaining insight in particle energization.

First, it has been a common practice to output particle trajectories to study the acceleration process (e.g., Hoshino et al., 2001; Drake et al., 2006; Fu et al., 2006; Oka et al., 2010; Guo et al., 2015). These have led to the identification of different acceleration mechanisms, as discussed in Oka et al. (2023) and Guo et al. (2023) of this issue. Fig. 10 shows a representative particle trajectory adapted from Oka et al. (2010). This particle is first accelerated by an X line (a), then further energized due to electric field during anti-reconnection between two merging island (c). The acceleration persists after the particle is ejected out of the X-line region. In addition, one can output the electric and magnetic fields and other quantities associated with particles, to complement the understanding of acceleration mechanisms.

The limitation of just showing several particle trajectories, even with the best effort, is that the “representative” examples are usually cherry-picking results and it is difficult to evaluate the relative importance of each mechanism. There has been recent effort to evaluate the acceleration processes over a large number of trajectories, (Guo et al., 2019, 2021; Kilian et al., 2020; French et al., 2022; Li et al., 2023).

Another method, developed and widely used over the last decade, is to study the collective energy gain, such as guiding center and pressure-restrained terms (discussed in Oka et al. (2023), this issue) using ensemble averaged moments (Dahlin et al., 2014, 2015; Li et al., 2015, 2017, 2018, 2019; Du et al., 2018). For example, the acceleration due to the curvature (Fermi) and gradient (betatron) drifts can be evaluated under guiding center approximation. Fig. 11 shows an example under the guiding-center approximation, and shows the curvature drift term is the main acceleration term. Moreover, it is possible to collect the energy dependent acceleration rates by considering particles with different energy, so the energization can be studied in a energy-dependent fashion (Dahlin et al., 2017; Guo et al., 2014; Li et al., 2018, 2019). Fig. 11b shows such an example.

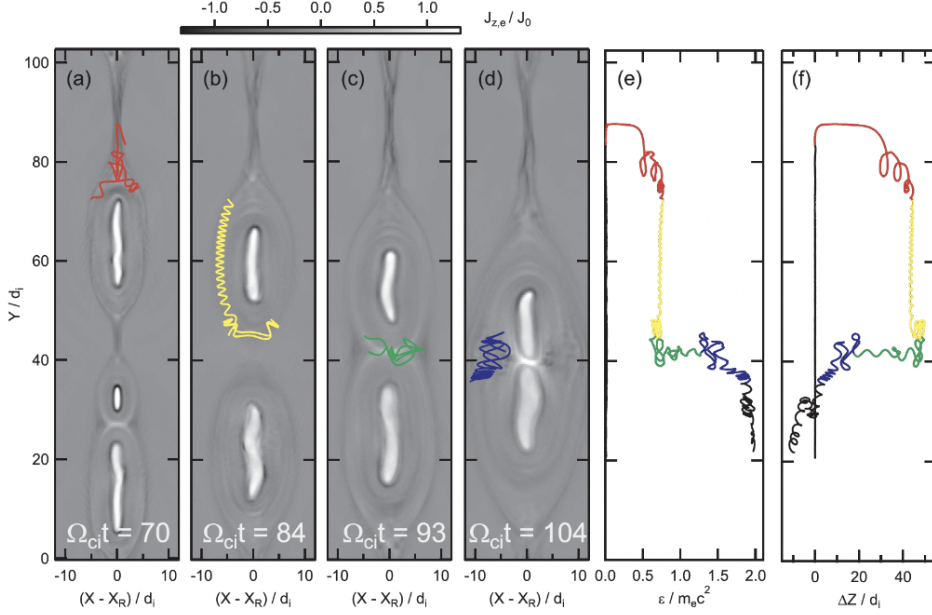


Fig. 10 An example of particle trajectory analysis. Adapted from [Oka et al. \(2010\)](#).

5.6 Simulations of magnetic reconnection in shock waves

Magnetic reconnection can occur in current sheets generated in plasma turbulence, and PIC simulations have also been applied to turbulent environments ([Wu et al., 2013](#); [Matthaeus et al., 2016](#); [Haggerty et al., 2017](#); [Shay et al., 2018](#); [Vega et al., 2020](#); [Adhikari et al., 2021](#); [Rueda et al., 2021](#)), including turbulence in Kelvin Helmholtz vortices in the magnetopause flank region ([Nakamura and Daughton, 2014](#); [Nakamura et al., 2017, 2022](#)), and the transition region in shock waves ([Matsumoto et al., 2015](#); [Bohdan et al., 2017, 2020](#); [Bessho et al., 2019, 2020, 2022, 2023](#); [Ng et al., 2022](#)).

Here, let us review 2D and 3D PIC simulation studies of magnetic reconnection in the shock turbulence. [Bessho et al. \(2019\)](#) used a 2D domain to study a quasi-parallel shock under the parameters in the Earth's bow shock. The size of the simulation domain is $L_x \times L_y = 375d_i \times 51.2d_i$, where the ion skin depth d_i has 40 grids. The plasma is uniform at $t = 0$, both ions and electrons are Maxwellian with their temperatures T_i and T_e , respectively, and the magnetic field is given as $\mathbf{B} = [B_0 \cos \theta, B_0 \sin \theta, 0]$, where θ is the shock angle with respect to the x axis. Periodic boundaries are used in the y direction, and conducting walls are placed in the x direction. To all the plasma particles, a negative drift speed, $-v_d$, in the x direction is given, and a uniform positive z component of electric field, as $E_z = v_d B_0 \sin \theta / c$, is set in the domain. At the right boundary, $x = L_x$, new particles for both ions and electrons are injected, using the same temperatures as the initially loaded particles, with the negative drift speed $-v_d$. At the left boundary, $x = 0$, all the particles are specularly reflected, and the incident particles and the reflected particles generate counter-streaming beams, which cause a beam instability. As a result, a non-linear

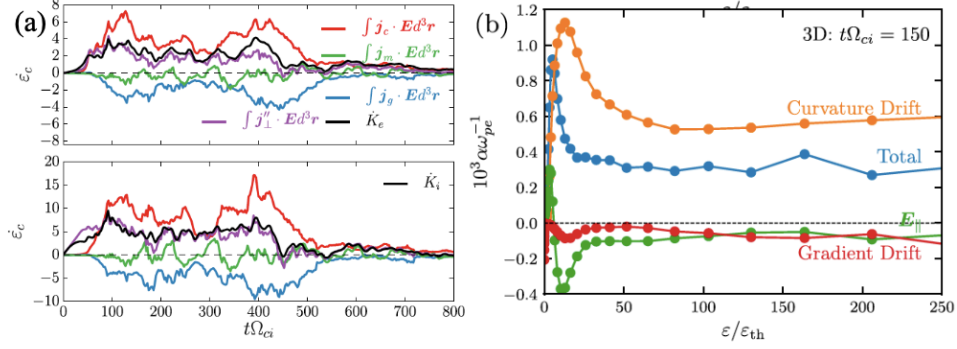


Fig. 11 (a) An example of guiding-center drift analysis. Particle energization due to different drift currents for electrons (top) and ions (bottom). j_c is due to particle curvature drift. j_g is due to particle grad- B drift. j_m is due to magnetization. $j_{\parallel} = j_c + j_g + j_m$. \dot{K}_e and \dot{K}_i are the energy change rates for electrons and ions, respectively. They are all normalized by $m_e c^2 \omega_{pe}$. (b) Similar to (a) but shows energy dependent values (Li et al., 2019) at a given time. Adapted from Li et al. (2017).

wave grows near the left boundary, and a wave steepening occurs. Eventually, a shock wave forms, propagating toward the positive x direction.

In the 2D simulation, the following parameters are used: the electron and ion beta $\beta_e = \beta_i = 1$, the ratio of the plasma frequency to the electron cyclotron frequency $\omega_{pe}/\Omega_e = 4$, the shock angle $\theta = 25^\circ$, and the mass ratio $m_i/m_e = 200$. With these parameters, the electron thermal speed becomes $v_{Te} = 14.4v_A$. The drift speed is set to be $v_d = 9v_A$. In the simulation (the downstream rest frame), the shock speed is $2.4v_A$, which corresponds to the Alfvén Mach number of the shock wave $M_A = 11.4$. In other words, the shock speed in the laboratory frame is $11.4v_A$, which is less than v_{Te} , consistent with the Earth’s bow shock.

In the simulation, the shock transition region shows a non-resonant ion-ion beam instability due to the interactions between the ions reflected by the shock and the incident ions, and many current sheets are generated, some of which show signatures of magnetic reconnection. In Fig. 12(a), the color shows the current density J_z in the 2D simulation domain, where the black curves are magnetic field lines projected onto the x - y plane, and magenta X marks represent the positions of reconnection X lines. One of the reconnecting current sheet is zoomed up in Fig. 12(b) and (c), where the electron fluid velocity V_{ex} and the ion fluid velocity V_{ix} are shown. There is one magnetic island above the current sheet, and there are bipolar electron jets generated from the X line. In contrast, the ion velocity plot does not show ion jet structures, and the ions are passing through the reconnection region with a negative V_{ix} . Therefore, this region is a site of electron-only reconnection, where only electrons are participating in reconnection, while ions cannot respond to the strong gradient of magnetic fields in the thin current sheet, whose thickness is less than the ion skin depth d_i . Electron-only reconnection has been observed in the Earth’s magnetosheath (Phan et al., 2018; Gingell et al., 2021; Stawarz et al., 2022) and the transition region of the Earth’s bow shock (Wang et al., 2019; Gingell et al., 2019, 2020). Note that the

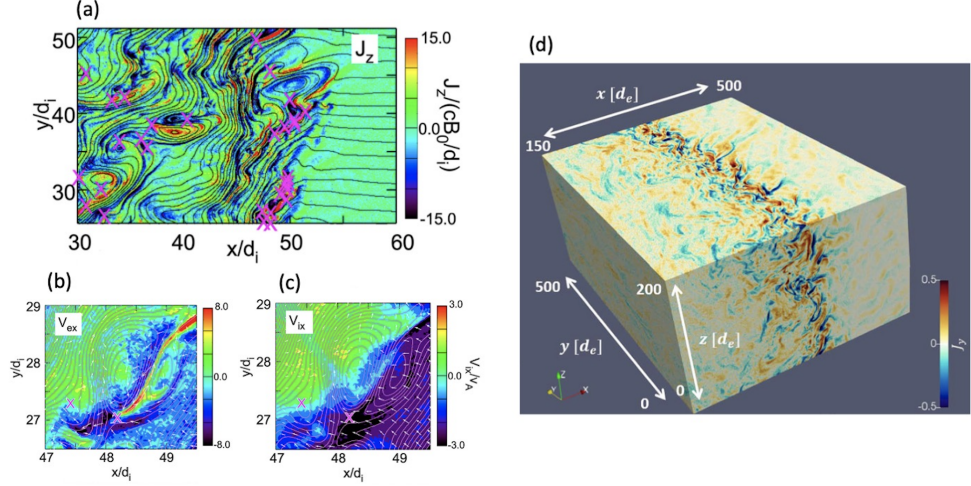


Fig. 12 PIC simulations of reconnection in shocks. (a) 2D simulation domain and the current density J_z . (b) Electron fluid velocity V_{ex} . (c) Ion fluid velocity V_{ix} . (d) 3D simulation domain and the current density J_z . Adapted from [Bessho et al. \(2019\)](#) and [Ng et al. \(2022\)](#).

shock transition region has a negative B_z magnetic field, $B_z \sim -4B_0$ (not shown), and the reconnecting magnetic field is the same order. Therefore, in the 2D simulation, reconnection in the shock transition region is guide-field reconnection.

[Ng et al. \(2022\)](#) performed a 3D PIC simulation to study reconnection in the shock transition region. The simulation parameters are: $\beta_e = \beta_i = 1.41$, $\omega_{pe}/\Omega_e = 4$, $m_i/m_e = 100$, $\theta = 30^\circ$, $v_d = 10v_A$, and the system size $L_x \times L_y \times L_z = 200d_i \times 50d_i \times 20d_i$. The z direction is set to be a periodic boundary. Fig. 12(d) shows the current density J_z . In the 3D simulation, the current direction can be not only in the z direction, but also in the y direction; therefore, the reconnection plane does not have to be in the x - y plane as in the 2D simulation, and some current sheets show reconnection with a weak guide field, even though the shock transition region has a large negative B_z .

6 Embedded PIC: MHD-AEPIC

6.1 Overview

Due to the large separation between the kinetic scales and the size of Earth's magnetosphere, it is highly computationally expensive to apply a purely kinetic code for simulating global magnetospheric dynamics. Various hybrid methods have been proposed to incorporate kinetic physics into global simulations while keeping the computational costs feasible. Traditional hybrid codes model the electron species as a fluid and simulate the ions with either macro-particles or a grid-based Vlasov solver. These hybrid models reduce the separation between the kinetic scales and the global scale by removing the electron kinetic scales from the model so that it becomes feasible to apply them to Earth's magnetosphere.

The Magnetohydrodynamic with Adaptively Embedded Particle-in-Cell (MHD-AEPIC) model represents another type of hybrid approach to incorporate kinetic effects into global models (Daldorff et al., 2014b; Shou et al., 2021; Chen et al., 2023). This type of hybrid model couples a kinetic code with a global fluid model, and only applies the kinetic code to simulate part of the simulation domain, where kinetic physics is crucial while using the fluid model to simulate the rest of the domain. Compared to a purely kinetic model, this type of hybrid model reduces the computational cost by reducing the domain size for the kinetic code, and it is best suited for applications where the important kinetic physics is localized. The MHD-AEPIC model, and its precursor, the Magnetohydrodynamic with Embedded Particle-in-Cell (MHD-EPIC) model, are the first two-way coupled models that work for global applications. Since then, similar coupled models have been developed by different independent teams. For example, Makwana et al. (2017) also developed a model that couples a PIC code with an MHD code, and Rieke et al. (2015) tried to couple a Vlasov solver with a two-fluid code.

6.2 Methodology

6.2.1 Development History

The original MHD-EPIC model was developed by Daldorff et al. (2014b), in which the semi-implicit particle-in-cell code iPIC3D (Markidis et al., 2010a) is coupled with the global fluid model BATS-R-US (Powell et al., 1999) through the Space Weather Modeling Framework (SWMF) (Tóth et al., 2005). The model has been successfully applied to study magnetic reconnections in the magnetospheres of Ganymede (Tóth et al., 2016; Zhou et al., 2019, 2020), Earth (Chen et al., 2017, 2020; Wang et al., 2022b,d), Mercury (Chen et al., 2019) and Mars (Ma et al., 2018). A PIC region has to be a box in the MHD-EPIC model. To cover the kinetic regions of interest, the MHD-EPIC model supports applying multiple independent kinetic regions (Tóth et al., 2016) in the same simulation domain, and it also allows rotating a box so that the corresponding PIC region does not have to be aligned with the global grid (Chen et al., 2020). These two features expand the capabilities of the MHD-EPIC model. However, not all the kinetic regions of interest can be covered by one or a few boxes

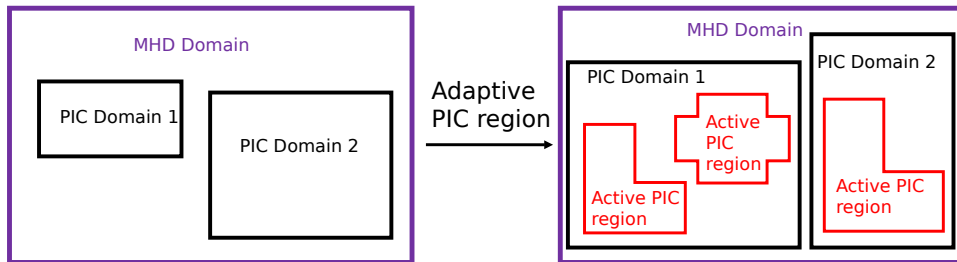


Fig. 13 A schematic shows the improvement of the MHD-AEPIC (right) model from the MHD-EPIC (left) model. Aadapted from Chen et al. (2023).

If the kinetic region moves at the global spatial scale during a simulation, the PIC box has to be very large to cover the whole region of interest, which is computationally expensive. To overcome these difficulties, the MHD-AEPIC model has been developed, which allows a dynamic PIC region of any shape (see Figure 13).

To support dynamic PIC regions, two different PIC codes, the Adaptive Mesh Particle Simulator (AMPS) (Shou et al., 2021) and the FLEKS (Chen et al., 2023), have been developed as the PIC component of the MHD-AEPIC model. Since FLEKS is more widely used for MHD-AEPIC simulations, we focus on the FLEKS code in this section.

6.2.2 Coupling Algorithm

MHD-AEPIC supports coupling with single-fluid MHD, multi-species MHD, multi-ion MHD (Glocer et al., 2009b), and five- and six-moment multi-fluid models (Huang et al., 2019). The most widely used fluid component is the single-fluid Hall MHD with a separate electron pressure equation, and we briefly describe the coupling algorithm for this case here.

In an MHD-AEPIC simulation, the PIC code covers part of the whole simulation domain. The MHD model provides the initial conditions for the PIC code at the beginning of the coupled simulation. Once the initialization is done, both the PIC and MHD models update independently for one or a few time steps until the next coupling time point is reached. During the coupling, the MHD model provides the boundary conditions for the PIC code, and the PIC code provides the updated magnetic field and plasma quantities to overwrite the overlapped MHD region. Since the MHD and PIC codes solve different sets of equations, conversion between the MHD and PIC variables is needed. When calculating PIC variables from MHD variables, we need densities, velocities, and pressures for both electron and ion species, and they are calculated as follows:

- Charge neutrality is assumed, so both the electron and ion densities can be easily obtained from total MHD density.
- From the MHD magnetic field, the current density can be calculated. Since the sum of electron and ion momentum is the total MHD momentum, and the velocity difference between electrons and ions produces the current, the electron and ion velocities can be obtained.
- Since we usually solve both ion and electron pressure equations on the MHD side, the electron and ion pressures can be obtained directly to initialize thermal PIC macro-particles.

Once the electron velocity is obtained, it is used to calculate the electric field \mathbf{E} for PIC from the generalized Ohm's law:

$$\mathbf{E} = -\frac{\mathbf{U}_e \times \mathbf{B}}{c}, \quad (73)$$

where \mathbf{B} is the MHD magnetic field and \mathbf{U}_e is the electron bulk velocity including the Hall term. We note that no matter Hall physics is included or not into the MHD

model, the equation above is applied to calculate the initial and boundary electric field for PIC.

Calculating MHD variables from PIC variables is more straightforward: we simply sum up the mass, momentum and energy of the electron and ion macro-particles to obtain the plasma variables required. We refer the readers to [Daldorff et al. \(2014b\)](#) for more details. Currently, the PIC codes used for MHD-EPIC/MHD-AEPIC coupling have to use a Cartesian mesh, but the MHD model BATSU-R-US can use non-uniform Cartesian or non-Cartesian grids. The interpolation between the PIC and MHD grids is done by a second-order linear interpolation.

6.2.3 Particle-In-Cell Algorithm

From iPIC3D for MHD-EPIC to FLEKS for MHD-AEPIC, all the PIC codes are semi-implicit ([Brackbill and Lapenta, 2008](#); [Lapenta, 2017](#); [Chen and Tóth, 2019](#)), meaning that the electric field is solved for by an implicit scheme. We choose the semi-implicit PIC algorithm because it has a relaxed stability constraint so that the Debye length does not have to be resolved and the stability constraint for the time step is based on the thermal speed instead of the speed of light. Based on our numerical experiments, we found the stability of the PIC code is extremely important for a successful MHD-EPIC/MHD-AEPIC simulation. To improve the stability, we designed the Gauss's Law satisfying Energy-Conserving Semi-Implicit Method (GL-ECSIM) ([Chen and Tóth, 2019](#)), which is based on the Energy-Conserving Semi-Implicit Method (ECSIM) by [Lapenta \(2017\)](#). GL-ECSIM shares the same energy conservation property as ECSIM, i.e., the total energy of the system can be exactly conserved with proper parameters. In practice, we found the code is more stable with parameters that slowly dissipate the total energy numerically. In addition, satisfying Gauss's law (charge conservation) is also crucial for the stability and accuracy of the PIC code. GL-ECSIM applies a novel method to satisfy Gauss's law by adjusting particle positions at the end of each cycle. The details of GL-ECSIM can be found in [Chen and Tóth \(2019\)](#).

In a long MHD-AEPIC simulation, the macro-particle number per cell may vary significantly due to the transport of particles. The uneven distribution of particle numbers can cause load imbalance and reduce computational efficiency. To alleviate this problem, we designed particle splitting and merging algorithms for FLEKS. A particle splitting (merging) algorithm is applied to split (merge) particles when the number of particles per cell is below (above) a threshold ([Chen et al., 2023](#)).

6.2.4 Kinetic Region Adaptation

The most important improvement of MHD-AEPIC over MHD-EPIC is the adaptive PIC region. Although the PIC grid is still Cartesian, its cells can be switched on or off so that the active cells can fit any shape of kinetic regions. We note that the PIC cells can be activated or deactivated dynamically during a simulation. The active PIC region can be defined either based on geometric or physical criteria. For physics-based adaptation, BATS-R-US calculates the physical criteria and sends the corresponding grid information to FLEKS to turn on or turn off cells.

6.2.5 Kinetic Scaling

In some applications, the difference between kinetic and global spatial and temporal scales makes it difficult, if not impossible, to resolve the kinetic scales in an MHD-EPIC, or even MHD-AEPIC simulation. Fortunately, the large separation of scales can be exploited, and the kinetic scales can be increased by changing the mass per charge ratio without affecting the global dynamics (Tóth et al., 2017). This technique is not needed or even applicable for Ganymede and Mercury simulations, where the kinetic and global scales are not very different. On the other hand, kinetic scaling is applicable and extremely useful for modeling Earth’s magnetosphere. We typically increase the kinetic scales by a factor of 4 to 16. See Tóth et al. (2017) for more detail.

6.3 Applications

The MHD-EPIC/MHD-AEPIC model has been applied to investigate the physical processes and consequences of both magnetopause and magnetotail reconnection. In these simulations, the PIC code is usually used to cover either the magnetopause or the magnetotail current sheet, where reconnection happens. Since the initial and boundary conditions of the PIC code are obtained from the MHD model, the physical parameters inside the PIC region, such as the plasma quantities and the shape of the current sheet, are more realistic than those in a standalone PIC simulation. On the other hand, the information from the PIC code is also fed back to the MHD model so that we can evaluate the global consequences of the kinetic magnetic reconnection.

Here we briefly describe a few applications of the MHD-EPIC/MHD-AEPIC model to study Earth’s magnetosphere. Chen et al. (2017) studied both the kinetic features of magnetopause reconnection and the evolution of flux transfer events (FTEs) show in Figure 14. Near the reconnection site, the simulation successfully produced key kinetic features of asymmetric magnetic reconnection, such as the crescent electron phase space distribution and the lower hybrid drift instability. Due to the multiple X-line reconnections inside the PIC code, FTEs are generated quasi-periodically at low latitudes, then propagate toward the cusps. We briefly describe the evolution of the FTEs here:

- During the growth of an FTE, its cross-section increase, and its length extends along the dawn-dusk direction (from $t = 100s$ to $t = 150s$ in Figure 14).
- Since its ambient plasma flow speed varies, an FTE may become tilted ($t = 240s$ in Figure 14).
- There may be multiple FTEs on the magnetopause, and a few FTEs can merge into one (from $t = 320$ to $t = 660s$ in Figure 14).
- FTEs can be dissipated at high latitudes due to the reconnection between the FTE magnetic field and the cusp field lines (Figure 5 of Chen et al. (2017)).

Chen et al. (2020) simulated the GEM dayside kinetic processes challenge event, and compared simulation results with both MMS observations and ground-based SuperDARN observations. The MHD-EPIC simulation shows there are usually multiple X-lines at the magnetopause, and the expanding speed of the X-line endpoints is comparable with SuperDARN observations.

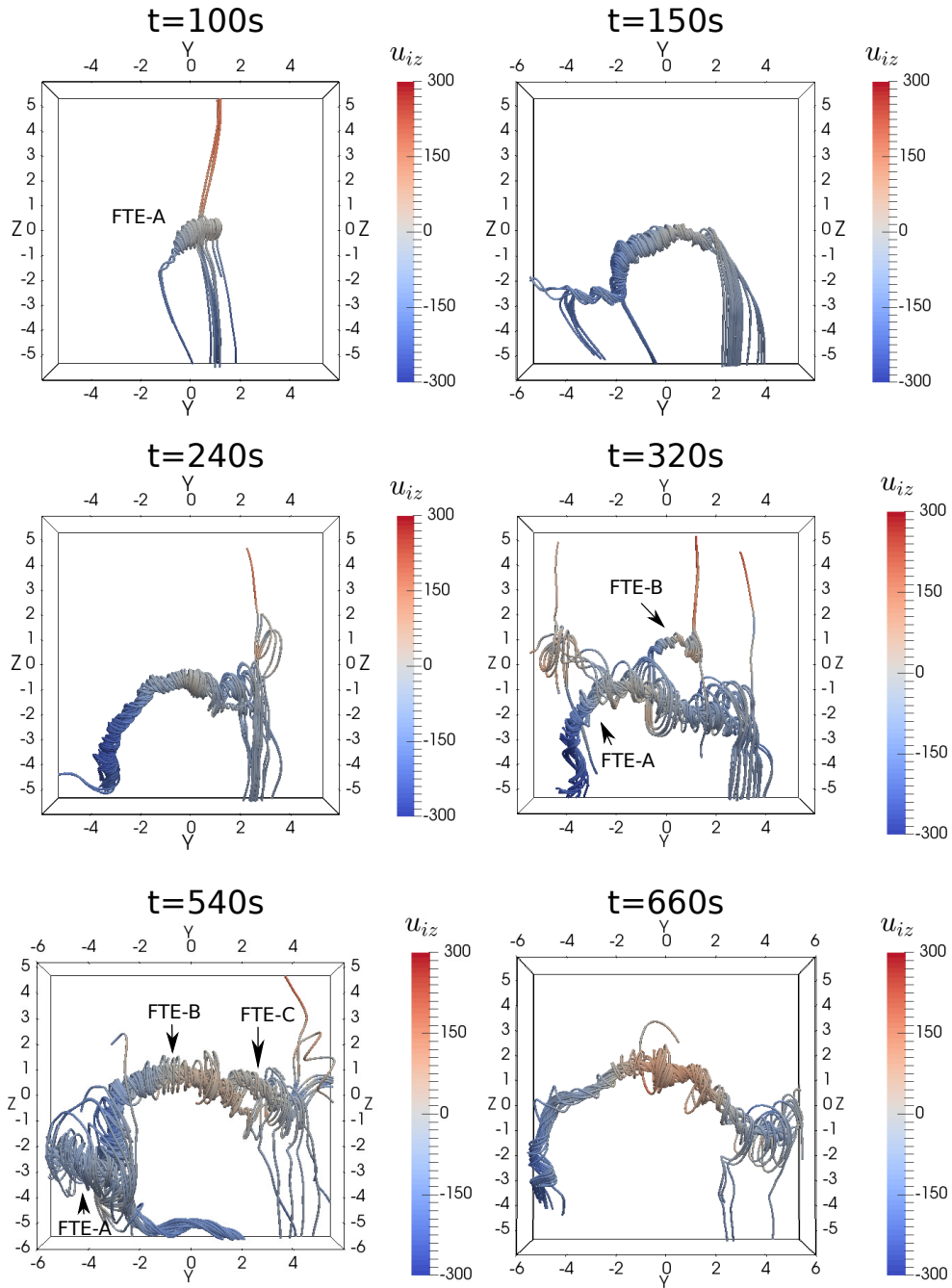


Fig. 14 Evolution of FTEs. Viewed from the Sun, a series of snapshots are shown with magnetic field lines colored by ion velocity u_{iz} [km/s]. Adapted from [Chen et al. \(2017\)](#).

The MHD-EPIC model has also been applied to study magnetotail reconnection. Wang et al. (2022d) found the MHD-EPIC simulation can produce global-scale magnetospheric sawtooth-like oscillations periodically even under steady solar wind conditions, while the ideal- and Hall-MHD simulations do not produce such variations. It suggests that kinetic reconnection physics may play an important role in driving sawtooth oscillations. Recently, the development of the MHD-AEPIC model has enabled us to simulate storm events with a dynamic PIC region that covers the highly dynamic magnetotail reconnection sites.

Our current work focuses on modeling extreme geomagnetic storm events with MHD-AEPIC. Extreme events occur infrequently, which makes it difficult to validate MHD models employing simple numerical diffusion to approximate reconnection physics. Using a higher-fidelity model, such as MHD-AEPIC, can improve the reliability of simulations of extreme events.

7 Kglobal: Particle acceleration self-consistently embedded in MHD

Solar flares convert magnetic energy into particle energy via magnetic reconnection. Observations of power-law tails in particle distribution functions imply that a large fraction of the released energy goes to energetic (i.e., non-thermal) electrons and ions (Warmuth and Mann, 2016). However, the particle spectra found in particle-in-cell (PIC) simulations of reconnection in the relevant regime typically do not form power-laws, except in the limit of extremely low upstream plasma β (Dahlin et al., 2015, 2017; Zhang et al., 2021). Why? With structures extending $\sim 10^4$ km and a Debye length of ~ 1 cm (for $n \sim 10^{10}$ cm $^{-3}$ and $T_e \sim 100$ eV), the corona spans ten orders of magnitude in physical scale. Explicit PIC models must resolve kinetic scales and hence can only simulate a tiny fraction of the macroscopic domain. The dependence of the Larmor radius on energy means nonthermal particles can quickly acquire orbits that approach the size of the simulation domain, halting further energy gains.

In contrast, MHD simulations study macroscopic domains with a fluid description that averages over small spatial and temporal scales. Following test particles in the MHD fields produces information about how particles gain energy but, without feedback coupling the particles and the fields, runaway energy gain can occur so that the system as a whole does not conserve total energy. It is possible to embed PIC models into MHD descriptions at selected locations, but such models presume that particle energy gain occurs in the vicinity of magnetic nulls, which is not consistent with the development and interaction of macroscale magnetic islands or the development of turbulence in large-scale current layers.

The *kglobal* model incorporates the physics necessary to explore particle energization from both the PIC and MHD descriptions (Drake et al., 2019; Arnold et al., 2019). The fundamental question is whether kinetic-scale boundary layers play an essential role in particle energy gain – or if they can be ordered out of the equations to facilitate simulations of macroscale systems. Kinetic boundary layers control the regions where E_{\parallel} , the component of the electric field parallel to the magnetic field,

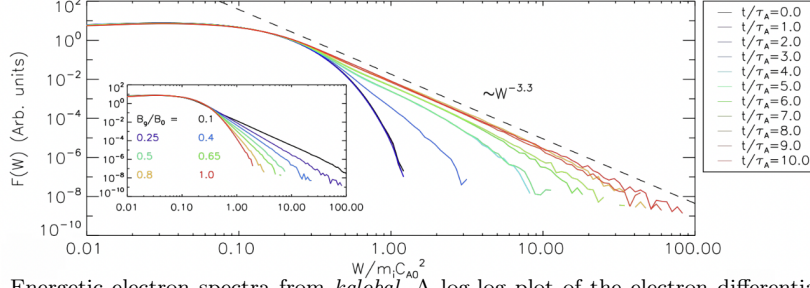


Fig. 15 Energetic electron spectra from *kglobal*. A log-log plot of the electron differential density $F(W)$ versus energy (W) at multiple times from a reconnection simulation with a guide field $B_g/B_0 = 0.25$. A power-law develops after $t/\tau_A \sim 3 - 5$. Inset: The late-time $F(W)$ for several guide fields, illustrating the dependence on the ratio of the guide-to-ambient magnetic field. Adapted from Arnold et al. (2021). However, Fermi reflection rather than E_{\parallel} is the dominant driver of energetic particles (Dahlin et al., 2016; Li et al., 2019). Particle energy gain from Fermi reflection takes place over macro-scale regions and occurs even where $E_{\parallel} = 0$. As a consequence, kinetic-scale boundary layers are not required to describe the non-thermal energization in macroscale systems.

Hence, *kglobal* combines a MHD description of the plasma dynamics with a macro-particle description. Guiding center particles populate the MHD grid, are advanced in parallel with the fluid equations, and feed back on the MHD fluid through their gyrotropic pressure tensor. They can be small in number density but can contribute a pressure comparable to the pressure of the reconnecting magnetic field. The entire system conserves total energy, which includes that of the MHD fluid, the magnetic field, and the kinetic energy of the macro-particles.

The basic version of *kglobal* includes three species: fluid ions, fluid electrons, and particle electrons (the latter of which form the nonthermal population). The fields follow the usual MHD equations

$$\frac{\partial \mathbf{B}}{\partial t} = -c \nabla \times \mathbf{E}_{\perp} \quad \mathbf{E}_{\perp} = -\frac{1}{c} \mathbf{v}_i \times \mathbf{B} \quad (74)$$

and the ion fluid satisfies the usual MHD continuity equation

$$\frac{\partial n_i}{\partial t} + \nabla \cdot n_i \mathbf{v}_i = 0 \quad (75)$$

and energy equation

$$\frac{d}{dt} \left(\frac{P_i}{n_i^{\gamma}} \right) = 0 \quad (76)$$

The ion momentum equation takes the form

$$\rho_i \frac{d\mathbf{v}_i}{dt} = \frac{1}{c} \mathbf{J} \times \mathbf{B} - \nabla P_i - \nabla_{\perp} P_{ef} - m_e n_{ef} v_{\parallel ef}^2 \boldsymbol{\kappa} + e n_i E_{\parallel} \mathbf{b} - (\nabla \cdot \mathbf{T}_{ep})_{\perp} \quad (77)$$

in which the left-hand side and first terms on the right-hand side are the same as in MHD (P_i and P_{ef} are the ion and fluid electron pressure, respectively). However the

final terms on the right-hand side include the curvature $\boldsymbol{\kappa} = \mathbf{b} \cdot \nabla \mathbf{b}$, large-scale parallel electric field E_{\parallel} , and particle electron stress tensor T_{ep} and quantify the self-consistent back-reaction of the particles on the system.

The perpendicular motion of the particle electrons is given by the conservation of the first adiabatic invariant

$$\mu_{ep} = \frac{p_{ep\perp}^2}{2B} = \text{const.} \quad (78)$$

while the parallel motion satisfies

$$\frac{d}{dt} p_{e\parallel} = p_{e\parallel} \mathbf{v}_{\mathbf{E}} \cdot \boldsymbol{\kappa} - \frac{\mu_e}{\gamma_e} \mathbf{b} \cdot \nabla B - eE_{\parallel} \quad (79)$$

This equation includes a contribution from the parallel electric field given by

$$E_{\parallel} = -\frac{1}{n_i e} \left(\mathbf{B} \cdot \nabla \left(\frac{m_e n_{ef} v_{ef\parallel}^2}{B} \right) + \mathbf{b} \cdot \nabla P_c + \mathbf{b} \cdot \nabla \cdot T_{ep} \right) \quad (80)$$

Finally, the fluid electron density enforces quasi-neutrality

$$n_{ef} = n_i - n_{ep} \quad (81)$$

the parallel flow eliminates parallel currents

$$n_{ef} v_{ef\parallel} = n_i v_{i\parallel} - n_{ep} v_{ep\parallel} \quad (82)$$

and the pressure equation takes the usual form

$$\frac{d}{dt} \left(\frac{P_{ef}}{n_{ef}^{\gamma}} \right) = 0 \quad (83)$$

A full derivation of these equations is given in [Drake et al. \(2019\)](#) and [Arnold et al. \(2019\)](#).

Simulations with these equations pass several tests. They describe the linear propagation of stable, circularly polarized Alfvén waves and the linear growth of firehose modes. The latter plays an important role in controlling the feedback of energetic particles during magnetic reconnection since magnetic tension is suppressed on the approach to firehose marginal stability. In addition, they accurately capture the dynamics of electron acoustic waves and describe the suppression of transport of hot electrons parallel to the ambient magnetic field. The inclusion of the large scale E_{\parallel} is important in describing the development of return currents that form as hot electrons escape from regions of electron acceleration in macroscale energy release events such as flares ([Egedal et al., 2012](#)).

Reconnection simulations with *kglobal* have produced power-law spectra of energetic electrons that extend nearly three decades in energy, while simultaneously generating the super-hot thermal electrons characteristic of flare observations ([Arnold](#)

et al., 2021). Fig. 15 shows the electron energy spectrum for a typical simulation. Electrons in the initial Maxwellian distribution (black curve) transform into a non-thermal spectrum in a few Alfvén crossing times (τ_A). Consistent with observations, the total energy content of the nonthermal electrons can exceed that of the hot thermal electrons even though the number density does not. The strength of the ambient out-of-plane guide field strongly impacts the energy content and power-law index of the nonthermal electrons (see inset of Figure 15): the guide field increases the radius of curvature of a reconnected field line, thereby weakening Fermi reflection (Drake et al., 2006). In contrast, the size of the global system has relatively little influence.

The governing equations of *kglobal* can be extended to include the contributions of non-thermal (particle) ions. Unlike for electrons, whose small mass can be used to simplify the equations, the ion inertia can not be neglected and must be included. Recent work has incorporated these equations into the computational model and early results reveal the simultaneous development and evolution of extended electron and proton power law distributions (Yin et al., 2024).

8 Vlasov

8.1 Overview

Eulerian Vlasov-Maxwell numerical simulations are a useful tool for investigating basic kinetic-scale plasma processes, such as turbulence and magnetic reconnection, as well as the interaction between the solar wind and planetary magnetospheres.

Thanks to the clean description of the plasma dynamics in the entire phase space at the expense of a larger computational cost, Eulerian algorithms complement well Particle-In-Cell (PIC) codes. The almost noise-free description of velocity space is generally guaranteed by the discretization of the plasma distribution function on a six-dimensional phase-space grid characterized by collocation points in both physical and velocity space. On the other hand, PIC methods suffer from the intrinsic stochastic shot noise which becomes especially relevant at small scales and in cases when the number of particles per cell is not large. However, in Eulerian methods, setting a six-dimensional grid in the entire phase space dramatically increases the computational cost. The bottleneck is generally constituted by the memory necessary to store the plasma distribution function, as shown in the following simple example.

The main difference when sampling the plasma distribution function in PIC and Eulerian approaches is depicted in Fig. 16. In PIC methods, the grid is defined only on the physical space \mathbf{x} , and the distribution function is sampled through macroparticles (blue circles), each one representative of a large number of effective plasma particles. In the Eulerian approach, the grid is defined on the entire phase space (\mathbf{x}, \mathbf{v}) and the distribution function is known on this ensemble of grid points (red circles). In both PIC and Eulerian methods, the electromagnetic fields and the moments of the distribution function (e.g., density, bulk speed, etc.) are defined on the physical-space grid \mathbf{x} .

Let's imagine a generic phenomenon occurring in a plasma composed of protons and electrons that requires a physical-space grid discretized with 512^3 points. Since

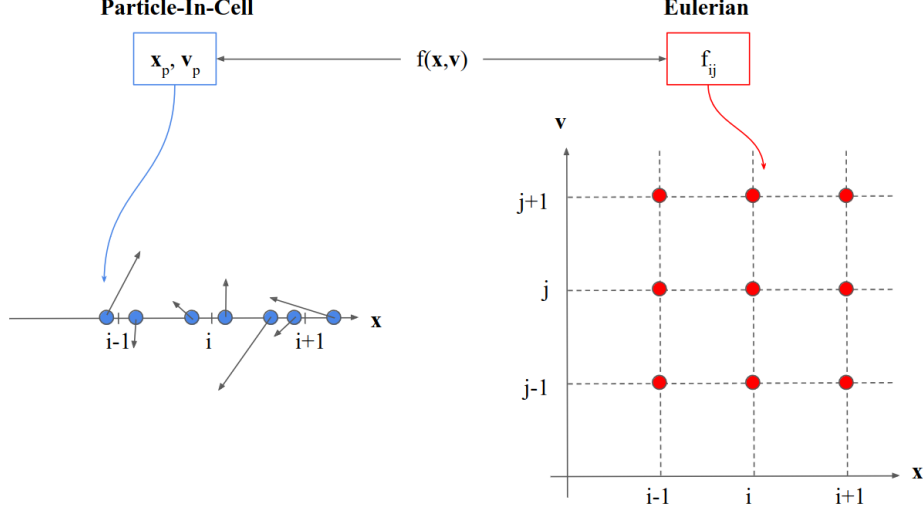


Fig. 16 Sketch of the typical sampling of the plasma distribution function $f(\mathbf{x}, \mathbf{v})$ adopted in PIC (left) and Eulerian (right) methods. Adapted from [Finelli \(2022\)](#).

the electromagnetic fields have the same memory requirements in both PIC and Eulerian methods, we neglect them here for simplicity. PIC simulations indicate that the plasma dynamics is overall well described with ~ 1000 particles per cell. The memory (assuming double-precision variables) required to store particles' positions and velocities is ~ 6 TB. Similarly, Eulerian Vlasov simulations generally adopt at least $\sim 51^3$ velocity-space points to well describe the details of the velocity plasma distribution function, thus requiring about ~ 260 TB of memory. Hence, PIC simulations can usually be performed in larger physical-space computational boxes compared to Eulerian ones. Moreover, 3D simulations are more easily achievable with PIC methods while they remain often prohibitive for Eulerian codes, or require more advanced methods such as adaptive mesh refinement or sparse velocity space techniques to become tractable.

In the following, we will introduce two models that have been intensively used by the community and, then, specialize the discussion on global and local Vlasov-Maxwell simulations of magnetic reconnection.

8.2 Models and Algorithms

Picturing a virtual journey from large to small scales, the first relevant Vlasov-Maxwell model widely adopted for performing Eulerian simulations is represented by the hybrid Vlasov-Maxwell one. The hybrid model considers protons as a kinetic species, while electrons are a background fluid. It is a low-frequency approximation of the full Vlasov-Maxwell system of equations that assumes quasi-neutrality and neglects the displacement current ([Mangeney et al., 2002](#)). Faraday's law is used to evolve the magnetic field, while the electric field is provided by the generalized Ohm's law which includes the Hall term, the electron pressure gradient term, and possibly the terms

related to electron inertia (see, e.g., [Valentini et al. \(2007\)](#) for further details about the generalized Ohm’s law).

The hybrid Vlasov-Maxwell model has been adopted for global simulations of the interaction between the solar wind and the Earth’s magnetosphere through the Vlasiator algorithm ([von Alfthan et al., 2014](#); [Palmroth et al., 2018a](#)). The Vlasiator code adopts a splitting algorithm to decompose the six-dimensional Vlasov equation into a set of two three-dimensional advection equations ([Strang, 1968](#)) in physical and velocity space, respectively. The solution of each advection equation is obtained by a semi-Lagrangian method ([Zerroukat and Allen, 2012](#)), which relieves from the strict limitations to the time step length posed by the CFL condition in velocity space acceleration in regions of strong magnetic field. Position space is discretized on a cell-adaptive Cartesian grid ([Honkonen et al., 2013](#); [Ganse et al., 2023](#)) and at each position in space the velocity-space grid is stored on a uniform, Cartesian grid. Vlasiator developed a sparse velocity-space method in which only regions of the velocity distribution function above a set phase-space density are stored and propagated ([von Alfthan et al., 2014](#)), yielding a gain of two orders of magnitude in terms of memory and computations. This technique made two-dimensional (2D position space periodic in the third dimension, 3D velocity space) magnetospheric simulations possible, as well as quasi-three dimensional simulations with a very limited extent in the third dimension ([Pfau-Kempf et al., 2020b](#)). The implementation of adaptive mesh refinement in position space, allowing to focus resolution on regions of interest while saving computations in less-resolved regions, is what made full three-dimensional, global magnetospheric simulations achievable with Vlasiator on modern, bleeding-edge supercomputers ([Grandin et al., 2023](#); [Ganse et al., 2023](#); [Palmroth et al., 2023](#)). The electric and magnetic fields are propagated using an upwind constrained transport method ([Londrillo and Del Zanna, 2004](#)) with divergence-free magnetic field reconstruction ([Balsara, 2009](#)) on a uniform Cartesian grid matching the finest refinement level of the Vlasov spatial grid, requiring a dedicated coupling scheme between the grids ([Papadakis et al., 2022](#)).

The hybrid Vlasov-Maxwell model has been also adopted for local simulations of plasma turbulence at sub-proton scales by means of the HVM algorithm ([Valentini et al., 2007](#)) (see also [Califano and Cerri \(2022\)](#) for a recent review). The HVM code reduces the six-dimensional Vlasov equation to a set of six one-dimensional advection equations. Each equation is then solved through the van Leer method ([van Leer, 1977](#)). Fields are computed through the Current-Advance Method (CAM). The grid is homogeneous in both physical and velocity space. Periodic boundary conditions are implemented in physical space, while in velocity space the proton distribution function is set to zero after a large number of thermal speeds.

Moving towards smaller scales, fully-kinetic Vlasov-Maxwell Eulerian algorithms have been recently implemented to describe electron-scale dynamics. Given the larger computational cost of Eulerian simulations with respect to PIC methods, the former are generally more recent than the latter and possibly implement different assumptions to simplify the Maxwell equations. The full Maxwell system has been retained in several codes ([Umeda et al., 2009, 2010](#); [Delzanno, 2015](#); [Ghizzo et al., 2017](#); [Juno et al., 2018](#); [Allmann-Rahn et al., 2022](#)). However, different approximations of the

Maxwell equations have been proposed to alleviate the CFL constraint which sets a very small time step when the wave phase speed approaches the speed of light. In this regard, [Wiegmann and Büchner \(2001\)](#) neglect the displacement current while allowing for charge separation, while [Tronci and Camporeale \(2015\)](#) ignore both the displacement current and the charge separation. Yet a different approach neglects only the transverse part of the displacement current responsible for ordinary mode propagating at the speed of lights ([Schmitz and Grauer, 2006a](#); [Pezzi et al., 2019](#); [Shi-oto, 2023](#)). Finally, an original approach has been developed based on the Vlasiator model, whereby a small section of interest from an ion-hybrid Vlasiator run is used to initialize an electron-hybrid setup in which the ions are kept static while the electron distribution function evolves ([Battarbee et al., 2021](#)). This so-called eVlasiator approach has successfully reproduced properties of electron distributions observed in the vicinity of reconnection diffusion regions ([Alho et al., 2022](#)).

8.3 Examples of Applications Focused on the Study of Magnetic Reconnection

8.3.1 Local simulations

In this section, we will present key results relevant to magnetic reconnection that have been obtained with the Hybrid Vlasov Maxwell code (HVM). Further treatments, based on fully-kinetic Eulerian Vlasov-Maxwell simulations, will not be covered in detail in this chapter, but the reader is referred to the works of [Schmitz and Grauer \(2006b\)](#); [Inglebert et al. \(2011\)](#); [Zenitani and Umeda \(2014\)](#); [Sarrat et al. \(2017\)](#); [Pezzi et al. \(2019\)](#), as well as Table 2 in the review by [Palmroth et al. \(2018a\)](#) which lists works using Vlasov-based methods in space and astrophysics.

The HVM code, which retains alpha particles ([Perrone et al., 2012](#); [Valentini et al., 2016](#)) and inter-particle collisions ([Pezzi et al., 2019](#)), has been used for years to investigate plasma processes occurring at ion kinetic scales. It has been massively employed to study the properties of plasma turbulence ([Valentini et al., 2010](#); [Servidio et al., 2012, 2014](#); [Servidio et al., 2015](#); [Cerri et al., 2017](#)), showing that turbulent fluctuations generate manifestly non-Maxwellian proton distribution functions ([Greco et al., 2012](#)). This emergent velocity-space complexity has been envisioned as a cascade process occurring in velocity space (e.g., [Tatsuno et al., 2009](#); [Schekochihin et al., 2016](#); [Servidio et al., 2017](#)): HVM results have allowed to characterize it in a full Vlasov system rather than in the gyrokinetic approximation ([Cerri et al., 2018](#); [Pezzi et al., 2018, 2021b](#)). Characterizing non-equilibrium plasma distribution functions is significant to understanding energy transfer and dissipation processes occurring at ion kinetic scales in nearly-collisionless plasmas such as the solar wind ([Matthaeus et al., 2020](#); [Cassak et al., 2023](#)), as also reported in different studies based on the HVM code ([Sorriso-Valvo et al., 2018](#); [Pezzi et al., 2019](#); [Pezzi et al., 2021a](#); [Fadanelli et al., 2021](#)). In the perspective of the [Holloway and Dorning \(1991\)](#) work showing that non-Maxwellian plasmas can support the propagation of undamped plasma waves, the HVM code has been adopted to study the onset of a novel type of electrostatic fluctuations triggered by trapped ions ([Valentini et al., 2011a,b, 2014](#)).

One of the first studies employing the HVM code for investigating magnetic reconnection reported the onset of a fast reconnection process obtained as a result of magnetic islands developed by the electromagnetic current filamentation (Califano et al., 2001). In the following years, despite the large number of studies adopting the HVM code, the vast majority of the research work mostly focused on the investigation of fully developed plasma turbulence. More recently, Finelli et al. (2021) investigated the magnetic reconnection in a similar manner as PIC-based studies discussed in Section 5, that is, modeling an isolated Harris-like current sheet (Harris, 1962b) in equilibrium or pressure balance. Such a current sheet, usually doubled in the physical-space domain to accommodate for periodic boundary conditions, quickly starts reconnecting thanks to an initial perturbation of proton density and/or current (thus magnetic field).

In particular, Finelli et al. (2021) compared results from three different models (i) the HVM model with (isotropic) isothermal electrons including finite electron-inertia, (ii) a modified HVM model, called hybrid-Vlasov-Landau-fluid (HVLF); (iii) a fully-kinetic PIC code (iPIC3D Markidis et al. (2010b)). The HVLF model is equipped to include anisotropies of the gyrotropic electron pressure with a Landau-fluid (LF) closure for the transport of the gyrotropic electron thermal energy along magnetic field lines (Sulem and Passot, 2015). Using these three models, Finelli et al. (2021) performed 2D-3V magnetic reconnection simulations with moderate guide field ($B_g = 0.25 B_0$, where B_0 is the asymptotic magnetic field) and with reduced mass ratio $m_p/m_e = 100$. The initial setup consists of a double Harris current sheet (Harris, 1962b) perturbed by long wavelength magnetic field fluctuations with random phase (with $1 < |\mathbf{k}|d_p < 9$, where \mathbf{k} is the wave vector of the fluctuations and d_p is the proton inertial length). The size of the simulations domains is $L_x \times L_y = 24\pi d_p \times 12\pi d_p$ discretized with $N_x \times N_y = 1024 \times 512$ grid points. In the HVM and HVLF simulations, the velocity space domain in each direction (x , y and z) is $[-6.4, +6.4] v_{th,p}$, where $v_{th,p}$ is the proton thermal speed, and it is discretized by 51^3 grid points. Figure 17 shows results comparing the three models.

While the reconnection linear phase evolution, as well as the overall reconnection signatures and patterns, are quite similar for all three models, Finelli et al. (2021) report that the region of intense current at the centre of the current sheet is more elongated in the case of the HVLF and PIC simulations than in the HVM run. Also, the normalized reconnection rate $R/B_0 v_A$ computed in the quasi-steady state is higher for the HVM ($R/B_0 v_A \sim 0.06$, where B_0 is the upstream magnetic field and v_A is the Alfvén speed) than for the HVLF and PIC simulations ($R/B_0 v_A \sim 0.04$). Despite these differences, the results of all three simulations agree qualitatively. In terms of electron dynamics, which is not captured by the HVM code, the HVLF model reproduces the main features obtained with the fully kinetic treatment of the PIC code.

Magnetic reconnection and turbulence are intricately coupled in plasmas (Stawarz et al., 2024, this issue), where coherent structures such as magnetic holes, magnetic islands, and current sheets naturally develop (see, e.g., Matthaeus et al. (2015)). Then, current sheet widths tend to approach the kinetic scale, leading to magnetic reconnection. Hybrid-Vlasov simulations of turbulent plasmas have been successful in modelling both turbulence-induced “standard” reconnection with ion-coupling and

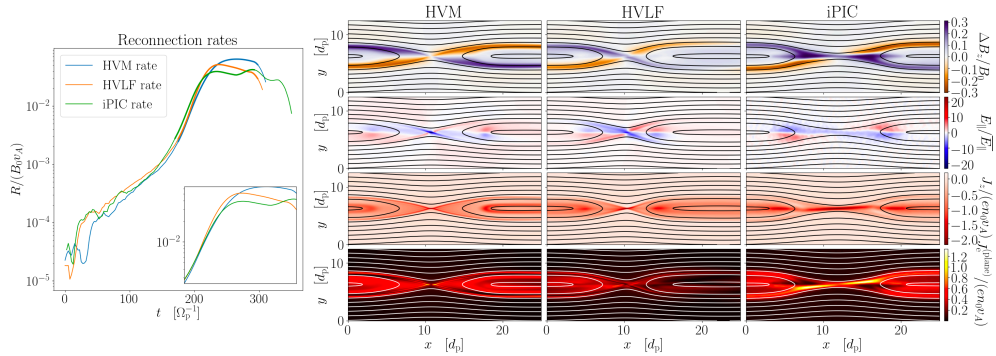


Fig. 17 Magnetic reconnection modeled using three different codes (HVM, HVLF and PIC). Left: normalized reconnection rate $R/B_0 v_A$. The inset shows the time interval corresponding to the ticker curves in the main plot. To ease the comparison, the curves in the inset are shifted in time. Right: (first row) out-of-reconnection-plane magnetic field $\Delta B_z/B_0 = (B_z - B_z(t=0))/B_0$ showing the expected Hall quadrupolar pattern; (second row) electric field parallel to the ambient magnetic field $E_{\parallel}/E_{\parallel}$, where E_{\parallel} is the root mean square of E_{\parallel} in the shown region; (third row) current density in the out-of-plane direction J_z ; (fourth row) electron current density in the plane $J_e^{(\text{in-plane})}$. The superposed black or white curves are the magnetic field lines. The three columns show results from the three different models. The left column show results from HVM at the simulation time $t = 237.5 \Omega_{cp}^{-1}$; the center column show results from the HVLF code at the simulation time $t = 232.5 \Omega_{cp}^{-1}$; the right column show results from the PIC code at the simulation time $t = 235.0 \Omega_{cp}^{-1}$. Ω_{cp} is the proton cyclotron frequency. Adapted from Finelli et al. (2021).

electron-only magnetic reconnection (Califano et al., 2020; Arrò, G. et al., 2020). A key result in the context of the interplay between reconnection and turbulence is the fact that turbulence is mediated by magnetic reconnection. More specifically, reconnection plays a key role in driving the onset of sub-ion turbulent cascade (Franci et al., 2017; Cerri et al., 2017; Manzini et al., 2023; Adhikari et al., 2024). Hybrid-Vlasov simulations with the HVM code have played a crucial role in providing evidence for the role played by reconnection in this context.

8.3.2 Global simulations

The main goal of Vlasiator is to model the solar wind–magnetosphere interaction with a hybrid-Vlasov approach. For this reason, the computational efforts have been mainly directed toward performing global simulations of the entire magnetosphere. As a consequence, a broad variety of magnetospheric plasma phenomena have been investigated using Vlasiator (notably collisionless shock (e.g., Johlander et al., 2022) and foreshock physics (e.g. Turc et al., 2023), magnetosheath jets (e.g. Suni et al., 2021), auroral proton precipitation (e.g. Grandin et al., 2020; Grandin et al., 2023) to mention a few). As magnetic reconnection plays a key role in magnetosphere dynamics, it has been investigated in several Vlasiator studies, both at the magnetopause (Pfau-Kempf et al., 2016; Hoilijoki et al., 2017, 2019; Akhavan-Tafti et al., 2020; Pfau-Kempf et al., 2020b) and in the magnetotail (Palmroth et al., 2017; Juusola et al., 2018; Runov et al., 2021; Palmroth et al., 2023). Since Vlasiator does not include an explicit resistive term, magnetic reconnection is enabled by the numerical diffusivity or resistivity.

In this section, we present key results from selected Vlasiator studies in two subsections, one devoted to magnetopause reconnection and the other focusing on magnetotail reconnection. We start with discussing 2D-3V simulations, and then present 3D-3V simulations since recent algorithmic improvements allowed running global, three-dimensional (3D-3V) hybrid-Vlasov simulations of Earth’s magnetosphere (Ganse et al., 2023).

Magnetopause Reconnection: Global simulations allow us to study the interaction between the solar wind and the magnetosphere, including how and to which extent dayside magnetic reconnection is affected by the solar wind and magnetosheath dynamics. Hoilijoki et al. (2017) investigate this topic by using a 2D-3V Vlasiator global simulation in the GSE polar xz plane, focusing in particular on the laminar or bursty nature of magnetic reconnection during steady solar wind conditions.

The simulation domain covers $x = [-94, +48] R_E$ and $z = [-56, +56] R_E$ ($R_E = 6371$ km is the Earth’s radius) and it features a 2D line dipole centered at the origin modelling the Earth’s magnetosphere dipole and scaled to match the geomagnetic dipole strength. The steady solar wind has a density $n = 1 \text{ cm}^{-3}$, a constant velocity $\mathbf{v}_{SW} = -750 \text{ km/s } \hat{\mathbf{x}}$ and a proton temperature of 0.5 MK. The interplanetary magnetic field (IMF) is directed purely southward and it has a magnitude of 5 nT. The resolution is uniform in the simulation domain; the spatial resolution is 300 km ($\sim 0.047 R_E \sim 1.3 d_{p,SW}$, where $d_{p,SW}$ is the proton inertial length in the solar wind) and the velocity space resolution is 30 km/s ($\sim 0.33 v_{th,p,SW}$, where $v_{th,p,SW}$ is the solar wind proton thermal speed). The solar wind flows into the simulation domain from the boundary at $x = +48 R_E$ with constant parameters. The boundaries of the simulation box are periodic in the out-of-plane y direction while the $-x$ and $\pm z$ boundaries apply copy boundary conditions. The inner boundary of the magnetosphere is a circle of radius $4.7 R_E$ centered at the origin and it enforces a static Maxwellian proton velocity distribution and perfect conductor field boundary conditions.

Hoilijoki et al. (2017) reported that, despite the steady solar wind conditions, magnetic reconnection at the subsolar magnetopause does not reach a steady state and it is very dynamic. Indeed, magnetic islands are constantly produced and the presence of multiple X-points is observed. The motion of the X-points appears to be mostly dictated by the outflow produced by the neighboring X-points. Hoilijoki et al. (2017) suggest that including the ion kinetic physics in the model promotes the development of a dynamic and bursty reconnection process at the dayside.

This study investigates also the reconnection rate at the multiple simultaneous X-points and how the rate is affected by the local plasma conditions near the X-point. In particular, the presence of mirror modes in the magnetosheath appears to affect the reconnection rate, in agreement with spacecraft observations (Laitinen et al., 2010). The dependence of the magnetopause reconnection rate upon the IMF direction is further investigated in global Vlasiator simulation by Hoilijoki et al. (2019). In particular, the run presented in (Hoilijoki et al., 2017) is compared to a run with similar parameters but with a positive component of the IMF ($B_{IMF} = [3.54, 0, -3.54] \text{ nT}$). The Sun-ward tilt of the IMF results in a smaller tangential field at the magnetopause, leading to a reduction of the reconnection rate with respect to the purely southward-directed IMF case. The presence of a non-zero $B_{x,IMF}$ introduces an asymmetry that

impacts the reconnection process in terms of flux transfer events (FTE) size, speed and occurrence rate. In particular, FTEs are observed more frequently in the Northern Hemisphere and they are smaller in size with respect to the Southern Hemisphere.

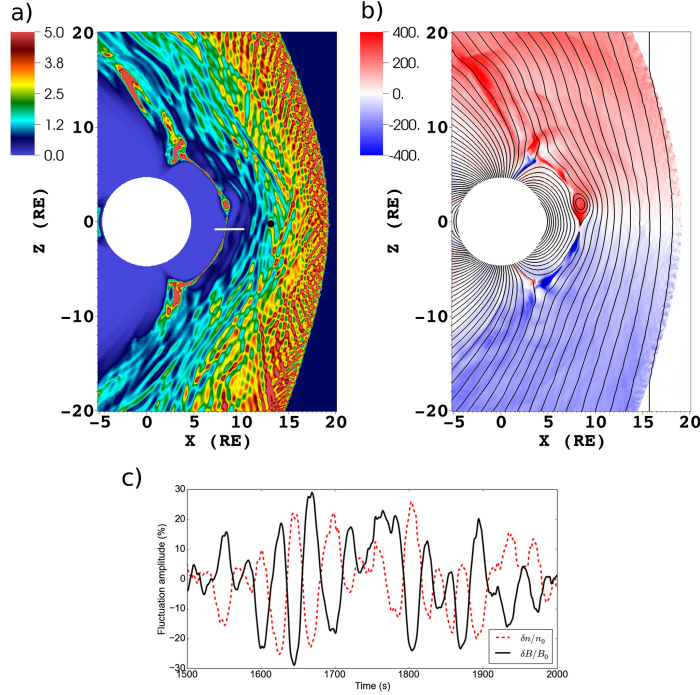


Fig. 18 (a) Plasma β ; (b) proton V_z . The black lines show the magnetic field lines. (c) Magnetic field strength (black solid) and plasma density (red dashed) fluctuations from the virtual spacecraft location indicated with the black dot in panel (a). The anticorrelation between magnetic field and density fluctuations is compatible with mirror mode waves. Adapted from Hoilijoki et al. (2017).

The findings of Hoilijoki et al. (2017) have been confirmed by Pfau-Kempf et al. (2020b), who analyze the reconnection process in a three-dimensional setup reproducing the magnetopause surface. In particular, Pfau-Kempf et al. (2020b) report a Vlasiator simulation of the noon–midnight meridional plane which is extended to cover $7 R_E$ in the dawn–dusk direction. The study by Pfau-Kempf et al. (2020b) is the first example of a 3D-3V Vlasiator simulation of a cylindrical geometry mimicking the subsolar dayside magnetosphere. While the dimensionality is increased, the cylindrical geometry and the limited extent in the y direction allow keeping the computational cost affordable and much lower than a global 3D-3V simulation modeling the entire magnetosphere.

The simulation domain covers $x = [-16, +31] R_E$, $x = [-3.5, +3.5] R_E$ and $z = [-35, +35] R_E$ and the solar wind and IMF parameters are the same used for the 2D-3V run reported in Hoilijoki et al. (2017) and discussed above. The spatial resolution is $\sim 0.24 R_E$, which is larger than the resolution of 2D-3V Vlasiator simulations because of the increased computational cost of 3D-3V runs.

Identifying the magnetic reconnection site in 3D settings is not as straightforward as in 2D-3V simulations, where the local behaviour of the flux function allows to identify saddle points corresponding to X points that are associated with reconnection sites. Hence, in this study the X-line location is estimated by combining the four-field junction method (Laitinen et al., 2006) with the identification of the locations exhibiting a flow reversal in the z direction. However, the four-field junction method is insufficient for identifying multiple reconnection X-lines. Pfau-Kempf et al. (2020b) find that, despite the uniform initial condition and the cylindrical symmetry in y , the X-line is not a straight line and it exhibits variations along the y direction. It is suggested that structures in the magnetosheath break the translation symmetry along y . Analogously to Hoilijoki et al. (2017), Pfau-Kempf et al. (2020b) point out that reconnection is bursty and patchy, with multiple reconnection sites being present at the various z and y locations across the magnetopause, despite the homogeneous and steady-state solar wind conditions.

Magnetotail Reconnection: Recently, magnetotail reconnection has been investigated in the context of a 3D-3V Vlasiator simulation investigating the dynamics of plasma eruptions (Palmroth et al., 2023). The three-dimensional simulation in both ordinary and velocity space is made possible by technological advances, notably by enabling static adaptive mesh refinement (AMR) for ordinary space (Ganse et al., 2023). With AMR, regions of high scientific interest such as the magnetotail plasma sheet are sampled with higher resolution ($0.16 R_E$) with respect to other regions in the simulations, the coarser resolution is $1.26 R_E$.

The 3D-3V simulation domain covers $x = [-111, +50] R_E$ and $y, z = [-58, +58] R_E$. The simulation parameters and initial conditions (IMF, solar wind density and speed) are the same adopted in (Hoilijoki et al., 2017). However, since this is a 3D-3V run, the Earth’s dipole is 3D and the inner boundary is a sphere of radius $4.7 R_E$, while the $\pm y$ boundaries apply copy boundary conditions, as the $\pm z$ boundaries. Differently from (Hoilijoki et al., 2017; Palmroth et al., 2018a; Juusola et al., 2018), where Ohm’s law included only the Hall term, this run includes the electron pressure gradient term as well. A polytropic closure is adopted for electrons, $\mathbf{P}_e = p_e \mathbf{I}$ and $p_e = n^\gamma T_e$, where \mathbf{P}_e is the electron pressure tensor, p_e is the scalar pressure, T_e is the electron temperature and n is the density. The polytropic index γ is set to $5/3$ (adiabatic).

Palmroth et al. (2023) focus on the investigation of magnetotail, revealing complex dynamics where magnetic reconnection and kinking instability co-exist in the magnetotail current sheet. In particular, in Fig. 19 it is shown that both processes are required to induce a global topological reconfiguration of the magnetotail, with the formation of a tail-wide plasmoid which is released and rapidly moves tailward. As mentioned above, the identification of the reconnection sites is challenging in 3D systems since we cannot rely on the identification based on the flux function. The reconnection site (X-line) in the magnetotail is identified by a combination of magnetic field and velocity proxies. X-lines and O-lines are identified as the locations where both $B_r = B_z = 0$, where B_r is the radial magnetic field component. The quantity $\partial B_z / \partial r$ allows us to distinguish between X-lines ($\partial B_z / \partial r > 0$ in the magnetotail) and O-lines ($\partial B_z / \partial r < 0$ in the magnetotail). The locations where an X-line

is co-located with a v_x reversal (diverging plasma flow) are identified as reconnection sites. [Palmroth et al. \(2023\)](#) further confirm that reconnection is ongoing at those locations by showing reconnection signatures such as the Hall electric field and ion demagnetization. In the 3D-3V run, a dominant tail-wide reconnection X-line is found at $X \sim -15 R_E$ throughout the simulation. The dominant X-line is very dynamic and new X-lines and O-lines with limited extent in the Y-direction are constantly formed.

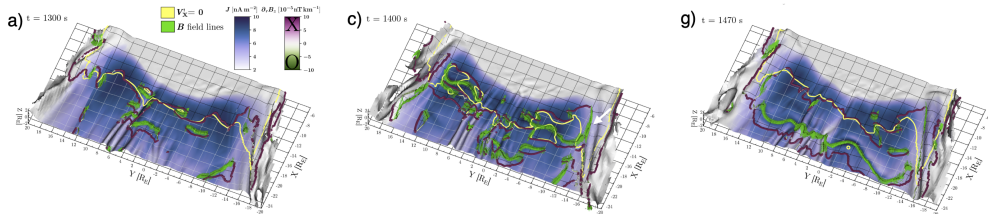


Fig. 19 Evolution of the magnetotail current sheet in a 3D-3V Vlasiator simulation. The panels show the current sheet surface (defined as $B_r = 0$) at different times, $t = 1300$ s (a), $t = 1400$ s (c), $t = 1470$ s (g). The color of the surface corresponds to the current density J . The yellow line indicates the flow reversal between the Earthward and tailward reconnection outflow. The magenta and green lines are locations where $B_r = 0$ and $B_z = 0$ and correspond to X-lines and O-lines (differentiated using the sign of $\partial B_z / \partial r$, which is positive at the X-lines and negative at the O-lines). The primary reconnection line is where the X-line (magenta) and flow reversal (yellow) contours are approximately co-located. The background grid shows the coordinates but also the magnetic-field topology: the black grid shows areas where the magnetic field is directed northward, and the white grid shows the areas where it is southward-directed. Adapted from [Palmroth et al. \(2023\)](#).

9 The Rice Convection Model

9.1 Introduction:

The Rice Convection Model (RCM), by definition, never includes the physics of reconnection. However, reconnection is a microscale/mesoscale process. Only a small fraction of the magnetic flux in the magnetosphere is included in reconnection at any given time. Including the RCM allows us to discuss how the reconnection process impacts the rest of the magnetosphere, specifically the inner magnetosphere, where the magnetic field lines are closed. Since the RCM's outer boundary condition comes from the plasmasheet, any process in the tail, such as reconnection, can impact the inner magnetosphere. Specifically, reconnection can generate low entropy bubbles that move toward the Earth at high speeds and can be a significant source of transport of plasma and magnetic field from the tail to the inner magnetosphere. In addition, the RCM helps quantitatively predict the plasmas from the inner magnetosphere which can reconnect on the dayside.

9.2 Assumptions and Equations

The physics behind the RCM can be found in detail in [Toffoletto et al. \(2003b\)](#) and [Wolf \(1983\)](#), and a detailed discussion of the use of the RCM can be found in [Wolf](#)

et al. (2016) and Toffoletto et al. (2003b), and ring current models are described by Toffoletto (2020). In the RCM, the distribution of magnetospheric particles is assumed to be isotropic. A key variable is the isotropic energy invariant

$$|\lambda_k| = W(\lambda_k, \mathbf{x}, t) V^{2/3} \quad (84)$$

where W is the particle kinetic energy, including bounce and gyro motion and the sign of λ_k is positive for positive ions and negative for electrons. The flux tube volume is

$$V = \int_{sh}^{nh} \frac{ds}{B(\mathbf{x}, t)} \quad (85)$$

where the integral extends along the field line from the southern to the northern ionosphere.

The motions of magnetospheric particles in the inner magnetosphere are assumed to be governed by

$$\text{Drift velocity} \ll \text{bounce motion} \ll \text{gyro motion}$$

The RCM calculates the bounce-averaged drift velocity, including gradient, curvature, and $E \times B$ drifts, i.e.,

$$\mathbf{v}_k = \frac{\left(\mathbf{E} - \frac{1}{q_k} \nabla W(\lambda_k, \mathbf{x}, t) \right) \times \mathbf{B}(\mathbf{x}, t)}{B(\mathbf{x}, t)^2} \quad (86)$$

where q_k is the charge of a particle of species k . Inertial drift is assumed to be negligible. The quantity $\eta_k(\mathbf{x}, t)$ is defined as the number of particles per unit magnetic flux for particles of a specific chemical species and a specific value of energy invariant. It follows a conservation law (Wolf, 1983)

$$\left[\frac{\partial}{\partial t} + \mathbf{v}_k(\lambda_k, \mathbf{x}, t) \cdot \nabla \right] \eta_k = -L(\eta_k) \quad (87)$$

where L is the loss rate of particles due to precipitation and charge exchange. The classic RCM neglects particles flowing up from the ionosphere to the magnetosphere. In the early 2000's Stan Sazykin and Darren DeZeeuw implemented a grid-based scheme using the CLAWPAK package (Mandli et al., 2016) that was more robust but a bit more diffusive than the earlier Lagrangian scheme.

The flux tube content η_k is related to the thermodynamic pressure P

$$PV^{5/3} = \frac{2}{3} \sum_k \eta_k |\lambda_k| \quad (88)$$

while the flux tube content is related to the plasma distribution function $f_k(\lambda)$ as

$$\eta_k = \frac{4\pi 2^{1/2}}{m_k^{3/2}} \int_{\lambda_{min}}^{\lambda_{max}} |\lambda|^{1/2} f_k(\lambda) d\lambda \quad (89)$$

where $(\lambda_{max} - \lambda_{min})$ is the width of the invariant energy channel associated with species k . The species k is defined for a given chemical species (usually e^- , H^+ , O^+), and the specific value of the energy invariant.

The electric field can be expressed as the sum of a potential component and an inductive component

$$\mathbf{E} = -\nabla\Phi - \mathbf{v}_{induction} \times \mathbf{B} \quad (90)$$

In the RCM, the inductive electric field is included implicitly through time-dependent magnetic field mappings. The inductive magnetic field in the ionosphere is assumed to be zero there; however, it is not zero in the magnetosphere.

There are two more complications in the electric field:

1. In the classic RCM, we assume the electric field is perpendicular to the magnetic field.
2. There are two coordinate systems used in the classic RCM. One moves with the Earth as it rotates, and the potential in that system is labeled Φ_i . The other does not rotate with the Earth, is approximately an inertial system, and is labeled Φ .

We can translate from one system to the other in the ionosphere using the formula

$$\Phi = \Phi_i - \frac{\omega_E B_0 R_E^3 \sin^2(\theta_i)}{R_i} \quad (91)$$

where ω_E is the angular rotation rate of the Earth, B_0 is the magnetic field at the Earth's equator, R_E is the radius of the Earth, θ_i is the colatitude, and R_i is the radius of the ionosphere. Equation 91 applies to the equatorial plane, but it applies only to a dipole magnetic field. To compute Φ in the equatorial plane of the magnetosphere, the RCM calculates Φ by mapping between the ionosphere to the equatorial plane, assuming Φ is constant along each field line.

In the thin-shell approximation, the equation for the conservation of current is ($\nabla \cdot \mathbf{J} = 0$) can be written

$$\nabla_i \cdot \left[\overleftrightarrow{\Sigma} \cdot (\nabla_i \Phi_i) \right] = (j_{\parallel nh} - j_{\parallel sh}) \sin(I) \quad (92)$$

where $\overleftrightarrow{\Sigma}$ is the field-line integrated conductivity tensor due to both hemispheres, I is the dip angle of the magnetic field in the ionosphere, and $j_{\parallel nh} - j_{\parallel sh}$ is the ionospheric field-aligned current density.

The [Vasyliunas \(1970\)](#) equation, which is based on force balance

$$\mathbf{J} \times \mathbf{B} - \nabla P = 0 \quad (93)$$

is given by

$$\frac{j_{\parallel nh} - j_{\parallel sh}}{B_i} = \frac{\hat{b}}{B} \cdot \nabla V \times \nabla P \quad (94)$$

which relates field-aligned currents in the ionosphere to pressure gradients in the magnetosphere, and B_i is the magnetic field at the southern- and northern-ionospheric footprints of the field line (assumed the same). The derivation makes use of the fact the right-hand side of Eqn. 94 can be evaluated anywhere along the field line. The RCM equations are solved on a fixed ionospheric grid that has variable grid spacing in latitude to better resolve the auroral zone. The RCM grid is time-dependent in the equatorial plane, ranging from just inside the magnetopause on the dayside to $10 - 20R_E$ on the night side.

9.3 Inputs, Boundary, and Initial conditions and Outputs

The magnetic field model: For many years, the RCM assumed a constant magnetic field, but, beginning about 2000 the RCM used a time-dependent semi-empirical model such as the Tsgyanenko models (1989, 1995, 2003). The RCM can also use the Hilmer and Voigt (1995) magnetic field model. In classic RCM runs, the magnetic field is not designed to be consistent with Ampere’s law and equation 93. Ways of including eqn. 93 consistently in the RCM are described in Section 9.4. In the ionosphere, where the magnetic field is assumed to be dipolar, the magnetic field is

$$\mathbf{B}_i = -\frac{\mu_0}{4\pi} \frac{\mathbf{M}_E - 3\hat{r}(\mathbf{M}_E \cdot \hat{r})}{R_i^3} \quad (95)$$

where \hat{r} is the radial unit vector in the ionosphere, and \mathbf{M}_E is the magnetic moment, which is in the southern direction, and

$$B_i = \hat{r} \cdot \mathbf{B}_i \quad (96)$$

Ionospheric conductance: Ionospheric conductance has two major drivers: Solar heating (e.g., the Sheffield University Ionosphere Plasmasphere (SUPIM) model, Bailey et al. (1997)). The second is Auroral heating. The standard treatment uses the electron precipitating energy flux and average energy (Robinson et al., 1987).

Loss models: Separate models are needed for electrons and ions. The simplest electron loss model assumes a fixed fraction of strong pitch-angle scattering, often between 33% and 67% (Schumaker et al., 1989). That procedure is reasonable for the plasma sheet but overestimates the electron loss rate in the inner magnetosphere. A slightly more sophisticated model (Chen and Schulz, 2001) is somewhat more realistic. For the Ion loss model, there are many theoretical models of ion charge exchange. The overall ion loss rate for an energy and L value is calculated using an algorithm developed by James Bishop (Freeman et al., 1993; Bishop, 1996).

The RCM needs boundary conditions both at its outer (large L) boundary and at its lowest (low L) boundary. The large- L boundary depends on MLT as well as UT. Note that the large- L boundary can’t be aligned with the grid, except in a few cases. At this boundary, the number η_s which is the number of particles for a given type

s per weber of magnetic flux, is needed as well as the potential distribution, which can be a simple function of solar wind conditions or an empirical model such as the Weimer model (1985).

The low-L boundary (low-latitude) is set at least a few degrees latitude from the equator. Given the aligned-dipole assumption, the latitudinal current density should, in principle, be zero at the equator. The RCM and many other models use a thin-wire approximation to represent the region near the equator, to provide a boundary condition

$$\frac{\partial J_\theta}{\partial \theta} + S \frac{\partial J_\phi}{\partial \phi} = 0 \quad (97)$$

which was derived by [Blanc and Richmond \(1980\)](#). Here J is the current density, θ is the colatitude coordinate, and ϕ is the longitudinal coordinate. S is a function of ϕ that was defined by [Blanc and Richmond \(1980\)](#).

Initial conditions: These are needed to provide the value of the initial value of η_k , which is a function of grid location and time. The RCM can be initialized with an empty value and run for a period of time to fill in the inner magnetosphere. Alternatively, the RCM uses the [Spence et al. \(1989\)](#) model for the initial pressure distribution. Earlier versions of the RCM assumed a Maxwellian distribution, but more recent versions have the option to assume a kappa distribution (e.g., [Yang et al. \(2015\)](#)).

RCM outputs: The main RCM outputs are the electric potential (Φ), field-aligned currents ($j_{\parallel nh} - j_{\parallel sh}$), the distribution function (η_s) and moments (pressure and density) within the RCM modeling region in the ionosphere and the magnetospheric equatorial plane.

9.4 Generalizations of the RCM

There have been many modifications to the RCM, particularly since 2000.

Other planets: Tom Hill and several of his students modified the RCM to be appropriate for Jupiter and Saturn. Jupiter's moon Io has volcanoes that loft neutrals and positive ions into the inner magnetosphere, and there is also a similar effect at Saturn's moon Enceladus. Centrifugal force is stronger than gravity near Io, and the region beyond Io is consequently interchange unstable. In the simulations, plasma develops finger-like structures, moving outward because of centrifugal force and azimuthally because of Coriolis force. The clearest magnetospheric signature of interchange transport occurs in the inner magnetosphere of Saturn, where the hot plasma injection-dispersion structures are evident ([Hill et al. \(2005\)](#) and references therein).

CRCM (Comprehensive Ring Current Model): This model ([Fok et al., 2001](#)) was similar to the classic RCM, except that it used a much more complete equation for the distribution function. Whereas the classic RCM assumed an isotropic pitch-angle distribution, CRCM assumes conservation of the first and second invariant. Additional terms account for precipitation and charge-exchange losses and pitch-angle scattering. CIMI (Comprehensive Inner Magnetosphere Model) includes radiation belt electrons and the plasmasphere ([Fok et al., 2014](#)).

RCM-E: In the classic RCM, the magnetic field was not required to satisfy the force balance equation $\mathbf{J} \times \mathbf{B} = \nabla P$ but $P = (2/3)V^{-5/3} \sum_k |\lambda_k| \eta_k$ and η_k was based on the theoretical equation 87. The RCM-E (equilibrium) is run for a small time step (typically 1 – 5 minutes), and a modified MHD code, called the “friction code”, recalculates the magnetic field in order to make it approximately consistent with $\mathbf{J} \times \mathbf{B} = \nabla P$ (Lemon et al., 2003). For conditions of strong convection, the time development of the RCM-E would cause the magnetic field to be tail-like and more like a substorm growth phase. If PV^γ was constant on the nightside large L - boundary, it became difficult to form a realistic strong ring current (Lemon et al., 2004). The RCM-E usually exhibited the pressure balance inconsistency (Erickson and Wolf, 1980). In other words, the more theoretically consistent model became a less realistic representation of observations. Other modelers have developed models that are variants of the RCM-E (e.g., Chen et al. (2012) or the RAM-SCB model (Zaharia et al., 2006a)) that use an alternative ring current and force balance model. The solution to the pressure balance inconsistency turned out to be bursty bulk flows (BBFs), which are localized regions of the inner and middle plasma sheet (Angelopoulos et al., 1992) that flow rapidly earthward. The flow bursts, which are also often called “bubbles”, often move very fast (typically 400km/s). These flows correspond to regions of low PV^γ (Pontius Jr and Wolf, 1990). Angelopoulos et al. (1992) found that BBFs account for a large fraction of the total earthward flow in the plasma sheet. BBFs usually terminate about the inner edge of the plasma sheet, although some of the fast flows penetrate the ring current (Gkioulidou et al., 2014; Yang et al., 2016). Lemon et al. (2004) produced a substantial ring current injection by reducing the PV^γ at the RCM’s outer boundary over a limited region of local time, simulating a ring current injection during a storm. Yang et al. (2014a) showed a possible relation to the streamers observed in the polar cap and bubbles in the plasma sheet, and Yang et al. (2014b) argued that this effect could account for pressure balance inconsistency and that during storms low entropy flux tubes could account for up to 60% of the ring current (Yang et al., 2015). See also the section 9.5 “Large, coupled models that include RCM”.

RCM-I (RCM-Inertial): The main problem with using RCM-E to represent BBFs is they move so fast that the assumption of force balance is not valid. Yang et al. (2019) developed a more complex version of the RCM that includes inertial effects in a very approximate way. Equation 92 is replaced by a much more complex expression that involves a $\partial\Phi/\partial t$ term.

9.5 Large, coupled models that include RCM

Single fluid, global MHD models have become powerful tools in recent years (e.g., Lyon et al. (2004); Raeder et al. (2001), Zhang et al. (2019)). However, these models do not capture all the important physics in the inner magnetosphere where gradient and curvature drifts become important but are neglected in MHD. Coupling these models is a daunting task as the modeling regions overlap in space and information is fed back and forth between them. There are different physics assumptions associated with each model: the RCM model assumes slow flow and force balance and neglects waves, while MHD does not. However, MHD does not include energy-dependent drifts that

are important in the inner magnetosphere. There have been several successful efforts to couple the RCM with global MHD, which provides many of the inputs used by the RCM (boundary and initial conditions) such as the magnetic field, plasma density, and pressure as well as the ionospheric potential. In return, the RCM provides the density and pressure that are derived from computing the moments from the RCM distribution function that have been subject to energy-dependent drifts.

SMWF: The earliest successful coupling effort was [De Zeeuw et al. \(2004\)](#) which merged the BATS-R-US Global MHD ([Tóth et al., 2005](#)) code with the RCM. The RCM was embedded in the Global MHD code as a subroutine that later became part of the Space Weather Modeling Framework (SWMF) ([Tóth et al., 2005](#)). Each coupling exchange requires computing many field-line integrals to obtain the flux tube volume (equation 1), which is used by the RCM, and the mapping of the 2D RCM quantities into the 3D domain of the MHD code, which is then used to update the MHD. This field line tracing requires using a parallelized and efficient field line tracer that exploits the nested adaptive grid used in the MHD code (e.g., [De Zeeuw et al. \(2004\)](#)). This version of the model demonstrated that including the RCM increased the pressure in the inner magnetosphere ring current region as compared to standalone MHD. The RCM also was able to model the region-2 currents in the ionosphere. Later versions of the SWMF also include other inner magnetosphere models such as the Comprehensive Ring current model (CRCM) ([Glocer et al., 2013](#)) and other models ([Tóth et al., 2012](#)), becoming the first coupled magnetosphere model to be used in the Community Coordinated Modeling Center (CCMC).

LFM-RCM: [Pembroke et al. \(2012\)](#) coupled the RCM to the Lyon Fedder Mobary (LFM) global MHD code ([Lyon et al., 2004](#)) that included the MIX ionosphere model ([Merkin and Lyon, 2010](#)). This approach used a loose coupling scheme where the models (LFM, MIX, and RCM) ran independently as separate processes and used the InterComm software package to exchange information at pre-set intervals ([Lee and Sussman, 2004](#)). In this model, RCM returned both pressure and density to the MHD code and included a simple static plasmasphere based on the [Gallagher et al. \(2000\)](#) empirical model. Since the RCM was only tracking the distribution function and not computing the potential as in the standalone RCM, the assumption of zero dipole tilt could be relaxed in the coupled model, allowing for more realistic simulations. The resulting coupled model was very dynamic, especially during geomagnetic storm simulations, and significantly impacted the ring current region (e.g., [Wiltberger et al. \(2017\)](#)). To keep the code stable, the RCM boundary was restricted to regions where the field line average plasma beta was less than 1. With moderately strong solar wind driving, the coupled model produced a strong ring current and region-2 currents.

OpenGGCM-RCM: [Hu et al. \(2010\)](#) and [Cramer et al. \(2017\)](#) coupled the OpenGGCM global MHD code to RCM ([Raeder et al., 2001](#)) that also includes the Coupled Thermosphere-Ionosphere Model (CTIM) ([Fuller-Rowell et al., 1996](#)). The RCM is embedded within the MHD code, where the feedback to the MHD code used a configurable ramp-up region based on the strength of the magnetic field for numerical stability. [Cramer et al. \(2017\)](#) found that most of the transport of plasma to the inner magnetosphere is via low entropy bubbles, consistent with [Yang et al. \(2015\)](#). [Raeder et al. \(2016\)](#) also used the coupled model to simulate a geomagnetic storm and showed

that it developed subauroral polarization streams (SAPS) from electron precipitation computed from the MHD code. [Hu et al. \(2011\)](#) examined the entropy profile in an idealized Open GGCM simulation and found that violations of the frozen-in-flux in MHD could lead to an entropy profile that produced a low entropy bubble that was earthward of an entropy enhancement. Such a configuration causes the bubble/blob pair to move earthward/tailward, which thins the current sheet in the region between them and can ultimately result in tearing or other configuration changes.

MAGE: The newest version of a global magnetosphere model is the Multi-scale Atmosphere Geospace Environment Model (MAGE) that couples the RCM to the Grid Agnostic MHD for Extended Research Application (GAMERA) global MHD code ([Zhang et al., 2019](#); [Sorathia et al., 2021](#)), the ReMIX ionosphere model ([Merkin and Lyon, 2010](#)) which is a revised version of the MIX solver, and the NCAR Thermosphere-Ionosphere- Electrodynamics General Circulation Model (TIE-GCM) [Roble et al. \(1988\)](#). The GAMERA MHD model is derived from the LFM model but with improved numerical algorithms and updated software designed for efficient use on modern supercomputers. The coupling to the RCM has also been significantly improved and modernized, for example, it uses a highly configurable and customizable parallel field line tracer. Other improvements include moving the RCM boundary in MAGE further from the Earth compared to the coupled LFM-RCM code, allowing more plasma from the plasmashet to move into the RCM modeling region, and the option of a Maxwellian distribution to compute RCM distribution functions replaced with a Kappa distribution ([Sciola et al., 2023](#)). The new model also includes improved loss rate mechanisms for electrons [Bao et al. \(2023\)](#) where the electron precipitation model is based on RCM-computed electron energy fluxes that are used to modify the ionospheric conductances ([Lin et al., 2022a](#)). The use of this conductance model was found to influence the formation of the SAPS channel ([Lin et al., 2021a](#)). The model also includes a dynamic plasmasphere density that is tracked using a zero-energy channel in the RCM that is fed back to the MHD model ([Bao et al., 2023](#)). [Pham et al. \(2022\)](#) used the coupled MAGE model to investigate the impact on thermospheric density perturbations produced by traveling ionospheric disturbances. [Sciola et al. \(2023\)](#) found that in the MAGE model, fast magnetospheric flows associated with low entropy channels can contribute over 50% of the ring current population, consistent with [Yang et al. \(2015\)](#) and [Cramer et al. \(2017\)](#).

9.6 Summary

While the RCM does not model reconnection, it is impacted by it. Reconnection in the tail produces low entropy flux tubes that rapidly interchange their way toward the Earth (e.g., [Wiltberger et al. \(2015\)](#); [Sorathia et al. \(2021\)](#)). Some of these flux tubes make it into the inner magnetosphere and play an important role in the formation and structure of the ring current region. It can also have ionospheric effects such as the formation of streamers. Over the years, the RCM has helped illuminate the impact of processes in the tail on the inner magnetosphere. This is especially true using the new generation coupled models that have been developed in recent years. However, there are several limitations in the models that present challenges. One is the modeling of

the region in the tail where the magnetic field is transitioning from a stretched tail-like configuration to a dipole. When fast flows appear in this region, as they often do, neither MHD, which neglects gradient/curvature drifts, nor the RCM, which assumes slow flow, are applicable.

Furthermore, including the RCM in MHD models can also affect the location and effectiveness of dayside reconnection as well. Since the Region 2 FACs modeled by the RCM shields the inner magnetosphere from convection, it also strongly affects the distribution of return flow back to the dayside boundary. The RCM has been successful in modeling the plasmaspheric plumes that can bring dense plasmas to the dayside reconnection regions (Goldstein et al. (2002); Huba and Sazykin (2014); Bao et al. (2023)). Dayside SWMF runs that include RCM all successfully place MMS within 1 RE of an X-line (or separatrix) whenever clear EDRs are observed (e.g. Reiff et al. (2017)).

The next generation coupled models will need to add the effect of ionospheric plasma sources (e.g., Glocer et al. (2009a); Varney et al. (2016)), which will ultimately require a multi-fluid MHD model coupled to a ring current model and includes a model of ionospheric outflow to track all the species in the magnetosphere.

10 Conclusions

In this paper, we have presented a “brief” overview of the large collection of computational methods that are used to study magnetic reconnection. It should be clear to the reader of this text, that simulating magnetic reconnection is nearly a separate field of study in and of itself. It should be and has been (Büchner et al., 2003) the topic of entire books. The single element to take away from this paper is that simulating a multifaceted and multiscale problem like magnetic reconnection is not a simple endeavor. Both plasma models and simulation initial conditions must be tuned carefully to match the goals of the study.

We have reviewed simulation methods for magnetic reconnection in space plasmas, from macroscopic MHD scales to microscopic kinetic scales. Basically, macroscopic plasma behaviors can be simulated based on fluid modes, and as we resolve smaller scale physics, kinetic models need to be implemented in simulations. In addition, we have reviewed novel approaches to incorporate multi-scale physics.

MHD simulations are useful to study large scale physics, including performing global simulations for planetary magnetospheres. We have discussed the basic algorithm for MHD simulations, and also how to implement test particles that follow MHD fields. Hall MHD simulations contain the Hall physics, which allows kinetic scale waves to propagate, mediating fast reconnection. We have reviewed recent progresses of Hall MHD studies, and also the effect of the electron inertia term and EMHD.

Hybrid PIC simulations and full PIC simulations include particle kinetic physics, where particle motions are directly solved by equations of motion of particles. For hybrid simulations, we have reviewed techniques to overcome the limitation of spatiotemporal resolutions in global models, and also the implementation of electron

kinetic physics into hybrid simulations. For full PIC simulations, we have reviewed simulation studies of magnetic reconnection in magnetotail and magnetopause, particle acceleration, and shock driven reconnection.

Next, we have reviewed two novel approaches to address multi-scale physics in magnetic reconnection: Embedded PIC, and kglobal. In the embedded PIC approach, the macro-scale region is solved using MHD equations, and local kinetic domains are embedded in the MHD domain, where full PIC techniques are employed. In kglobal, on the other hand, equations for the ion and electron fluids are combined with particles' equations for electrons, and the macro-scale evolution is modified by the kinetic physics.

Finally, we have reviewed two types of other simulation techniques: Vlasov simulations and the Rice convection model. In Vlasov simulations, kinetic effects are implemented in simulations by solving 2D-3V or 3D-3V Vlasov equations. We have discussed recent progresses of studies by Vlasov models from local reconnection simulations to global simulations. The Rice convection model is a kinetic approach to simulate physics of the inner magnetosphere, where bounce averaged particle drift motion is taken into account.

References

- Adhikari S, Parashar TN, Shay MA, Matthaeus WH, Pyakurel PS, Fordin S, Stawarz JE, Eastwood JP (2021) Energy transfer in reconnection and turbulence. *Physical Review E* 104:065206
- Adhikari S, Yang Y, Matthaeus WH, Cassak PA, Parashar TN, Shay MA (2024) Scale filtering analysis of kinetic reconnection and its associated turbulence. *Physics of Plasmas* 31(2)
- Akhavan-Tafti M, Palmroth M, Slavin JA, Battarbee M, Ganse U, Grandin M, Le G, Gershman D, Eastwood JP, Stawarz J (2020) Comparative analysis of the vlsiator simulations and mms observations of multiple x-line reconnection and flux transfer events. *Journal of Geophysical Research: Space Physics* 125(7):e2019JA027410, DOI 10.1029/2019JA027410
- von Alftan S, Pokhotelov D, Kempf Y, Hoilijoki S, Honkonen I, Sandroos A, Palmroth M (2014) Vlsiator: First global hybrid-Vlasov simulations of Earth's foreshock and magnetosheath. *J Atmospheric and Solar-Terrest Phys* 120:24–35
- Alho M, Wedlund CS, Nilsson H, Kallio E, Jarvinen R, Pulkkinen T (2019) Hybrid modeling of cometary plasma environments. *Astronomy & Astrophysics* 630:A45, DOI 10.1051/0004-6361/201834863, URL <https://doi.org/10.1051/0004-6361/201834863>
- Alho M, Battarbee M, Pfau-Kempf Y, Khotyaintsev YV, Nakamura R, Cozzani G, Ganse U, Turc L, Johlander A, Horaites K, Tarvus V, Zhou H, Grandin M, Dubart M, Papadakis K, Suni J, George H, Bussov M, Palmroth M (2022) Electron signatures of reconnection in a global evlsiator simulation. *Geophysical Research Letters* 49(14):e2022GL098329, DOI <https://doi.org/10.1029/2022GL098329>, e2022GL098329 2022GL098329, <https://agupubs.onlinelibrary.wiley.com/doi/pdf/10.1029/2022GL098329>

- Allmann-Rahn F, Grauer R, Kormann K (2022) A parallel low-rank solver for the six-dimensional vlasov–maxwell equations. *Journal of Computational Physics* 469:111562, DOI <https://doi.org/10.1016/j.jcp.2022.111562>, URL <https://www.sciencedirect.com/science/article/pii/S0021999122006246>
- Amano T, Higashimori K, Shirakawa K (2014) A robust method for handling low density regions in hybrid simulations for collisionless plasmas. *Journal of Computational Physics* 275:197–212
- Angelopoulos V, Baumjohann W, Kennel C, Coroniti FV, Kivelson M, Pellat R, Walker R, Lühr H, Paschmann G (1992) Bursty bulk flows in the inner central plasma sheet. *Journal of Geophysical Research: Space Physics* 97(A4):4027–4039
- Arencibia M, Cassak PA, Shay MA, Priest ER (2021) Scaling theory of three-dimensional magnetic reconnection spreading. *Physics of Plasmas* 28(8)
- Arencibia M, Cassak PA, Shay MA, Qiu J, Petrinec SM, Liang H (2022) Three-dimensional magnetic reconnection spreading in current sheets of non-uniform thickness. submitted
- Arnold H, Drake J, Swisdak M, Dahlin J (2019) Large-scale parallel electric fields and return currents in a global simulation model. *Physics of Plasmas* 26(10)
- Arnold H, Drake JF, Swisdak M, Guo F, Dahlin JT, Chen B, Fleishman G, Glesener L, Kontar E, Phan T, et al. (2021) Electron acceleration during macroscale magnetic reconnection. *Physical review letters* 126(13):135101
- Arrò, G, Califano, F, Lapenta, G (2020) Statistical properties of turbulent fluctuations associated with electron-only magnetic reconnection. *A&A* 642:A45, DOI 10.1051/0004-6361/202038696, URL <https://doi.org/10.1051/0004-6361/202038696>
- Ashour-Abdalla M, El-Alaoui M, Goldstein ML, Zhou M, Schriver D, Richard R, Walker R, Kivelson MG, Hwang KJ (2011) Observations and simulations of non-local acceleration of electrons in magnetotail magnetic reconnection events. *Nature Physics* 7(4):360–365
- Attico N, Califano F, Pegoraro F (2000) Fast collisionless reconnection in the whistler frequency range. *Physics of Plasmas* 7(6):2381–2387, DOI 10.1063/1.874076
- Aydemir AY (1992) Nonlinear studies of $m = 1$ modes in high-temperature plasmas. *Phys Fluids B* 4:3469
- Bailey G, Balan N, Su Y (1997) The sheffield university plasmasphere ionosphere model—a review. *Journal of Atmospheric and Solar-Terrestrial Physics* 59(13):1541–1552
- Balsara DS (2009) Divergence-free reconstruction of magnetic fields and WENO schemes for magnetohydrodynamics. *Journal of Computational Physics* 228(14):5040 – 5056, DOI 10.1016/j.jcp.2009.03.038
- Bao S, Toffoletto F, Merkin S, Wang W, Sorathia K, Lin D, Pham K, Garretson J, Wiltberger M, Lyon J, Michael A (2023) Drivers of the geospace plume: Mage simulation of the march 31 2001 super storm. In preparation
- Battarbee M, Brito T, Alho M, Pfau-Kempf Y, Grandin M, Ganse U, Papadakis K, Johlander A, Turc L, Dubart M, Palmroth M (2021) Vlasov simulation of electrons in the context of hybrid global models: an evlasiator approach. *Annales Geophysicae* 39(1):85–103, DOI 10.5194/angeo-39-85-2021, URL <https://angeo.copernicus.org/articles/39/85/2021/>

- Bessho N, Chen LJ, Wang S, Hesse M, III LBW (2019) Magnetic reconnection in a quasi-parallel shock. *Geophys Rev Lett* 46:9352
- Bessho N, Chen LJ, Wang S, Hesse M, III LBW, Ng J (2020) Magnetic reconnection and kinetic waves generated in the earth's quasi-parallel bow shock. *Phys Plasmas* 27:092901
- Bessho N, Chen LJ, Stawarz JE, Wang S, Hesse M, III LBW, Ng J (2022) Strong reconnection electric fields in shock-driven turbulence. *Phys Plasmas* 29:042304
- Bessho N, Chen LJ, Hesse M, Ng J, III LBW, Stawarz JE (2023) Electron acceleration and heating during magnetic reconnection in the earth's quasi-parallel bow shock. *The Astrophysical Journal* 954:25
- Biermann L (1950) Über den Ursprung der Magnetfelder auf Sternen und im interstellaren Raum (mit einem Anhang von A. Schlüter). *Zeitschrift Naturforschung Teil A* 5:65
- Birdsall CK, Langdon AB (1991) *Plasma physics via computer simulation*. Adam Hilger, Bristol
- Birn J, Hesse M (1991) The substorm current wedge and field-aligned currents in MHD simulations of magnetotail reconnection. *Journal of Geophysical Research: Space Physics* 96(A2):1611–1618
- Birn J, Hesse M (1994) Particle acceleration in the dynamic magnetotail: Orbits in self-consistent three-dimensional MHD fields. *Journal of Geophysical Research: Space Physics* 99(A1):109–119
- Birn J, Hesse M (2000) Large-scale stability of the magnetotail. In: *Fifth International Conference on Substorms*, vol 443, p 15
- Birn J, Hesse M (2014) The substorm current wedge: Further insights from MHD simulations. *Journal of Geophysical Research: Space Physics* 119(5):3503–3513
- Birn J, Hones Jr EW (1981) Three-dimensional computer modeling of dynamic reconnection in the geomagnetic tail. *Journal of Geophysical Research: Space Physics* 86(A8):6802–6808
- Birn J, Priest ER (eds) (2007) *Reconnection of Magnetic Fields*. Cambridge University Press, Cambridge, DOI 10.1017/CBO9780511536151, URL <https://www.cambridge.org/core/product/identifier/9780511536151/type/book>
- Birn J, Schindler K (2002) Thin current sheets in the magnetotail and the loss of equilibrium. *Journal of Geophysical Research: Space Physics* 107(A7):SMP–18
- Birn J, Drake JF, Shay MA, Rogers BN, Denton RE, Hesse M, Kuznetsova M, Ma ZW, Bhattacharjee A, Otto A, Pritchett PL (2001a) GEM magnetic reconnection challenge. *J Geophys Res* 106:3715
- Birn J, Drake JF, Shay MA, Rogers BN, Denton RE, Hesse M, Kuznetsova M, Ma ZW, Bhattacharjee A, Otto A, Pritchett PL (2001b) Geospace Environmental Modeling (GEM) magnetic reconnection challenge. *J Geophys Res* 106(A3):3715–3720, DOI 10.1029/1999JA900449
- Birn J, Thomsen M, Hesse M (2004) Electron acceleration in the dynamic magnetotail: Test particle orbits in three-dimensional magnetohydrodynamic simulation fields. *Physics of Plasmas* 11(5):1825–1833
- Birn J, Merkin V, Sitnov M, Otto A (2018) MHD stability of magnetotail configurations with a Bz hump. *Journal of Geophysical Research: Space Physics* 123(5):3477–3492

- Birn J, Hesse M, Runov A (2022) Electron anisotropies in magnetotail dipolarization events. *Frontiers in Astronomy and Space Sciences* 9:908730
- Bishop J (1996) Multiple charge exchange and ionization collisions within the ring current-geocorona-plasmasphere system: Generation of a secondary ring current on inner l shells. *Journal of Geophysical Research: Space Physics* 101(A8):17325–17336
- Biskamp D (1986) Magnetic reconnection via current sheets. *Phys Fluids* 29:1520
- Biskamp D (1996) Magnetic reconnection in plasmas. *Astrophysics and Space Science* 242:165–207
- Biskamp D (2000) *Magnetic Reconnection in Plasmas*. Cambridge University Press, Cambridge, DOI 10.1017/CBO9780511599958, URL <http://ebooks.cambridge.org/ref/id/CBO9780511599958>
- Blanc M, Richmond A (1980) The ionospheric disturbance dynamo. *Journal of Geophysical Research: Space Physics* 85(A4):1669–1686
- Blanco-Cano X, Kajdič P, Omidi N, Russell C (2011) Foreshock cavitons for different interplanetary magnetic field geometries: Simulations and observations. *Journal of Geophysical Research: Space Physics* 116(A9)
- Bohdan A, Niemiec J, Kobzar O, Pohl M (2017) Electron pre-acceleration at nonrelativistic high-mach-number perpendicular shocks. *Astrophys J* 847:71
- Bohdan A, Pohl M, Niemiec J, Vafin S, Matsumoto Y, Amano T, Hoshino M (2020) Kinetic simulations of nonrelativistic perpendicular shocks of young supernova remnants. *Astrophys J* 893:6
- Boris JP (1970) Relativistic plasma simulation-optimization of a hybrid code. *Proceeding of the 4th Conference on Numerical Simulation of Plasmas*
- Brackbill JU, Lapenta G (2008) Magnetohydrodynamics with implicit plasma simulation. *Comm Comput Phys* 4:433–456
- Braginskii SI (1965) Transport processes in a plasma. In: Leontovich MA (ed) *Reviews of Plasma Physics*, vol 1, Consultants Bureau, New York, pp 205–311
- Brambles O, Lotko W, Zhang B, Ouellette J, Lyon J, Wiltberger M (2013) The effects of ionospheric outflow on icme and sir driven sawtooth events. *Journal of Geophysical Research: Space Physics* 118(10):6026–6041
- Buchner J, Zelenyi L (1989) Regular and chaotic charged-particle motion in magnetotail-like field reversals .1. basic theory of trapped motion. *Journal of Geophysical Research* 94(A9):11821–11842
- Büchner J, Dum C, Scholer M (2003) *Space plasma simulation*, vol 615. Springer Science & Business Media
- Bulanov SV, Pegoraro F, Sakharov AS (1992) Magnetic reconnection in electron magnetohydrodynamics. *Physics of Fluids B: Plasma Physics* 4(8):2499–2508, DOI 10.1063/1.860467
- Burch JL, Torbert RB, Phan TD, Chen LJ, Moore TE, Ergun RE, Eastwood JP, Gershman DJ, Cassak PA, Argal MR, Wang S, Hesse M, Pollock CJ, Giles BL, Nakamura R, Mauk BH, Fuselier SA, Russell CT, Strangeway RJ, Drake JF, Shay MA, Khotyaintsev YV, Lindqvist PA, Marklund G, Wilder FD, Young DT, Torkar K, Goldstein J, Dorelli JC, Avannov LA, Oka M, Baker DN, Jaynes AN, Goodrich KA, Cohen IJ, Turner DL, Fennell JF, Blake JB, Clemmons J, Goldman M, Newman D, Petrinec SM, Trattner K, Lavraud B, Reiff PH, Baumjohann W, Magnes

- W, Steller M, Lewis W, Saito Y, Coffey V, , Chandler M (2016) Electron-scale measurements of magnetic reconnection in space. *Science* 352(6290):aaf2939
- Burch JL, Webster JM, Hesse M, Genestreti KJ, Denton RE, Phan TD, Hasegawa H, Cassak PA, Torbert RB, Giles BL, Gershman DJ, Ergun RE, Russell CT, Strangeway RJ, Le Contel O, Pritchard KR, Marshall AT, Hwang KJ, Dokgo K, Fuselier SA, Chen LJ, Wang S, Swisdak M, Drake JF, Argall MR, Trattner KJ, Yamada M, Paschmann G (2020) Electron Inflow Velocities and Reconnection Rates at Earth's Magnetopause and Magnetosheath. *Geophysical Research Letters* 47(17):e2020GL089082, DOI 10.1029/2020GL089082
- Buzulukova N, Fok MC, Pulkkinen A, Kuznetsova M, Moore TE, Glocer A, Brandt PC, Tóth G, Rastatter L (2010) Dynamics of ring current and electric fields in the inner magnetosphere during disturbed periods: CRCM-BATS-R-US coupled model. *J Geophys Res* 115:A05210, DOI doi:10.1029/2009JA014621
- Califano F, Cerri SS (2022) Eulerian approach to solve the vlasov equation and hybrid-vlasov simulations. In: *Space and Astrophysical Plasma Simulation: Methods, Algorithms, and Applications*, Springer, pp 123–161
- Califano F, Attico N, Pegoraro F, Bertin G, Bulanov SV (2001) Fast formation of magnetic islands in a plasma in the presence of counterstreaming electrons. *Phys Rev Lett* 86:5293–5296, DOI 10.1103/PhysRevLett.86.5293, URL <https://link.aps.org/doi/10.1103/PhysRevLett.86.5293>
- Califano F, Cerri SS, Faganello M, Laveder D, Sisti M, Kunz MW (2020) Electron-only reconnection in plasma turbulence. *Frontiers in Physics* 8:317
- Caprioli D (2014) Hybrid Simulations of Particle Acceleration at Shocks. *Nuclear Physics B (Proc Suppl)* 256–257:48–55, DOI 10.1016/j.nuclphysbps.2014.10.005, URL <https://doi.org/10.1016/j.nuclphysbps.2014.10.005>
- Cassak PA, Shay MA (2007) Scaling of asymmetric magnetic reconnection: General theory and collisional simulations. *Phys Plasmas* 14:102114, DOI 10.1063/1.2795630
- Cassak PA, Shay MA (2012) Magnetic reconnection for coronal conditions: Reconnection rates, secondary islands and onset. *Space Sci Rev* 172:283
- Cassak PA, Shay MA, Drake JF (2005) Catastrophe model for fast magnetic reconnection onset. *Phys Rev Lett* 95:235002, DOI 10.1103/PhysRevLett.95.235002
- Cassak PA, Baylor RN, Fermo RL, Beidler MT, Shay MA, Swisdak M, Drake JF, Karimabadi H (2015) Fast magnetic reconnection due to anisotropic electron pressure. *Phys Plasmas* 22:020705
- Cassak PA, Barbhuiya MH, Liang H, Argall MR (2023) Quantifying Energy Conversion in Higher-Order Phase Space Density Moments in Plasmas. *Physical Review Letters* 130(8):085201, DOI 10.1103/PhysRevLett.130.085201, [2306.01106](https://doi.org/10.1103/PhysRevLett.130.085201)
- Cerri SS, Servidio S, Califano F (2017) Kinetic cascade in solar-wind turbulence: 3d3v hybrid-kinetic simulations with electron inertia. *The Astrophysical Journal Letters* 846(2):L18, DOI 10.3847/2041-8213/aa87b0, URL <https://dx.doi.org/10.3847/2041-8213/aa87b0>
- Cerri SS, Kunz MW, Califano F (2018) Dual Phase-space Cascades in 3D Hybrid-Vlasov-Maxwell Turbulence. *The Astrophysical Journal Letters* 856(1):L13, DOI 10.3847/2041-8213/aab557, [1802.06133](https://doi.org/10.3847/2041-8213/aab557)

- Chacón L, Simakov AN, Zocco A (2007) Steady-State Properties of Driven Magnetic Reconnection in 2D Electron Magnetohydrodynamics. *Physical Review Letters* 99(23):235001, DOI 10.1103/PhysRevLett.99.235001
- Chen LJ, Ng J, Omelchenko Y, Wang S (2021) Magnetopause reconnection and indents induced by foreshock turbulence. *Geophysical Research Letters* 48(11):e2021GL093029
- Chen MW, Schulz M (2001) Simulations of diffuse aurora with plasma sheet electrons in pitch angle diffusion less than everywhere strong. *Journal of Geophysical Research: Space Physics* 106(A12):28949–28966
- Chen MW, Lemon CL, Guild TB, Schulz M, Roeder JL, Le G (2012) Comparison of self-consistent simulations with observed magnetic field and ion plasma parameters in the ring current during the 10 august 2000 magnetic storm. *Journal of Geophysical Research: Space Physics* 117(A9)
- Chen Y, Tóth G (2019) Gauss’s law satisfying energy-conserving semi-implicit particle-in-cell method. *J Comput Phys* 386:632, DOI 10.1016/j.jcp.2019.02.032
- Chen Y, Tóth G, Cassak P, Jia X, Gombosi TI, Slavin J, Markidis S, Peng B (2017) Global three-dimensional simulation of earth’s dayside reconnection using a two-way coupled magnetohydrodynamics with embedded particle-in-cell model: initial results. *J Geophys Res* 122:10318, DOI 10.1002/2017JA024186
- Chen Y, Tóth G, Jia X, Slavin J, Sun W, Markidis S, Gombosi T, Raines J (2019) Studying dawn-dusk asymmetries of mercury’s magnetotail using mhd-epic simulations. *J Geophys Res* 124:8954, DOI 10.1029/2019JA026840
- Chen Y, Tóth G, Hietala H, Vines SK, Zou Y, Nishimura Y, Silveira MV, Guo Z, Lin Y, Markidis S (2020) Magnetohydrodynamic with embedded particle-in-cell simulation of the Geospace Environment Modeling dayside kinetic processes challenge event. *Earth and Space Science* DOI 10.1029/2020ea001331
- Chen Y, Tóth G, Zhou H, Wang X (2023) FLEKS: A flexible particle-in-cell code for multi-scale plasma simulations. *Computer Physics Communications* 287:108714, DOI 10.1016/j.cpc.2023.108714
- Cheng L, Lin Y, Perez J, Johnson JR, Wang X (2020) Kinetic alfvén waves from magnetotail to the ionosphere in global hybrid simulation associated with fast flows. *Journal of Geophysical Research: Space Physics* 125(2):e2019JA027062
- Chew GF, Goldberger ML, Low FE (1956) Boltzmann equation and the one-fluid hydrodynamic equations in the absence of particle collisions. *Proc Roy Soc A* 236:112
- Choudhuri AR (1998) *The Physics of Fluids and Plasmas*. Cambridge University Press
- Cramer WD, Raeder J, Toffoletto F, Gilson M, Hu B (2017) Plasma sheet injections into the inner magnetosphere: Two-way coupled openggcm-rcm model results. *Journal of Geophysical Research: Space Physics* 122(5):5077–5091
- Curran DB, Goertz C (1989) Particle distributions in a two-dimensional reconnection field geometry. *Journal of Geophysical Research: Space Physics* 94(A1):272–286
- Dahlin J, Drake J, Swisdak M (2015) Electron acceleration in three-dimensional magnetic reconnection with a guide field. *Physics of Plasmas* 22(10)
- Dahlin J, Drake J, Swisdak M (2016) Parallel electric fields are inefficient drivers of energetic electrons in magnetic reconnection. *Physics of Plasmas* 23(12)

- Dahlin J, Drake J, Swisdak M (2017) The role of three-dimensional transport in driving enhanced electron acceleration during magnetic reconnection. *Physics of Plasmas* 24(9)
- Dahlin JT, Drake JF, Swisdak M (2014) The mechanisms of electron heating and acceleration during magnetic reconnection. *Physics of Plasmas* 21(9):092304, DOI 10.1063/1.4894484, [1406.0831](https://doi.org/10.1063/1.4894484)
- Dahlin JT, Drake JF, Swisdak M (2015) Electron acceleration in three-dimensional magnetic reconnection with a guide field. *Physics of Plasmas* 22(10):100704, DOI 10.1063/1.4933212, [1503.02218](https://doi.org/10.1063/1.4933212)
- Daldorff LKS, Tóth G, Gombosi TI, Lapenta G, Amaya J, Markidis S, Brackbill JU (2014a) Two-way coupling of a global Hall magnetohydrodynamics model with a local implicit particle-in-cell model. *Journal of Computational Physics* 268:236–254
- Daldorff LKS, Tóth G, Gombosi TI, Lapenta G, Amaya J, Markidis S, Brackbill JU (2014b) Two-way coupling of a global Hall magnetohydrodynamics model with a local implicit Particle-in-Cell model. *J Comput Phys* 268:236, DOI 10.1016/j.jcp.2014.03.009
- Daughton W, JScudder (2006) Fully kinetic simulations of undriven magnetic reconnection with open boundary conditions. *Physics of Plasmas* 13:072101
- Daughton W, Scudder J, Karimabadi H (2006) Fully kinetic simulations of undriven magnetic reconnection with open boundary conditions. *Physic of Plasmas* 13(7):072101, DOI 10.1063/1.2218817
- Daughton W, Roytershteyn V, Albright BJ, Karimabadi H, Yin L, Bowers KJ (2009) Transition from collisional to kinetic regimes in large-scale reconnection layers. *Phys Rev Lett* 103:065004
- Daughton W, Roytershteyn V, Karimabadi H, Yin L, Albright BJ, Bergen B, Bowers KJ (2011) Role of electron physics in the development of turbulent magnetic reconnection in collisionless plasmas. *Nature Physics* 7:539–542, DOI 10.1038/nphys1965
- De Zeeuw D, Sazykin S, Wolf R, Gombosi T, Ridley A, Tóth G (2004) Coupling of a global MHD code and an inner magnetosphere model: Initial results. *J Geophys Res* 109(A12):219, DOI 10.1029/2003JA010366
- De Zeeuw DL, Sazykin S, Wolf RA, Gombosi TI, Ridley AJ, Tóth G (2004) Coupling of a global mhd code and an inner magnetospheric model: Initial results. *Journal of Geophysical Research: Space Physics* 109(A12)
- Delamere PA (2009) Hybrid code simulations of the solar wind interaction with Pluto. *Journal of Geophysical Research* 114:A03220, DOI 10.1029/2008JA013756, URL <https://doi.org/10.1029/2008JA013756>
- Delcourt D, Sauvaud J (1994) Plasma sheet ion energization during dipolarization events. *Journal of Geophysical Research: Space Physics* 99(A1):97–108
- Delzanno G (2015) Multi-dimensional, fully-implicit, spectral method for the vlasov–maxwell equations with exact conservation laws in discrete form. *Journal of Computational Physics* 301:338 – 356, DOI <https://doi.org/10.1016/j.jcp.2015.07.028>, URL <http://www.sciencedirect.com/science/article/pii/S0021999115004738>
- Dong C, Wang L, Hakim A, Bhattacharjee A, Slavin JA, DiBraccio GA, Germaschewski K (2019) Global ten-moment multifluid simulations of the solar wind

- interaction with mercury: From the planetary conducting core to the dynamic magnetosphere. *Geophysical Research Letters* 46(21):11584–11596
- Dong C, Le A, Wang L, Stanier A, Wetherton B, Daughton W, Bhattacharjee A, Slavin J, DiBraccio G (2021) Global Hybrid-VPIC Simulations of the Solar Wind Interaction with Mercury’s Dynamic Magnetosphere: Reconnection and Fore-shock. In: EGU General Assembly, 19–30 Apr 2021, vol EGU-12954, DOI 10.5194/egusphere-egu21-12954, URL <https://doi.org/10.5194/egusphere-egu21-12954>
- Dorelli J, Birn J (2003) Whistler-mediated magnetic reconnection in large systems: Magnetic flux pileup and the formation of thin current sheets. *J Geophys Res Space Physics* 108(A3):1133, DOI 10.1029/2001JA009180, URL <https://doi.org/10.1029/2001JA009180>
- Dorelli JC, Glocer A, Collinson G, Tóth G (2015) The role of the hall effect in the global structure and dynamics of planetary magnetospheres: Ganymede as a case study. *J Geophys Res* 120:5377
- Drake J, Swisdak M, Che H, Shay M (2006) Electron acceleration from contracting magnetic islands during reconnection. *Nature* 443(7111):553–556
- Drake J, Arnold H, Swisdak M, Dahlin J (2019) A computational model for exploring particle acceleration during reconnection in macroscale systems. *Physics of Plasmas* 26(1)
- Drake JF, Shay MA (2007) The fundamentals of collisionless reconnection. In: Birn J, Priest E (eds) *Reconnection of Magnetic Fields: Magnetohydrodynamics and Collisionless Theory and Observations*, Cambridge University Press
- Drake JF, Kleva RG, Mandt ME (1994) Structure of Thin Current Layers: Implications for Magnetic Reconnection. *Physical Review Letters* 73(9):1251–1254, DOI 10.1103/PhysRevLett.73.1251
- Drake JF, Biskamp D, Zeiler A (1997) Breakup of the electron current layer during 3-D collisionless magnetic reconnection. *Geophysical Research Letters* 24(22):2921–2924, DOI 10.1029/97GL52961
- Drake JF, Swisdak M, Che H, Shay MA (2006) Electron acceleration from contracting magnetic islands during reconnection. *Nature* 443(7111):553–556, DOI 10.1038/nature05116
- Drake JF, Shay MA, Swisdak M (2008) The Hall fields and fast magnetic reconnection. *Physics of Plasmas* 15(4):042306, DOI 10.1063/1.2901194
- Dreher J, Arendt U, Schindler K (1996) Particle simulations of collisionless reconnection in magnetotail configuration including electron dynamics. *Journal of Geophysical Research: Space Physics* 101(A12):27375–27381
- Du S, Guo F, Zank GP, Li X, Stanier A (2018) Plasma Energization in Colliding Magnetic Flux Ropes. *Astrophysical Journal* 867(1):16, DOI 10.3847/1538-4357/aae30e, [1809.08357](https://doi.org/10.3847/1538-4357/aae30e)
- Dungey J (1961) Interplanetary magnetic field and the auroral zones. *Phys Rev Lett* 93:47, DOI 10.1103/PhysRevLett.6.47
- Dungey JW (1954) The attenuation of alfvén waves. *Journal of Geophysical Research (1896-1977)* 59(3):323–328, DOI <https://doi.org/10.1029/JZ059i003p00323>

- Dyadechkin S, Kallio E, Jarvinen R (2013) A new 3-D spherical hybrid model for solar wind interaction studies. *Journal of Geophysical Research: Space Physics* 118:5157–5168, DOI 10.1002/jgra.50497, URL <https://doi.org/10.1002/jgra.50497>
- Edwards AW, Campbell DJ, Engelhardt WW, Farhbach HU, Gill RD, Granetz RS, Tsuji S, Tubbing BJD, Weller A, Wesson J, Zasche D (1986) Rapid collapse of a plasma sawtooth oscillation in the jet tokamak. *Phys Rev Lett* 57:210–213
- Egedal J, Daughton W, Le A (2012) Large-scale electron acceleration by parallel electric fields during magnetic reconnection. *Nature Physics* 8(4):321–324
- Egedal J, Le A, Daughton W (2013) A review of pressure anisotropy caused by electron trapping in collisionless plasma, and its implications for magnetic reconnection. *Phys Plasmas* 20:061201
- Erickson GM, Wolf R (1980) Is steady convection possible in the earth’s magnetotail? *Geophysical Research Letters* 7(11):897–900
- Eriksson S, Wilder FD, Ergun RE, Schwartz SJ, Cassak PA, Burch JL, Chen LJ, Torbert RB, Phan TD, Lavraud B, Goodrich KA, Holmes JC, Stawarz JE, Sturmer AP, Malaspina DM, Usanova ME, Trattner KJ, Strangeway RJ, Russell CT, Pollock CJ, Giles BL, Hesse M, Lindqvist PA, Drake JF, Shay MA, Nakamura R, Marklund GT (2016) Magnetospheric Multiscale Observations of the Electron Diffusion Region of Large Guide Field Magnetic Reconnection. *Physical Review Letters* 117(1):015001, DOI 10.1103/PhysRevLett.117.015001
- Fadanelli S, Lavraud B, Califano F, Cozzani G, Finelli F, Sisti M (2021) Energy conversions associated with magnetic reconnection. *Journal of Geophysical Research: Space Physics* 126(1):e2020JA028333, DOI <https://doi.org/10.1029/2020JA028333>, e2020JA028333 2020JA028333, <https://agupubs.onlinelibrary.wiley.com/doi/pdf/10.1029/2020JA028333>
- Farrugia CJ, Rogers AJ, Torbert RB, Genestreti KJ, Nakamura TKM, Lavraud B, Montag P, Egedal J, Payne D, Keesee A, Ahmadi N, Ergun R, Reiff P, Argall M, Matsui H, Wilson III LB, Lugaz N, Burch JL, Russell CT, Fuselier SA, Dors I (2021) An Encounter With the Ion and Electron Diffusion Regions at a Flapping and Twisted Tail Current Sheet. *Journal of Geophysical Research: Space Physics* 126(3):e2020JA028903, DOI 10.1029/2020JA028903
- Fatemi S, Poppe AR, Delory GT, Farrell WM (2017) AMITIS: A 3D GPU-Based Hybrid-PIC Model for Space and Plasma Physics. *J Phys: Conf Ser* 837:012017, DOI 10.1088/1742-6596/837/1/012017, URL <https://iopscience.iop.org/article/10.1088/1742-6596/837/1/012017>
- Finelli F (2022) Magnetic reconnection in space plasmas: advanced numerical models and detection in turbulence. Phd thesis, University of Pisa, Pisa, Italy, URL <https://etd.adm.unipi.it/t/etd-06062022-180752/>
- Finelli F, Cerri SS, Califano F, Pucci F, Laveder D, Lapenta G, Passot T (2021) Bridging hybrid- and full-kinetic models with landau-fluid electrons. *Astronomy & Astrophysics* 653:A156, DOI 10.1051/0004-6361/202140279
- Fok MC, Wolf R, Spiro R, Moore T (2001) Comprehensive computational model of earth’s ring current. *Journal of Geophysical Research: Space Physics* 106(A5):8417–8424

- Fok MC, Buzulukova N, Chen SH, Glocer A, Nagai T, Valek P, Perez J (2014) The comprehensive inner magnetosphere-ionosphere model. *Journal of Geophysical Research: Space Physics* 119(9):7522–7540
- Fox W, Bhattacharjee A, Germaschewski K (2012) Magnetic reconnection in high-energy-density laser-produced plasmas. *Physics of Plasmas* 19(5)
- Franci L, Cerri SS, Califano F, Landi S, Papini E, Verdini A, Matteini L, Jenko F, Hellinger P (2017) Magnetic reconnection as a driver for a sub-ion-scale cascade in plasma turbulence. *The Astrophysical Journal Letters* 850(1):L16, DOI 10.3847/2041-8213/aa93fb, URL <https://dx.doi.org/10.3847/2041-8213/aa93fb>
- Franci L, Hellinger P, Guarrasi M, Chen CH, Papini E, Verdini A, Matteini L, Landi S (2018) Three-dimensional simulations of solar wind turbulence with the hybrid code CAMELIA. *Journal of Physics: Conference Series* 1031(1), DOI 10.1088/1742-6596/1031/1/012002
- Freeman J, Wolf R, Spiro R, Hausman B, Bales B, Hilmer R, Nagai A, Lambour R (1993) Magnetospheric specification model development code documentation, scientific description, and software documentation. contract F19628-90-K-0012, Rice Univ for Air Force Geophys Lab, Hanscom Air Force Base, Mass, July
- French O, Guo F, Zhang Q, Uzdensky D (2022) Particle Injection and Nonthermal Particle Acceleration in Relativistic Magnetic Reconnection. arXiv e-prints arXiv:2210.08358, [2210.08358](https://arxiv.org/abs/2210.08358)
- Fu XR, Lu QM, Wang S (2006) The process of electron acceleration during collisionless magnetic reconnection. *Physics of Plasmas* 13(1):012309, DOI 10.1063/1.2164808
- Fuller-Rowell T, Rees D, Quegan S, Moffett R, Codrescu M, Millward G (1996) A coupled thermosphere-ionosphere model (ctim). STEP report 239(4)
- Gabrielse C, Angelopoulos V, Runov A, Turner D (2012) The effects of transient, localized electric fields on equatorial electron acceleration and transport toward the inner magnetosphere. *Journal of Geophysical Research: Space Physics* 117(A10)
- Gallagher DL, Craven PD, Comfort RH (2000) Global core plasma model. *Journal of Geophysical Research: Space Physics* 105(A8):18819–18833
- Ganse U, Koskela T, Battarbee M, Pfau-Kempf Y, Papadakis K, Alho M, Bussov M, Cozzani G, Dubart M, George H, Gordeev E, Grandin M, Horaites K, Suni J, Tarpus V, Kebede FT, Turc L, Zhou H, Palmroth M (2023) Enabling technology for global 3D + 3V hybrid-vlasov simulations of near-earth space. *Physics of Plasmas* 30(4):042902
- Ghizzo A, Sarrat M, Del Sarto D (2017) Vlasov models for kinetic Weibel-type instabilities. *Journal of Plasma Physics* 83(1):705830101, DOI 10.1017/S0022377816001215
- Gingell I, Schwartz SJ, Eastwood JP, Burch JL, Ergun RE, Fuselier S, Gershman DJ, Giles BL, Khotyaintsev YV, Lavraud B, Lindqvist PA, Paterson WR, Phan TD, Russell CT, Stawarz JE, Strangeway RJ, Torbert RB, Wilder F (2019) Observations of Magnetic Reconnection in the Transition Region of Quasi-Parallel Shocks. *Geophysical Research Letters* 46(3):1177–1184, DOI 10.1029/2018GL081804
- Gingell I, Schwartz SJ, Eastwood JP, Stawarz J, Burch JL, Ergun RE, Fuselier SA, Gershman DJ, Giles BL, Khotyaintsev YV, Lavraud B, Lindqvist PA, Paterson WR, Phan TD, Russell CT, Strangeway RJ, Torbert RB, Wilder F (2020) Statistics

- of reconnecting current sheets in the transition region of earth's bow shock. *Journal of Geophysical Research* 125:e2019JA027119
- Gingell I, Schwartz SJ, HKucharek, Farrugia CJ, JTrattner K (2021) Observing the prevalence of thin current sheets downstream of earth's bow shock. *Physics of Plasmas* 28:102902
- Gkioulidou M, Ukhorskiy A, Mitchell D, Sotirelis T, Mauk B, Lanzerotti L (2014) The role of small-scale ion injections in the buildup of earth's ring current pressure: Van allen probes observations of the 17 march 2013 storm. *Journal of Geophysical Research: Space Physics* 119(9):7327–7342
- Glasser AH, Sovinec CR, Nebel RA, Gianakon TA, Plimpton SJ, Chu MS, Schnack DD, the NIMROD Team (1999) The nimrod code: a new approach to numerical plasma physics. *Plasma Physics and Controlled Fusion* 41(3A):A747, DOI 10.1088/0741-3335/41/3A/067, URL <https://dx.doi.org/10.1088/0741-3335/41/3A/067>
- Glocer A, Tóth G, Gombosi T, Welling D (2009a) Modeling ionospheric outflows and their impact on the magnetosphere, initial results. *Journal of Geophysical Research: Space Physics* 114(A5)
- Glocer A, Tóth G, Ma YJ, Gombosi T, Zhang JC, Kistler LM (2009b) Multifluid Block-Adaptive-Tree Solar wind Roe-type Upwind Scheme: Magnetospheric composition and dynamics during geomagnetic storms – initial results. *J Geophys Res* 114:A12203, DOI 10.1029/2009JA014418
- Glocer A, Fok M, Meng X, Toth G, Buzulukova N, Chen S, Lin K (2013) Crcm+bats-r-us two-way coupling. *Journal of Geophysical Research: Space Physics* 118(4):1635–1650
- Godfrey BB (1980) Time-biased field solver for electromagnetic pic code. *Proceedings of the Ninth Conference on Numerical Simulation of Plasmas* p OD–4
- Goldstein J, Spiro RW, Reiff PH, Wolf RA, Sandel BR, Freeman JW, Lambour RL (2002) IMF-driven overshielding electric field and the origin of the plasmaspheric shoulder of May 24, 2000. *Geophysical Research Letters* 29(16):1819, DOI 10.1029/2001GL014534
- Gomez D (2006) Parallel simulations of hall-mhd plasmas. *Space Sci Rev* 122:231–238
- Gonzalez W, Parker E (eds) (2016) *Magnetic Reconnection, Astrophysics and Space Science Library*, vol 427. Springer International Publishing, Cham, DOI 10.1007/978-3-319-26432-5, URL <http://link.springer.com/10.1007/978-3-319-26432-5>
- Gordeev AV, Kingsep AS, Rudakov LI (1994) Electron magnetohydrodynamics. *Physics Reports* 243(5):215–315, DOI 10.1016/0370-1573(94)90097-3
- Grandin M, Turc L, Battarbee M, Ganse U, Johlander A, Pfau-Kempf Y, Dubart M, Palmroth M (2020) Hybrid-vlasov simulation of auroral proton precipitation in the cusps: Comparison of northward and southward interplanetary magnetic field driving. *J Space Weather Space Clim* 10:51, DOI 10.1051/swsc/2020053, URL <https://doi.org/10.1051/swsc/2020053>
- Grandin M, Luttikhuis T, Battarbee M, Cozzani G, Zhou H, Turc L, Pfau-Kempf Y, George H, Horaites K, Gordeev E, Ganse U, Papadakis K, Alho M, Tesema F, Suni J, Dubart M, Tarvus V, Palmroth M (2023) First 3d hybrid-vlasov global simulation of auroral proton precipitation and comparison with satellite observations. *Journal of Space Weather and Space Climate* p TBD, DOI 10.1051/swsc/2023017

- Greco A, Valentini F, Servidio S, Matthaeus WH (2012) Inhomogeneous kinetic effects related to intermittent magnetic discontinuities. *Physical Review E* 86(6):066405, DOI 10.1103/PhysRevE.86.066405
- Greess S, Egedal J, Stanier A, Daughton W, Olson J, Lê A, Myers R, Millet-Ayala A, Clark M, Wallace J, Endrizzi D, Forest C (2021) Laboratory Verification of Electron-Scale Reconnection Regions Modulated by a Three-Dimensional Instability. *Journal of Geophysical Research: Space Physics* 126(7):e2021JA029316, DOI 10.1029/2021JA029316
- Guo F, Giacalone J (2013) THE ACCELERATION OF THERMAL PROTONS AT PARALLEL COLLISIONLESS SHOCKS: THREE-DIMENSIONAL HYBRID SIMULATIONS. *The Astrophysical Journal* 773:158, DOI 10.1088/0004-637X/773/2/158, URL <https://doi.org/10.1088/0004-637X/773/2/158>
- Guo F, Li H, Daughton W, Liu YH (2014) Formation of Hard Power Laws in the Energetic Particle Spectra Resulting from Relativistic Magnetic Reconnection. *Physical Review Letters* 113(15):155005, DOI 10.1103/PhysRevLett.113.155005, [1405.4040](https://doi.org/10.1103/PhysRevLett.113.155005)
- Guo F, Liu YH, Daughton W, Li H (2015) Particle Acceleration and Plasma Dynamics during Magnetic Reconnection in the Magnetically Dominated Regime. *Astrophysical Journal* 806(2):167, DOI 10.1088/0004-637X/806/2/167, [1504.02193](https://doi.org/10.1088/0004-637X/806/2/167)
- Guo F, Li X, Daughton W, Kilian P, Li H, Liu YH, Yan W, Ma D (2019) Determining the Dominant Acceleration Mechanism during Relativistic Magnetic Reconnection in Large-scale Systems. *Astrophysical Journal Letters* 879(2):L23, DOI 10.3847/2041-8213/ab2a15, [1901.08308](https://doi.org/10.3847/2041-8213/ab2a15)
- Guo F, Li X, Daughton W, Li H, Kilian P, Liu YH, Zhang Q, Zhang H (2021) Magnetic Energy Release, Plasma Dynamics, and Particle Acceleration in Relativistic Turbulent Magnetic Reconnection. *Astrophysical Journal* 919(2):111, DOI 10.3847/1538-4357/ac0918, [2008.02743](https://doi.org/10.3847/1538-4357/ac0918)
- Guo F, Liu YH, Zenitani S, Hoshino M (2023) Magnetic Reconnection and Associated Particle Acceleration in High-energy Astrophysics. arXiv e-prints arXiv:2309.13382, DOI 10.48550/arXiv.2309.13382, [2309.13382](https://arxiv.org/abs/2309.13382)
- Guo J, Lu S, Lu Q, Lin Y, Wang X, Huang K, Wang R, Wang S (2021a) Reconnection processes of magnetopause flux ropes: Three-dimensional global hybrid simulations. *Journal of Geophysical Research: Space Physics* 126(6):e2021JA029388
- Guo J, Lu S, Lu Q, Lin Y, Wang X, Zhang Q, Xing Z, Huang K, Wang R, Wang S (2021b) Three-dimensional global hybrid simulations of high latitude magnetopause reconnection and flux ropes during the northward IMF. *Geophysical Research Letters* 48(21):e2021GL095003
- Guo Z, Lin Y, Wang X, Vines SK, Lee S, Chen Y (2020) Magnetopause reconnection as influenced by the dipole tilt under southward IMF conditions: Hybrid simulation and MMS observation. *Journal of Geophysical Research: Space Physics* 125(9):e2020JA027795
- Guo Z, Lin Y, Wang X (2021c) Investigation of the Interaction between Magnetosheath Reconnection and Magnetopause Reconnection Driven by Oblique Interplanetary Tangential Discontinuity Using Three-Dimensional Global Hybrid Simulation. *J Geophys Res Space Physics* 126:e2020JA028558, DOI 10.1029/2020JA028558, URL <https://doi.org/10.1029/2020JA028558>

- Guo Z, Lin Y, Wang X, Du A (2021d) Magnetic reconnection inside solar wind rotational discontinuity during its interaction with the quasi-perpendicular bow shock and magnetosheath. *Journal of Geophysical Research: Space Physics* 126(12):e2021JA029979
- Haggerty CC, Parashar TN, Matthaeus WH, Shay MA, Yang Y, Wan M, Wu P, Servidio S (2017) Exploring the statistics of magnetic reconnection x-points in kinetic particle-in-cell turbulence. *Phys Plasmas* 24:102308
- Haiducek JD, Welling DT, Morley SK, Gañushkina NY, Chu X (2020) Using multiple signatures to improve accuracy of substorm identification. *J Geophys Res* 125(4):e2019JA027559, DOI <https://doi.org/10.1029/2019JA027559>, URL <https://agupubs.onlinelibrary.wiley.com/doi/abs/10.1029/2019JA027559>
- Hall EH, et al. (1879) On a new action of the magnet on electric currents. *American Journal of Mathematics* 2(3):287–292
- Harris EG (1962a) The equilibrium of oppositely directed magnetic fields. *Nuovo Cimento* 23:115–121
- Harris EG (1962b) On a plasma sheath separating regions of oppositely directed magnetic field. *Il Nuovo Cimento (1955-1965)* 23(1):115–121
- Herčík D, Trávníček PM, Johnson R, Kim EH, Hellinger P (2013) Mirror mode structures in the asymmetric Hermean magnetosheath: Hybrid simulations. *Journal of Geophysical Research: Space Physics* 118:405–417, DOI 10.1029/2012JA018083, URL <https://doi.org/10.1029/2012JA018083>
- Hesse M, Winske D (1998) Electron dissipation in collisionless magnetic reconnection. *Journal of Geophysical Research: Space Physics* 103(A11):26479–26486, DOI 10.1029/98JA01570
- Hesse M, Birn J, Baker DN, Slavin JA (1996) Mhd simulations of the transition of magnetic reconnection from closed to open field lines. *Journal of Geophysical Research: Space Physics* 101(A5):10805–10816, DOI <https://doi.org/10.1029/95JA02857>, URL <https://agupubs.onlinelibrary.wiley.com/doi/abs/10.1029/95JA02857>, <https://agupubs.onlinelibrary.wiley.com/doi/pdf/10.1029/95JA02857>
- Hesse M, Liu YH, Chen LJ, Bessho N, Kuznetsova M, Birn J, Burch JL (2016) On the electron diffusion region in asymmetric reconnection with a guide magnetic field. *Geophysical Research Letters* 43(6):2359–2364, DOI 10.1002/2016GL068373
- Hesse M, Norgren C, Tenfjord P, Burch JL, Liu YH, Chen LJ, Bessho N, Wang S, Nakamura R, Eastwood JP, Hoshino M, Torbert RB, Ergun RE (2018a) On the role of separatrix instabilities in heating the reconnection outflow region. *Physics of Plasmas* 25:122902
- Hesse M, Liu YH, Chen LJ, Bessho N, Wang S, Burch J, Moretto T, Norgren C, Genestreti K, Phan T, et al. (2018b) The physical foundation of the reconnection electric field. *Physics of Plasmas* 25(3)
- Hesse M, Norgren C, Tenfjord P, Burch JL, Liu YH, Chen LJ, Bessho N, Wang S, Nakamura R, Eastwood JP, Hoshino M, Torbert RB, Ergun RE (2019) Erratum: “on the role of separatrix instabilities in heating the reconnection outflow region”. *Physics of Plasmas* 26:049901
- Hill T, Rymer A, Burch J, Crary F, Young D, Thomsen M, Delapp D, André N, Coates A, Lewis G (2005) Evidence for rotationally driven plasma transport in saturn’s

- magnetosphere. *Geophysical Research Letters* 32(14)
- Hilmer RV, Voigt GH (1995) A magnetospheric magnetic field model with flexible current systems driven by independent physical parameters. *Journal of Geophysical Research: Space Physics* 100(A4):5613–5626
- Hoilijoki S, Ganse U, Pfau-Kempf Y, Cassak PA, Walsh BM, Hietala H, von Althaus S, Palmroth M (2017) Reconnection rates and x line motion at the magnetopause: Global 2d-3v hybrid-vlasov simulation results. *Journal of Geophysical Research: Space Physics* 122(3):2877–2888, DOI <https://doi.org/10.1002/2016JA023709>, URL <https://agupubs.onlinelibrary.wiley.com/doi/abs/10.1002/2016JA023709>, <https://agupubs.onlinelibrary.wiley.com/doi/pdf/10.1002/2016JA023709>
- Hoilijoki S, Ganse U, Sibeck DG, Cassak PA, Turc L, Battarbee M, Fear RC, Blanco-Cano X, Dimmock AP, Kilpua EKJ, Jarvinen R, Juusola L, Pfau-Kempf Y, Palmroth M (2019) Properties of magnetic reconnection and ftes on the day-side magnetopause with and without positive imf bx component during southward imf. *Journal of Geophysical Research: Space Physics* 124(6):4037–4048, DOI <https://doi.org/10.1029/2019JA026821>, URL <https://agupubs.onlinelibrary.wiley.com/doi/abs/10.1029/2019JA026821>, <https://agupubs.onlinelibrary.wiley.com/doi/pdf/10.1029/2019JA026821>
- Holloway JP, Dornring JJ (1991) Undamped plasma waves. *Physical Review A* 44(6):3856–3868, DOI 10.1103/PhysRevA.44.3856
- Honkonen I, von Althaus S, Sandroos A, Janhunen P, Palmroth M (2013) Parallel grid library for rapid and flexible simulation development. *Computer Physics Communications* 184(4):1297–1309, DOI 10.1016/j.cpc.2012.12.017
- Horiuchi R, Sato T (1994) Particle simulation study of driven magnetic reconnection in a collisionless plasma. *Physics of Plasmas* 1(11):3587–3597
- Hoshino M (1987) The electrostatic effect for the collisionless tearing mode. *Journal of Geophysical Research: Space Physics* 1:7368–7380
- Hoshino M, Mukai T, Terasawa T, Shinohara I (2001) Suprathermal electron acceleration in magnetic reconnection. *Journal of Geophysical Research* 106(A11):25979–25998, DOI 10.1029/2001JA900052
- Hsieh MS, Otto A (2014) The influence of magnetic flux depletion on the magnetotail and auroral morphology during the substorm growth phase. *Journal of Geophysical Research: Space Physics* 119(5):3430–3443
- Hsieh MS, Otto A (2015) Thin current sheet formation in response to the loading and the depletion of magnetic flux during the substorm growth phase. *Journal of Geophysical Research: Space Physics* 120(6):4264–4278
- Hu B, Toffoletto F, Wolf R, Sazykin S, Raeder J, Larson D, Vapirev A (2010) One-way coupled opengcm/rcm simulation of the 23 march 2007 substorm event. *Journal of Geophysical Research: Space Physics* 115(A12)
- Hu B, Wolf R, Toffoletto F, Yang J, Raeder J (2011) Consequences of violation of frozen-in-flux: Evidence from opengcm simulations. *Journal of Geophysical Research: Space Physics* 116(A6)
- Huang K, Liu YH, Lu Q, Hesse M (2020) Scaling of magnetic reconnection with a limited x-line extent. *Geophysical Research Letters* 47:e2020GL088147

- Huang YM, Bhattacharjee A, Sullivan BP (2011) Onset of fast reconnection in Hall magnetohydrodynamics mediated by the plasmoid instability. *Phys Plasmas* 18:072109
- Huang Z, Tóth G, van der Holst B, Chen Y, Gombosi T (2019) A six-moment multi-fluid plasma model. *J Comput Phys* 387:134, DOI 10.1016/j.jcp.2019.02.023
- Huba JD (1995) Hall magnetohydrodynamics in space and laboratory plasmas. *Phys Plasmas* 2(6):2504–2513
- Huba JD (1998) NRL plasma formulary. 98-358, Naval Research Laboratory
- Huba JD (2003) A tutorial on Hall magnetohydrodynamics. In: Büchner J, Dum CT, Scholer M (eds) *Space Plasma Simulation*, Springer, New York, p 170
- Huba JD, Rudakov LI (2002) Three-dimensional Hall magnetic reconnection. *Phys Plasmas* 9:4435
- Huba JD, Rudakov LI (2003) Hall magnetohydrodynamics of neutral layers. *Phys Plasmas* 10:3139
- Huba JD, Sazykin S (2014) Storm time ionosphere and plasmasphere structuring: SAMI3-RCM simulation of the 31 March 2001 geomagnetic storm. *Geophysical Research Letters* 41(23):8208–8214, DOI 10.1002/2014GL062110
- Hubbert M, Russell CT, Qi Y, Lu S, Burch JL, Giles BL, Moore TE (2022) Electron-Only Reconnection as a Transition Phase From Quiet Magnetotail Current Sheets to Traditional Magnetotail Reconnection. *Journal of Geophysical Research: Space Physics* 127(3):e2021JA029584, DOI 10.1029/2021JA029584
- Hwang KJ, Choi E, Dokgo K, Burch JL, Sibeck DG, Giles BL, Goldstein ML, Paterson WR, Pollock CJ, Shi QQ, Fu H, Hasegawa H, Gershman DJ, Khotyaintsev Y, Torbert RB, Ergun RE, Dorelli JC, Avakov L, Russell CT, Strangeway RJ (2019) Electron Vorticity Indicative of the Electron Diffusion Region of Magnetic Reconnection. *Geophysical Research Letters* 46(12):6287–6296, DOI 10.1029/2019GL082710
- Hyman JM (1983) Accurate monotonicity preserving cubic interpolation. *SIAM Journal on Scientific and Statistical Computing* 4(4):645–654
- Inglebert A, Ghizzo A, Reveille T, Sarto DD, Bertrand P, Califano F (2011) A multi-stream vlasov modeling unifying relativistic weibel-type instabilities. *Europhysics Letters* 95(4):45002, DOI 10.1209/0295-5075/95/45002
- Jain N, Büchner J (2014a) Nonlinear evolution of three-dimensional instabilities of thin and thick electron scale current sheets: Plasmoid formation and current filamentation. *Physics of Plasmas* 21(7):072306, DOI 10.1063/1.4887279
- Jain N, Büchner J (2014b) Three dimensional instabilities of an electron scale current sheet in collisionless magnetic reconnection. *Physics of Plasmas* 21(6):062116, DOI 10.1063/1.4885636
- Jain N, Büchner J (2015) Effect of guide field on three-dimensional electron shear flow instabilities in electron current sheets. *Journal of Plasma Physics* 81(6):905810606, DOI 10.1017/S0022377815001257
- Jain N, Sharma AS (2009) Electron scale structures in collisionless magnetic reconnection. *Physics of Plasmas* 16(5):050704, DOI 10.1063/1.3134045

- Jain N, Sharma AS (2015a) Electron-scale nested quadrupole Hall field in Cluster observations of magnetic reconnection. *Annales Geophysicae* 33(6):719–724, DOI 10.5194/angeo-33-719-2015
- Jain N, Sharma AS (2015b) Evolution of electron current sheets in collisionless magnetic reconnection. *Physics of Plasmas* 22(10):102110, DOI 10.1063/1.4933120
- Jain N, Sharma AS, Zelenyi LM, Malova HV (2012) Electron scale structures of thin current sheets in magnetic reconnection. *Annales Geophysicae* 30(4):661–666, DOI 10.5194/angeo-30-661-2012
- Jain N, Büchner J, Dorfman S, Ji H, Surjalal Sharma A (2013) Current disruption and its spreading in collisionless magnetic reconnection. *Physics of Plasmas* 20(11)
- Jain N, Büchner J, Muñoz PA (2017a) Nonlinear evolution of electron shear flow instabilities in the presence of an external guide magnetic field. *Physics of Plasmas* 24(3):032303, DOI 10.1063/1.4977528
- Jain N, von Stechow A, Muñoz PA, Büchner J, Grulke O, Klinger T (2017b) Electron-magnetohydrodynamic simulations of electron scale current sheet dynamics in the Vineta.II guide field reconnection experiment. *Physics of Plasmas* 24(9):092312, DOI 10.1063/1.5004564
- Jain N, Muñoz PA, Farzalipour Tabriz M, Rampp M, Büchner J (2022) Importance of accurate consideration of the electron inertia in hybrid-kinetic simulations of collisionless plasma turbulence: The 2D limit. *Physics of Plasmas* 29(5):053902, DOI 10.1063/5.0087103
- Jain N, Muñoz PA, Büchner J (2023) Hybrid-kinetic approach: Inertial electrons. In: Büchner J (ed) *Space and Astrophysical Plasma Simulation: Methods, Algorithms, and Applications*, Springer International Publishing, pp 283–311
- Jardin S, Ferraro N, Luo X, Chen J, Breslau J, Jansen K, Shephard M (2008) The m3d-c1 approach to simulating 3d 2-fluid magnetohydrodynamics in magnetic fusion experiments. In: *Journal of Physics: Conference Series*, IOP Publishing, vol 125, p 012044
- Jarvinen R, Alho M, Kallio E, Pulkkinen TI (2020) Ultra-low-frequency waves in the foreshock of Mercury: a global hybrid modelling study. *MNRAS* 491:4147–4161, DOI 10.1093/mnras/stz3257, URL <https://doi.org/10.1093/mnras/stz3257>
- Johlander A, Battarbee M, Turc L, Gause U, Pfau-Kempf Y, Grandin M, Suni J, Tarvus V, Bussov M, Zhou H, Alho M, Dubart M, George H, Papadakis K, Palmroth M (2022) Quasi-parallel shock reformation seen by magnetospheric multiscale and ion-kinetic simulations. *Geophysical Research Letters* 49(2):e2021GL096335, DOI <https://doi.org/10.1029/2021GL096335>, e2021GL096335 2021GL096335, <https://agupubs.onlinelibrary.wiley.com/doi/pdf/10.1029/2021GL096335>
- Jordanova VK, Kozyra JU, Khazanov GV, Nagy AF, Rasmussen CE, Fok MC (1994) A bounce-averaged kinetic model of the ring current ion population. *Geophys Res Lett* 21:2785
- Juno J, Hakim A, TenBarge J, Shi E, Dorland W (2018) Discontinuous galerkin algorithms for fully kinetic plasmas. *Journal of Computational Physics* 353:110 – 147, DOI <https://doi.org/10.1016/j.jcp.2017.10.009>, URL <http://www.sciencedirect.com/science/article/pii/S0021999117307477>

- Juusola L, Hoilijoki S, Pfau-Kempf Y, Ganse U, Jarvinen R, Battarbee M, Kilpua E, Turc L, Palmroth M (2018) Fast plasma sheet flows and x line motion in the earth's magnetotail: results from a global hybrid-vlasov simulation. *Annales Geophysicae* 36(5):1183–1199, DOI 10.5194/angeo-36-1183-2018, URL <https://angeo.copernicus.org/articles/36/1183/2018/>
- Kallio E, Dyadechkin S, Wurz P, Khodachenko M (2019) Space weathering on the Moon: Farside-nearside solar wind precipitation asymmetry. *Planet Space Science* 166:9–22, DOI 10.1016/j.pss.2018.07.013, URL <https://doi.org/10.1016/j.pss.2018.07.013>
- Karimabadi H, Krauss-Varban D, Huba D, Vu H (2004a) On magnetic reconnection regimes and associated three-dimensional asymmetries: Hybrid, Hall-less hybrid, and Hall-MHD simulations. *Journal of Geophysical Research* 109(A9):A09205, DOI 10.1029/2004JA010478, URL <http://doi.wiley.com/10.1029/2004JA010478>
- Karimabadi H, Krauss-Varban D, Huba JD, Vu HX (2004b) On magnetic reconnection regimes and associated three-dimensional asymmetries: Hybrid, Hall-less hybrid, and Hall-MHD simulations. *J Geophys Res* 109:A09205
- Karimabadi H, Daughton W, Scudder J (2007) Multi-scale structure of the electron diffusion region. *Geophys Res Lett* 34:L13104
- Karimabadi H, Roytershteyn V, Vu HX, Omelchenko YA, Scudder J, Daughton W, Dimmock A, Nykyri K, Wan M, Sibeck D, Tatineni M, Majumdar A, Loring B, Geveci B (2014) The link between shocks, turbulence, and magnetic reconnection in collisionless plasmas. *Physics of Plasmas* 21(6):062308, DOI 10.1063/1.4882875
- Kepko L, McPherron R, Amm O, Apatenkov S, Baumjohann W, Birn J, Lester M, Nakamura R, Pulkkinen TI, Sergeev V (2015) Substorm current wedge revisited. *Space Science Reviews* 190:1–46
- Kilian P, Li X, Guo F, Li H (2020) Exploring the Acceleration Mechanisms for Particle Injection and Power-law Formation during Transrelativistic Magnetic Reconnection. *Astrophysical Journal* 899(2):151, DOI 10.3847/1538-4357/aba1e9, [2001.02732](https://doi.org/10.3847/1538-4357/aba1e9)
- Kingsep AS, Chukbar KV, Yan'kov YY (1990) Electron magnetohydrodynamics. In: *Reviews of Plasma Physics*, Consultants Bureau, New York, vol 16
- Kleva R, Drake J, Waelbroeck F (1995) Fast reconnection in high temperature plasma. *Phys Plasma* 2:23
- Kuznetsova M (2000) Toward a transport model of collisionless magnetic reconnection. *Journal of Geophysical Research: Space Physics* 105(A4):7601–7616, DOI 10.1029/1999JA900396
- Kuznetsova M, Hesse M, Winske D (1998) Kinetic quasi-viscous and bulk flow inertia effects in collisionless magnetotail reconnection. *Journal of Geophysical Research* 103:199–213
- Kuznetsova MM, Hesse M, Winske D (2001) Collisionless reconnection supported by nongyrotropic pressure effects in hybrid and particle simulations. *Journal of Geophysical Research: Space Physics* 106(A3):3799–3810, DOI 10.1029/1999JA001003
- Laitinen TV, Janhunen P, Pulkkinen TI, Palmroth M, Koskinen HEJ (2006) On the characterization of magnetic reconnection in global MHD simulations. *Annales Geophysicae* 24(11):3059–3069, DOI 10.5194/angeo-24-3059-2006

- Laitinen TV, Khotyaintsev YV, André M, Vaivads A, Reme H (2010) Local influence of the magnetosheath plasma beta fluctuations on magnetopause reconnection. *Ann Geophys* 28:1053
- Lapenta G (2017) Exactly energy conserving semi-implicit particle in cell formulation. *J Comput Phys* 334:349, DOI 10.1016/j.jcp.2017.01.002
- Lapenta G, Krauss-Varban D, Karimabadi H, Huba JD, Rudakov LI, Ricci P (2006) Kinetic simulations of x-line expansion in 3D reconnection. *Geophys Res Lett* 33:L10102
- Leclercq L, Modolo R, Leblanc F, Hess S, Mancini M (2016) 3D magnetospheric parallel hybrid multi-grid method applied to planet–plasma interactions. *J Comp Phys* 309:295–313, DOI 10.1016/j.jcp.2016.01.005, URL <https://doi.org/10.1016/j.jcp.2016.01.005>
- Lee JY, Sussman A (2004) Efficient communication between parallel programs with intercomm. Tech. rep., Citeseer
- Lemon C, Toffoletto F, Hesse M, Birn J (2003) Computing magnetospheric force equilibria. *Journal of Geophysical Research: Space Physics* 108(A6)
- Lemon C, Wolf R, Hill T, Sazykin S, Spiro R, Toffoletto F, Birn J, Hesse M (2004) Magnetic storm ring current injection modeled with the rice convection model and a self-consistent magnetic field. *Geophysical research letters* 31(21)
- Li C, Jia X, Chen Y, Toth G, Zhou H, Slavin JA, Sun W, Poh G (2023) Global hall mhd simulations of mercury’s magnetopause dynamics and ftes under different solar wind and imf conditions. *Journal of Geophysical Research: Space Physics* 128(5):e2022JA031206
- Li X, Baker D, Temerin M, Reeves G, Belian R (1998) Simulation of dispersionless injections and drift echoes of energetic electrons associated with substorms. *Geophysical Research Letters* 25(20):3763–3766
- Li X, Guo F, Li H, Li G (2015) Nonthermally Dominated Electron Acceleration during Magnetic Reconnection in a Low- β Plasma. *Astrophysical Journal Letters* 811(2):L24, DOI 10.1088/2041-8205/811/2/L24, [1505.02166](https://doi.org/10.1088/2041-8205/811/2/L24)
- Li X, Guo F, Li H, Li G (2017) Particle Acceleration during Magnetic Reconnection in a Low-beta Plasma. *Astrophysical Journal* 843(1):21, DOI 10.3847/1538-4357/aa745e
- Li X, Guo F, Li H, Birn J (2018) The Roles of Fluid Compression and Shear in Electron Energization during Magnetic Reconnection. *Astrophysical Journal* 855(2):80, DOI 10.3847/1538-4357/aaacd5, [1801.02255](https://doi.org/10.3847/1538-4357/aaacd5)
- Li X, Guo F, Li H (2019) Particle acceleration in kinetic simulations of nonrelativistic magnetic reconnection with different ion–electron mass ratios. *The Astrophysical Journal* 879(1):5
- Li X, Guo F, Li H, Stanier A, Kilian P (2019) Formation of Power-law Electron Energy Spectra in Three-dimensional Low- β Magnetic Reconnection. *Astrophysical Journal* 884(2):118, DOI 10.3847/1538-4357/ab4268, [1909.01911](https://doi.org/10.3847/1538-4357/ab4268)
- Li X, Guo F, Liu YH, Li H (2023) A Model for Nonthermal Particle Acceleration in Relativistic Magnetic Reconnection. *Astrophysical Journal Letters* 954(2):L37, DOI 10.3847/2041-8213/acf135, [2302.12737](https://doi.org/10.3847/2041-8213/acf135)

- Liemohn M, Ganushkina N, Zeeuw DD, Rastaetter L, Kuznetsova M, Welling D, Tóth G, Ilie R, Gombosi T, van der Holst B (2018) Real-time swmf at ccmc: assessing the dst output from continuous operational simulations. *Space Weather* 16:1583, DOI 10.1029/2018SW001953
- Liemohn MW, Kozyra JU, Clauer CR, Ridley AJ (2001) Computational analysis of the near-Earth magnetospheric current system during two-phase decay storms. *J Geophys Res* 106:29,531
- Lin D, Wang W, Merkin VG, Huang C, Oppenheim MM, Sorathia K, Pham KH, Michael A, Bao S, Wu Q, et al. (2022a) Ionospheric dawnside subauroral polarization streams: A unique feature of major geomagnetic storms. *Authorea Preprints*
- Lin Y (2002) Global hybrid simulation of hot flow anomalies near the bow shock and in the magnetosheath. *Planetary and space science* 50(5-6):577–591
- Lin Y, Wang X (2006) Formation of dayside low-latitude boundary layer under northward interplanetary magnetic field. *Geophysical research letters* 33(21)
- Lin Y, Wang XY (2005) Three-dimensional global hybrid simulation of dayside dynamics associated with the quasi-parallel bow shock. *Journal of Geophysical Research: Space Physics* 110(A12):1–13, DOI 10.1029/2005JA011243, URL <http://dx.doi.org/10.1029/2005JA011243>
- Lin Y, Lee L, Yan M (1996) Generation of dynamic pressure pulses downstream of the bow shock by variations in the interplanetary magnetic field orientation. *Journal of Geophysical Research: Space Physics* 101(A1):479–493
- Lin Y, Wang XY, Chang SW (2007) Connection between bow shock and cusp energetic ions. *Geophys Res Lett* 34:L11107, DOI 10.1029/2007GL030038, URL <https://doi.org/10.1029/2007GL030038>
- Lin Y, Wang XY, Brown MR, Schaffer MJ, Cothran CD (2008) Modeling Swarthmore spheromak reconnection experiment using hybrid code. *Plasma Phys Control Fusion* 50:074012, DOI 10.1088/0741-3335/50/7/074012, URL <https://doi.org/10.1088/0741-3335/50/7/074012>
- Lin Y, Johnson JR, Wang X (2012) Three-dimensional mode conversion associated with kinetic alfvén waves. *Physical review letters* 109(12):125003
- Lin Y, Wang XY, Lu S, Perez JD, Lu Q (2014) Investigation of storm time magnetotail and ion injection using three-dimensional global hybrid simulation. *Journal of Geophysical Research (Space Physics)* 119(9):7413–7432, DOI 10.1002/2014JA020005, URL <https://ui.adsabs.harvard.edu/abs/2014JGRA..119.7413L>
- Lin Y, Wing S, Johnson JR, Wang X, Perez JD, Cheng L (2017) Formation and transport of entropy structures in the magnetotail simulated with a 3-d global hybrid code. *Geophysical Research Letters* 44(12):5892–5899
- Lin Y, Wang X, Fok MC, Buzulukova N, Perez J, Cheng L, Chen LJ (2021a) Magnetotail-inner magnetosphere transport associated with fast flows based on combined global-hybrid and cimi simulation. *Journal of Geophysical Research: Space Physics* 126(3):e2020JA028405
- Lin Y, Wang X, Fok MC, Buzulukova N, Perez JD, Cheng L, Chen LJ (2021b) Magnetotail-Inner Magnetosphere Transport Associated With Fast Flows Based on Combined Global-Hybrid and CIMI Simulation. *J Geophys Res Space Physics*

- 126:e2020JA028405, DOI 10.1029/2020JA028405, URL <https://doi.org/10.1029/2020JA028405>
- Lin Y, Wang X, Sibeck DG, Wang CP, Lee SH (2022b) Global asymmetries of hot flow anomalies. *Geophysical Research Letters* 49(4):e2021GL096970
- Lin Y, Wang XY, Sibeck DG, Wang CP, Lee SH (2022c) Global Asymmetries of Hot Flow Anomalies. *Geophys Res Lett* 49:e2021GL096970, DOI 10.1029/2021GL096970, URL <https://doi.org/10.1029/2021GL096970>
- Lipatov AS (2002a) *The Hybrid Multiscale Simulation Technology*. Scientific Computation, Springer, Berlin, Heidelberg, DOI 10.1007/978-3-662-05012-5
- Lipatov AS (2002b) *The Hybrid Multiscale Simulation Technology*. Scientific Computation, Springer Berlin Heidelberg, Berlin, Heidelberg, DOI 10.1007/978-3-662-05012-5
- Liu J, V Angelopoulos XZZ, Yao ZH, Runov A (2015) Cross-tail expansion of dipolarizing flux bundles. *Journal of Geophysical Research* 120:2516
- Liu YH, Daughton W, Karimabadi H, Li H, Roytershteyn V (2013) Bifurcated Structure of the Electron Diffusion Region in Three-Dimensional Magnetic Reconnection. *Physical Review Letters* 110(26):265004, DOI 10.1103/PhysRevLett.110.265004, URL <http://link.aps.org/doi/10.1103/PhysRevLett.110.265004>
- Liu YH, Birn J, Daughton W, Hesse M, Schindler K (2014) Onset of reconnection in the near magnetotail: Pic simulations. *Journal of Geophysical Research: Space Physics* 119(12):9773–9789
- Liu YH, Li TC, Hesse M, Huang K (2019) Three-dimensional magnetic reconnection with a spatially confined x-line extent: Implications for dipolarizing flux bundles and the dawn-dusk asymmetry. *Journal of Geophysical Research: Space Physics* 128:2819–2830
- Liu YH, Cassak P, Li X, Hesse M, Lin SC, Genestreti K (2022) First-principles theory of the rate of magnetic reconnection in magnetospheric and solar plasmas. *Comms Phys* 5:97, DOI 10.1038/s42005-022-00854-x
- Liu YH, Hesse M, Genestreti K, Nakamura R, Burch J, Cassak P, Bessho N, Eastwood J, Phan T, Swisdak M, et al. (2024) Ohm's law, the reconnection rate, and energy conversion in collisionless magnetic reconnection. *arXiv preprint arXiv:240600875*
- Londrillo P, Del Zanna L (2004) On the divergence-free condition in Godunov-type schemes for ideal magnetohydrodynamics: the upwind constrained transport method. *Journal of Computational Physics* 195(1):17–48, DOI 10.1016/j.jcp.2003.09.016
- Lottermoser RF, Scholar M (1997) Undriven magnetic reconnection in magnetohydrodynamics and hall magnetohydrodynamics. *Journal of Geophysical Research: Space Physics* 102(A3):4875–4892, DOI <https://doi.org/10.1029/96JA03634>
- Loureiro NF, Schekochihin AA, Cowley SC (2007) Instability of current sheets and formation of plasmoid chains. *Phys Plasmas* 14:100703
- Lu S, Lin Y, Angelopoulos V, Artemyev A, Pritchett P, Lu Q, Wang X (2016) Hall effect control of magnetotail dawn-dusk asymmetry: A three-dimensional global hybrid simulation. *Journal of Geophysical Research: Space Physics* 121(12):11–882
- Lu S, Wang R, Lu Q, Angelopoulos V, Nakamura R, Artemyev AV, Pritchett PL, Liu TZ, Zhang XJ, Baumjohann W, Gonzalez W, Rager AC, Torbert RB, Giles

- BL, Gershman DJ, Russell CT, Strangeway RJ, Qi Y, Ergun RE, Lindqvist PA, Burch JL, Wang S (2020) Magnetotail reconnection onset caused by electron kinetics with a strong external driver. *Nature Communications* 11(1):5049, DOI 10.1038/s41467-020-18787-w
- Lu S, Lu Q, Wang R, Pritchett PL, Hubbert M, Qi Y, Huang K, Li X, Russell CT (2022) Electron-Only Reconnection as a Transition From Quiet Current Sheet to Standard Reconnection in Earth's Magnetotail: Particle-In-Cell Simulation and Application to MMS Data. *Geophysical Research Letters* 49(11):e2022GL098547, DOI 10.1029/2022GL098547
- Lyon J, Fedder J, Mobarri C (2004) The lyon–fedder–mobarri (lfm) global mhd magnetospheric simulation code. *Journal of Atmospheric and Solar-Terrestrial Physics* 66(15-16):1333–1350
- Ma Y, Russell C, Tóth G, Chen Y, Nagy A, Harada Y, McFadden J, Halekas J, Lillis R, Connerney J, Espley J, DiBraccio G, Markidis S, Peng IB, Fang X, Jakosky B (2018) Reconnection in the martian magnetotail: Hall-mhd with embedded particle-in-cell simulations. *J Geophys Res* 123:3742, DOI 10.1029/2017JA024729
- Ma ZW, Bhattacharjee A (1996) Fast impulsive reconnection and current sheet intensification due to electron pressure gradients in semi-collisional plasmas. *Geophys Res Lett* 23:1673
- Ma ZW, Bhattacharjee A (2001) Hall magnetohydrodynamic reconnection: The geospace environment modeling challenge. *Journal of Geophysical Research: Space Physics* 106(A3):3773–3782, DOI <https://doi.org/10.1029/1999JA001004>
- Makwana K, Keppens R, Lapenta G (2017) Two-way coupling of magnetohydrodynamic simulations with embedded particle-in-cell simulations. *Computer Phys Comm* 221:81, DOI 10.1016/j.cpc.2017.08.003
- Man HY, Zhou M, Yi YY, Zhong ZH, Tian AM, Deng XH, Khotyaintsev Y, Russell CT, Giles BL (2020) Observations of Electron-Only Magnetic Reconnection Associated With Macroscopic Magnetic Flux Ropes. *Geophysical Research Letters* 47(19):e2020GL089659, DOI 10.1029/2020GL089659
- Mandli KT, Ahmadi AJ, Berger M, Calhoun D, George DL, Hadjimichael Y, Ketcheson DI, Lemoine GI, LeVeque RJ (2016) Clawpack: building an open source ecosystem for solving hyperbolic pdes. *PeerJ Computer Science* 2:e68
- Mandt ME, Denton RE, Drake JF (1994a) Transition to whistler mediated magnetic reconnection. *Geophys Res Lett* 21:73
- Mandt ME, Denton RE, Drake JF (1994b) Transition to whistler mediated magnetic reconnection. *Geophysical Research Letters* 21(1):73–76, DOI 10.1029/93GL03382
- Mangeny A, Califano F, Cavazzoni C, Travnicek P (2002) A numerical scheme for the integration of the vlasov–maxwell system of equations. *Journal of Computational Physics* 179(2):495–538, DOI <https://doi.org/10.1006/jcph.2002.7071>, URL <https://www.sciencedirect.com/science/article/pii/S0021999102970713>
- Manzini D, Sahraoui F, Califano F (2023) Subion-scale turbulence driven by magnetic reconnection. *Phys Rev Lett* 130:205201, DOI 10.1103/PhysRevLett.130.205201, URL <https://link.aps.org/doi/10.1103/PhysRevLett.130.205201>
- Markidis S, Lapenta G, Rizwan-Uddin (2010a) Multi-scale simulations of plasma with ipic3d. *Mathematics and Computers in Simulation* 80:1509–1519, DOI 10.1016/j.matcom.2009.08.038

- Markidis S, Lapenta G, Rizwan-uddin (2010b) Multi-scale simulations of plasma with ipic3d. *Mathematics and Computers in Simulation* 80(7):1509–1519, DOI <https://doi.org/10.1016/j.matcom.2009.08.038>, URL <https://www.sciencedirect.com/science/article/pii/S0378475409002444>, multiscale modeling of moving interfaces in materials
- Matsumoto Y, Amano T, Kato TN, Hoshino M (2015) Stochastic electron acceleration during spontaneous turbulent reconnection in a strong shock wave. *Science* 347:974
- Matthaeus WH, Wan M, Servidio S, Greco A, Osman KT, Oughton S, Dmitruk P (2015) Intermittency, nonlinear dynamics and dissipation in the solar wind and astrophysical plasmas. *Philosophical Transactions of the Royal Society of London Series A* 373(2041):20140154–20140154, DOI 10.1098/rsta.2014.0154
- Matthaeus WH, Parashar TN, Wan M, Wu P (2016) Turbulence and proton–electron heating in kinetic plasma. *Astrophysical Journal Letters* 827:L7
- Matthaeus WH, Yang Y, Wan M, Parashar TN, Bandyopadhyay R, Chasapis A, Pezzi O, Valentini F (2020) Pathways to Dissipation in Weakly Collisional Plasmas. *The Astrophysical Journal* 891(1):101, DOI 10.3847/1538-4357/ab6d6a
- McPherron RL, Russell CT, Aubry MP (1973) Satellite studies of magnetospheric substorms on august 15, 1968: 9. phenomenological model for substorms. *Journal of Geophysical Research* 78(16):3131–3149
- Meng X, Tóth G, Gloer A, Fok MC, Gombosi TI (2013) Pressure anisotropy in global magnetospheric simulations: Coupling with ring current models. *J Geophys Res* 118:5639, DOI 10.1002/jgra.50539
- Merkin V, Lyon J (2010) Effects of the low-latitude ionospheric boundary condition on the global magnetosphere. *Journal of Geophysical Research: Space Physics* 115(A10)
- Merkin V, Sitnov M (2016) Stability of magnetotail equilibria with a tailward bz gradient. *Journal of Geophysical Research: Space Physics* 121(10):9411–9426
- Mouikis C, Omelchenko Y, Roytershteyn V (2021) Comparative study of the magnetotail loading of ionospheric O+ using 3D Global Hybrid simulations. In: AGU Fall Meeting 2021, held in New Orleans, LA, 13-17 December 2021, vol SH35G-02, URL <https://ui.adsabs.harvard.edu/abs/2021AGUFMSH35G..02M/abstract>
- Müller J, Simon S, Motschmann U, Scüller J, Glassmeier KH (2011) A.I.K.E.F.: Adaptive hybrid model for space plasma simulations. *Comp Phys Comm* 182:946–966
- Muñoz PA, Jain N, Kilian P, Büchner J (2018) A new hybrid code (CHIEF) implementing the inertial electron fluid equation without approximation. *Computer Physics Communications* 224:245–264, DOI 10.1016/j.cpc.2017.10.012
- Muñoz PA, Jain N, Farzalipour Tabriz M, Rampp M, Büchner J (2023) Electron inertia effects in 3D hybrid-kinetic collisionless plasma turbulence. *Physics of Plasmas* 30(9):092302, DOI 10.1063/5.0148818, URL <https://doi.org/10.1063/5.0148818>
- Nakamura TKM, Daughton W (2014) Turbulent plasma transport across the earth’s low-latitude boundary layer. *Geophys Res Lett* 41:8704
- Nakamura TKM, Nakamura R, Alexandrova A, Kubota Y, Nagai T (2012) Hall magnetohydrodynamic effects for three-dimensional magnetic reconnection with finite width along the direction of the current. *J Geophys Res* 117:03220
- Nakamura TKM, Hasegawa H, Daughton W, Eriksson S, Li W, Nakamura R (2017) Turbulent mass transfer caused by vortex induced reconnection in collisionless

- magnetospheric plasmas. *Nature Communications* 8:1582
- Nakamura TKM, Blasl KA, Hasegawa H, Umeda T, Liu YH, Peery SA, Plaschke F, Nakamura R, Holmes JC, Stawarz JE, Nystrom WD (2022) Multi-scale evolution of kelvin–helmholtz waves at the earth’s magnetopause during southward imf periods. *Phys Plasmas* 29:012901
- Ng J, Chen LJ, Omelchenko YA (2021) Bursty magnetic reconnection at the Earth’s magnetopause triggered by high-speed jets. *Phys Plasmas* 28:092902, DOI 10.1063/5.0054394, URL <https://doi.org/10.1063/5.0054394>
- Ng J, Chen LJ, Bessho N, Shuster J, Burkholder B, Yoo J (2022) Electron-scale reconnection in three-dimensional shock turbulence. *Geophysical Research Letters* 49:e2022GL099544
- Ohia O, Egedal J, Lukin VS, Daughton W, Le A (2012) Demonstration of anisotropic fluid closure capturing the kinetic structure of magnetic reconnection. *Phys Rev Lett* 109:115004, DOI 10.1103/PhysRevLett.109.115004, URL <https://link.aps.org/doi/10.1103/PhysRevLett.109.115004>
- Ohtani H, Horiuchi R (2009) Open boundary condition for particle simulation in magnetic reconnection research. *Plasma and Fusion Research* 4:24
- Oka M, Phan TD, Krucker S, Fujimoto M, Shinohara I (2010) Electron Acceleration by Multi-Island Coalescence. *Astrophysical Journal* 714(1):915–926, DOI 10.1088/0004-637X/714/1/915, [1004.1154](https://doi.org/10.1088/0004-637X/714/1/915)
- Oka M, Birn J, Egedal J, Guo F, Ergun RE, Turner DL, Khotyaintsev Y, Hwang KJ, Cohen IJ, Drake JF (2023) Particle Acceleration by Magnetic Reconnection in Geospace. *Space Science Reviews* 219(8):75, DOI 10.1007/s11214-023-01011-8, [2307.01376](https://doi.org/10.1007/s11214-023-01011-8)
- Omelchenko Y, Karimabadi H (2006a) Event-driven, hybrid particle-in-cell simulation: A new paradigm for multi-scale plasma modeling. *Journal of Computational Physics* 216(1):153 – 178, DOI <http://dx.doi.org/10.1016/j.jcp.2005.11.029>, URL <http://www.sciencedirect.com/science/article/pii/S0021999105005474>
- Omelchenko Y, Karimabadi H (2006b) Self-adaptive time integration of flux-conservative equations with sources. *Journal of Computational Physics* 216(1):179 – 194, DOI <http://dx.doi.org/10.1016/j.jcp.2005.12.008>, URL <http://www.sciencedirect.com/science/article/pii/S0021999105005619>
- Omelchenko Y, Karimabadi H (2007) A time-accurate explicit multi-scale technique for gas dynamics. *Journal of Computational Physics* 226(1):282 – 300, DOI <http://dx.doi.org/10.1016/j.jcp.2007.04.010>, URL <http://www.sciencedirect.com/science/article/pii/S002199910700157X>
- Omelchenko Y, Karimabadi H (2012) HYPERS: A unidimensional asynchronous framework for multiscale hybrid simulations. *Journal of Computational Physics* 231(4):1766–1780, DOI 10.1016/j.jcp.2011.11.004, URL <https://linkinghub.elsevier.com/retrieve/pii/S0021999111006462>
- Omelchenko Y, Chen LJ, Ng J (2021a) 3d space-time adaptive hybrid simulations of magnetosheath high-speed jets. *Journal of Geophysical Research: Space Physics* 126(7):e2020JA029035
- Omelchenko YA (2015) Formation, spin-up, and stability of field-reversed configurations. *Phys Rev E* 92:023105, DOI 10.1103/PhysRevE.92.023105, URL <http://dx.doi.org/10.1103/PhysRevE.92.023105>

- [//link.aps.org/doi/10.1103/PhysRevE.92.023105](https://link.aps.org/doi/10.1103/PhysRevE.92.023105)
- Omelchenko YA, Karimabadi H (2022) EMAPS - An Intelligent Agent-Based Technology for Simulation of Multiscale Systems. In: Büchner J (ed) Space and Astrophysical Plasma Simulation, Springer, URL https://doi.org/10.1007/978-3-031-11870-8_13
- Omelchenko YA, Sudan R (1997) A 3-D Darwin-EM Hybrid, PIC code for ion ring studies. *J Comp Phys* 133:146–159, DOI 10.1006/jcph.1997.5670, URL <https://doi.org/10.1006/jcph.1997.5670>
- Omelchenko YA, Chen LJ, Ng J (2021b) 3D Space-Time Adaptive Hybrid Simulations of Magnetosheath High-Speed Jets. *J Geophys Res Space Physics* 126:e2020JA029035, DOI 10.1029/2020JA029035, URL <https://doi.org/10.1029/2020JA029035>
- Omelchenko YA, Roytershteyn V, Chen LJ, Ng J, Hietala H (2021c) HYPERS simulations of solar wind interactions with the Earth’s magnetosphere and the Moon. *J Atmos Sol-Terr Phys* 215:105581, DOI 10.1016/j.jastp.2021.105581, URL <https://doi.org/10.1016/j.jastp.2021.105581>
- Omelchenko YA, Rudakov LI, Ng J, Crabtree C, Ganguli G (2021d) On the rate of energy deposition by an ion ring velocity ring. *Phys Plasmas* 28:052102, DOI 10.1063/5.0046309, URL <https://doi.org/10.1063/5.0046309>
- Omelchenko YA, Mouikis C, Ng J, Roytershteyn V, Chen LJ (2022) Multiscale Hybrid Modeling of the Impact Response of the Earth’s Magnetotail to Ionospheric O+ Outflow. *Frontiers in Astronomy and Space Science* Submitted
- Omidi N, Sibeck D (2007) Flux transfer events in the cusp. *Geophysical Research Letters* 34(4)
- Omidi N, Blanco-Cano X, Russell C, Karimabadi H (2004) Dipolar magnetospheres and their characterization as a function of magnetic moment. *Advances in Space Research* 33:1996–2003, DOI 10.1016/j.asr.2003.08.041, URL <https://doi.org/10.1016/j.asr.2003.08.041>
- Omidi N, Phan T, Sibeck D (2009) Hybrid simulations of magnetic reconnection initiated in the magnetosheath. *Journal of Geophysical Research: Space Physics* 114(A2)
- Omidi N, Eastwood J, Sibeck D (2010) Foreshock bubbles and their global magnetospheric impacts. *Journal of Geophysical Research: Space Physics* 115(A6)
- Palmroth M, Hoilijoki S, Juusola L, Pulkkinen TI, Hietala H, Pfau-Kempf Y, Ganse U, von Althaus S, Vainio R, Hesse M (2017) Tail reconnection in the global magnetospheric context: Vlasiator first results. *Annales Geophysicae* 35(6):1269–1274, DOI 10.5194/angeo-35-1269-2017, URL <https://angeo.copernicus.org/articles/35/1269/2017/>
- Palmroth M, Ganse U, Pfau-Kempf Y, Battarbee M, Turc L, Brito T, Grandin M, Hoilijoki S, Sandroos A, von Althaus S (2018a) Vlasov methods in space physics and astrophysics. *Living Reviews in Computational Astrophysics* 4(1):1
- Palmroth M, Hietala H, Plaschke F, Archer M, Karlsson T, Blanco-Cano X, Sibeck D, Kajdič P, Ganse U, Pfau-Kempf Y, Battarbee M, Turc L (2018b) Magnetosheath jet properties and evolution as determined by a global hybrid-Vlasov simulation. *Annales Geophysicae* 36:1171–1182, DOI 10.5194/angeo-36-1171-2018, URL <https://doi.org/10.5194/angeo-36-1171-2018>

[//doi.org/10.5194/angeo-36-1171-2018](https://doi.org/10.5194/angeo-36-1171-2018)

- Palmroth M, Pulkkinen TI, Ganse U, Pfau-Kempf Y, Koskela T, Zaitsev I, Alho M, Cozzani G, Turc L, Battarbee M, Dubart M, George H, Gordeev E, Grandin M, Horaites K, Osmane A, Papadakis K, Suni J, Tarvus V, Zhou H, Nakamura R (2023) Magnetotail plasma eruptions driven by magnetic reconnection and kinetic instabilities. *Nature Geoscience* 16(7):570–576
- Pang Y, Lin Y, Deng X, Wang X, Tan B (2010) Three-dimensional hybrid simulation of magnetosheath reconnection under northward and southward interplanetary magnetic field. *Journal of Geophysical Research: Space Physics* 115(A3)
- Papadakis K, Pfau-Kempf Y, Ganse U, Battarbee M, Alho M, Grandin M, Dubart M, Turc L, Zhou H, Horaites K, Zaitsev I, Cozzani G, Bussov M, Gordeev E, Tesema F, George H, Suni J, Tarvus V, Palmroth M (2022) Spatial filtering in a 6D hybrid-Vlasov scheme to alleviate adaptive mesh refinement artifacts: a case study with Vlasiator (versions 5.0, 5.1, and 5.2.1). *Geoscientific Model Development* 15(20):7903–7912, DOI 10.5194/gmd-15-7903-2022
- Parker EN (1957a) Newtonian development of the dynamical properties of ionized gases of low density. *Phys Rev* 107:924–933, DOI 10.1103/PhysRev.107.924, URL <https://link.aps.org/doi/10.1103/PhysRev.107.924>
- Parker EN (1957b) Sweet’s mechanism for merging magnetic fields in conducting fluids. *J Geophys Res* 62:509
- Parker EN (1963) The solar-flare phenomenon and the theory of reconnection and annihilation of magnetic fields. *Ap J* 8:177
- Parker EN (1973) The reconnection rate of magnetic fields. *Ap J* 180:247
- Paty C, Winglee R (2004) Multi-fluid simulations of ganymede’s magnetosphere. *Geophys Res Lett* 31:L24806
- Pembroke A, Toffoletto F, Sazykin S, Wiltberger M, Lyon J, Merkin V, Schmitt P (2012) Initial results from a dynamic coupled magnetosphere-ionosphere-ring current model. *Journal of Geophysical Research: Space Physics* 117(A2)
- Peromian V, El-Alaoui M (2008) The storm-time access of solar wind ions to the nightside ring current and plasma sheet. *Journal of Geophysical Research: Space Physics* 113(A6)
- Perrone D, Valentini F, Servidio S, Dalena S, Veltri P (2012) Vlasov simulations of multi-ion plasma turbulence in the solar wind. *The Astrophysical Journal* 762(2):99, DOI 10.1088/0004-637X/762/2/99, URL <https://dx.doi.org/10.1088/0004-637X/762/2/99>
- Pezzi O, Servidio S, Perrone D, Valentini F, Sorriso-Valvo L, Greco A, Matthaeus WH, Veltri P (2018) Velocity-space cascade in magnetized plasmas: Numerical simulations. *Physics of Plasmas* 25(6):060704, DOI 10.1063/1.5027685, [1803.01633](https://doi.org/10.1063/1.5027685)
- Pezzi O, Cozzani G, Califano F, Valentini F, Guarrasi M, Camporeale E, Brunetti G, Retinò A, Veltri P (2019) Vida: a vlasov–darwin solver for plasma physics at electron scales. *Journal of Plasma Physics* 85(5):905850506, DOI 10.1017/S0022377819000631
- Pezzi O, Perrone D, Servidio S, Valentini F, Sorriso-Valvo L, Veltri P (2019) Proton-Proton Collisions in the Turbulent Solar Wind: Hybrid Boltzmann-Maxwell Simulations. *The Astrophysical Journal* 887(2):208, DOI 10.3847/1538-4357/ab5285, [1903.03398](https://doi.org/10.3847/1538-4357/ab5285)

- Pezzi O, Yang Y, Valentini F, Servidio S, Chasapis A, Matthaeus WH, Veltri P (2019) Energy conversion in turbulent weakly collisional plasmas: Eulerian hybrid Vlasov-Maxwell simulations. *Physics of Plasmas* 26(7), DOI 10.1063/1.5100125, URL <https://doi.org/10.1063/1.5100125>, 072301, https://pubs.aip.org/aip/pop/article-pdf/doi/10.1063/1.5100125/13820638/072301_1.online.pdf
- Pezzi O, Liang H, Juno JL, Cassak PA, Vásconez CL, Sorriso-Valvo L, Perrone D, Servidio S, Roytershteyn V, TenBarge JM, Matthaeus WH (2021a) Dissipation measures in weakly collisional plasmas. *Monthly Notices of the Royal Astronomical Society* 505(4):4857–4873, DOI 10.1093/mnras/stab1516, [2101.00722](https://doi.org/10.1093/mnras/stab1516)
- Pezzi O, Pecora F, Le Roux J, Engelbrecht NE, Greco A, Servidio S, Malova HV, Khabarova OV, Malandraki O, Bruno R, Matthaeus WH, Li G, Zelenyi LM, Kislov RA, Obridko VN, Kuznetsov VD (2021b) Current Sheets, Plasmoids and Flux Ropes in the Heliosphere. Part II: Theoretical Aspects. *Space Science Reviews* 217(3):39, DOI 10.1007/s11214-021-00799-7, [2101.05007](https://doi.org/10.1007/s11214-021-00799-7)
- Pfau-Kempf Y, Hietala H, Milan SE, Juusola L, Hoilijoki S, Ganse U, von Alfthan S, Palmroth M (2016) Evidence for transient, local ion foreshocks caused by dayside magnetopause reconnection. *Annales Geophysicae* 34(11):943–959, DOI 10.5194/angeo-34-943-2016, URL <https://angeo.copernicus.org/articles/34/943/2016/>
- Pfau-Kempf Y, Palmroth M, Johlander A, Turc L, Alho M, Battarbee M, Dubart M, Grandin M, Ganse U (2020a) Hybrid-Vlasov modeling of three-dimensional dayside magnetopause reconnection. *Phys Plasmas* 27:092903, DOI <https://doi.org/10.1063/5.0020685>, URL <https://aip.scitation.org/doi/10.1063/5.0020685>
- Pfau-Kempf Y, Palmroth M, Johlander A, Turc L, Alho M, Battarbee M, Dubart M, Grandin M, Ganse U (2020b) Hybrid-Vlasov modeling of three-dimensional dayside magnetopause reconnection. *Physics of Plasmas* 27(9):092903
- Pham KH, Zhang B, Sorathia K, Dang T, Wang W, Merkin V, Liu H, Lin D, Wiltberger M, Lei J, et al. (2022) Thermospheric density perturbations produced by traveling atmospheric disturbances during august 2005 storm. *Journal of Geophysical Research: Space Physics* 127(2):e2021JA030071
- Phan TD, Drake JF, Shay MA, Mozer FS, Eastwood JP (2007) Evidence for an elongated (>60 ion skin depths) electron diffusion region during fast magnetic reconnection. *Phys Rev Lett* 99:255002
- Phan TD, Eastwood JP, Shay MA, Drake JF, Sonnerup BUÖ, Fujimoto M, Cassak PA, Øieroset M, Burch JL, Torbert RB, Rager AC, Dorelli JC, Gershman DJ, Pollock C, Pyakurel PS, Haggerty CC, Khotyaintsev Y, Lavraud B, Saito Y, Oka M, Ergun RE, Retino A, Le Contel O, Argall MR, Giles BL, Moore TE, Wilder FD, Strangeway RJ, Russell CT, Lindqvist PA, Magnes W (2018) Electron magnetic reconnection without ion coupling in Earth’s turbulent magnetosheath. *Nature* 557(7704):202–206, DOI 10.1038/s41586-018-0091-5
- Pontius Jr D, Wolf R (1990) Transient flux tubes in the terrestrial magnetosphere. *Geophysical research letters* 17(1):49–52
- Poppe AR (2019) Comment on ”the dominant role of energetic ions in solar wind interaction with the moon” by omidi et al. *J Geophys Res: Space Physics* 124:6927–6932, DOI <https://doi.org/10.1029/2019JA026692>

- Powell K, Roe P, Linde T, Gombosi T, De Zeeuw DL (1999) A solution-adaptive upwind scheme for ideal magnetohydrodynamics. *J Comput Phys* 154:284–309, DOI 10.1006/jcph.1999.6299
- Powell KG (1994) An approximate Riemann solver for magnetohydrodynamics (that works in more than one dimension). Tech. Rep. 94-24, Inst. for Comput. Appl. in Sci. and Eng., NASA Langley Space Flight Center, Hampton, Va.
- Press WH, Teukolsky SA, Vetterling WT, Flannery BP (1992) *Numerical Recipes in Fortran 77*, Cambridge University Press, chap 7.3, pp 281–286
- Priest E, Forbes T (2000) *Magnetic Reconnection*. Cambridge University Press
- Pritchett P, Coroniti FV, Pella R (1991) Collisionless reconnection in two-dimension magnetotail equilibria. *Journal of Geophysical Research: Space Physics* 96(A7):11523–11538
- Pritchett PL (2005) Onset and saturation of guide-field magnetic reconnection. *Physics of Plasmas* 12(6):062301, DOI 10.1063/1.1914309
- Raeder J (2006) Flux Transfer Events: 1. generation mechanism for strong southward IMF. *Ann Geophys* 24(1):381–392, DOI 10.5194/angeo-24-381-2006
- Raeder J, Berchem J, Ashour-Abdalla M, Frank L, Paterson W, Ackerson K, Kokubun S, Yamamoto T, Slavin J (1997) Boundary layer formation in the magnetotail: Geotail observations and comparisons with a global MHD simulation. *Geophys Res Lett* 24:951, DOI 10.1029/97GL00218
- Raeder J, McPherron R, Frank L, Kokubun S, Lu G, Mukai T, Paterson W, Sigwarth J, Singer H, Slavin J (2001) Global simulation of the geospace environment modeling substorm challenge event. *Journal of Geophysical Research: Space Physics* 106(A1):381–395
- Raeder J, Cramer WD, Jensen J, Fuller-Rowell T, Maruyama N, Toffoletto F, Vo H (2016) Sub-auroral polarization streams: A complex interaction between the magnetosphere, ionosphere, and thermosphere. In: *Journal of Physics: Conference Series*, IOP Publishing, vol 767, p 012021
- Reiff PH, Webster JM, Daou AG, Marshall A, Sazykin SY, Rastaetter L, Welling DT, DeZeeuw D, Kuznetsova MM, Glocher A, Russell CT (2017) CCMC modeling of magnetic reconnection in electron diffusion region events. In: Foullon C, Malandraki OE (eds) *Proceedings of the International Astronomical Union*, vol 13, pp 142–146, doi:10.1017/S1743921317010845
- Ridley A, Gombosi T, DeZeeuw D (2004) Ionospheric control of the magnetosphere: conductance. *Annales Geophysicae* 22:567–584, DOI 10.5194/angeo-22-567-2004
- Rieke M, Trost T, Grauer R (2015) Coupled Vlasov and two-fluid codes on GPUs. *Journal of Computational Physics* 283:436–452, DOI 10.1016/j.jcp.2014.12.016, URL <http://dx.doi.org/10.1016/j.jcp.2014.12.016>
- Robinson R, Vondrak R, Miller K, Dabbs T, Hardy D (1987) On calculating ionospheric conductances from the flux and energy of precipitating electrons. *Journal of Geophysical Research: Space Physics* 92(A3):2565–2569
- Roble R, Ridley EC, Richmond A, Dickinson R (1988) A coupled thermosphere/ionosphere general circulation model. *Geophysical Research Letters* 15(12):1325–1328

- Rogers BN, Denton RE, Drake JF, Shay MA (2001) Role of dispersive waves in collisionless magnetic reconnection. *Phys Rev Lett* 87(19):195004
- Rogers BN, Denton RE, Drake JF (2003) Signatures of collisionless magnetic reconnection. *J Geophys Res* 108(A3):10.1029/2002JA009699
- Roytershteyn V, Karimabadi H, Omelchenko Y, Germaschewski K (2015) Kinetic simulations of collisionless turbulence across scales. In: *Solar Heliospheric and Interplanetary Environment (SHINE 2016)*, The SHINE conference held 5-10 July, 2015 at The StoweFlake Resort in Stowe, VT, URL <https://ui.adsabs.harvard.edu/abs/2015shin.confE.117R/abstract>, 2015shin.confE.117R
- Rueda JAA, Verscharen D, TWicks R, Owen CJ, Nicolaou G, PWalsh A, Zouganelis I, Germaschewski K, Domínguez SV (2021) Three-dimensional magnetic reconnection in particle-in-cell simulations of anisotropic plasma turbulence. *J Plasma Phys* 87:905870228
- Runov A, Grandin M, Palmroth M, Battarbee M, Ganse U, Hietala H, Hoilijoki S, Kilpua E, Pfau-Kempf Y, Toledo-Redondo S, Turc L, Turner D (2021) Ion distribution functions in magnetotail reconnection: global hybrid-vlasov simulation results. *Annales Geophysicae* 39(4):599–612, DOI 10.5194/angeo-39-599-2021, URL <https://angeo.copernicus.org/articles/39/599/2021/>
- Sachsenweger D, Scholer M, Möbius E (1989) Test particle acceleration in a magnetotail reconnection configuration. *Geophysical Research Letters* 16(9):1027–1030
- Sarrat M, Ghizzo A, Del Sarto D, Serrat L (2017) Parallel implementation of a relativistic semi-Lagrangian Vlasov–Maxwell solver. *The European Physical Journal D* 71(11):271, DOI 10.1140/epjd/e2017-80188-4
- Sato T, Hayashi T (1979) Externally driven magnetic reconnection and a powerful magnetic energy converter. *Phys Fluids* 22:1189
- Schekochihin AA, Parker JT, Highcock EG, Dellar PJ, Dorland W, Hammett GW (2016) Phase mixing versus nonlinear advection in drift-kinetic plasma turbulence. *Journal of Plasma Physics* 82(2):905820212, DOI 10.1017/S0022377816000374, [1508.05988](https://doi.org/10.1017/S0022377816000374)
- Schindler K (1972) A self-consistent theory of the tail of the magnetosphere. In: *Earth’s Magnetospheric Processes: Proceedings of a Symposium Organized by the Summer Advanced Study Institute and Ninth ESRO Summer School, Held in Cortina, Italy, August 30-September 10, 1971*, Springer, pp 200–209
- Schmitz H, Grauer R (2006a) Darwin–vlasov simulations of magnetised plasmas. *Journal of Computational Physics* 214(2):738–756, DOI <https://doi.org/10.1016/j.jcp.2005.10.013>, URL <https://www.sciencedirect.com/science/article/pii/S0021999105004717>
- Schmitz H, Grauer R (2006b) Kinetic vlasov simulations of collisionless magnetic reconnection. *Physics of Plasmas* 13(9):092309, DOI <https://doi.org/10.1063/1.2347101>
- Scholer M, Jamitzky F (1987) Particle orbits during the development of plasmoids. *Journal of Geophysical Research: Space Physics* 92(A11):12181–12186
- Scholer M, Otto A (1991) Magnetotail reconnection: Current diversion and field-aligned currents. *Geophysical Research Letters* 18(4):733–736

- Schrifer D, Ashour-Abdalla M, Zelenyi L, Gombosi T, Ridley A, De Zeeuw D, Toth G, Monostori G (2005) Modeling the kinetic transport of electrons through the earth's global magnetosphere. In: Proceedings of the 7th International School/Symposium for Space Simulations. Research Institute for Sustainable Humanosphere, Kyoto University, Kyoto, Japan, pp 345–346
- Schumaker TL, Gussenhoven MS, Hardy DA, Carovillano RL (1989) The relationship between diffuse auroral and plasma sheet electron distributions near local midnight. *Journal of Geophysical Research: Space Physics* 94(A8):10061–10078
- Sciola A, Merkin V, Sorathia K, Gkioulidou M, Bao S, FToffoletto, Pham K, Lin D, Michael A, Wiltberger M, Ukhorskiy A (2023) The buildup and evolution of the stormtime ring current via mesoscale plasma sheet flows. Submitted to *Journal of Geophysical Research*
- Sergeev V, Nikolaev A, Tsyganenko N, Angelopoulos V, Runov A, Singer H, Yang J (2014) Testing a two-loop pattern of the substorm current wedge (scw2l). *Journal of Geophysical Research: Space Physics* 119(2):947–963
- Servidio S, Valentini F, Califano F, Veltri P (2012) Local kinetic effects in two-dimensional plasma turbulence. *Phys Rev Lett* 108:045001, DOI 10.1103/PhysRevLett.108.045001, URL <https://link.aps.org/doi/10.1103/PhysRevLett.108.045001>
- Servidio S, Osman KT, Valentini F, Perrone D, Califano F, Chapman S, Matthaeus WH, Veltri P (2014) Proton kinetic effects in vlasov and solar wind turbulence. *The Astrophysical Journal Letters* 781(2):L27, DOI 10.1088/2041-8205/781/2/L27, URL <https://dx.doi.org/10.1088/2041-8205/781/2/L27>
- Servidio S, Valentini F, Perrone D, Greco A, Califano F, Matthaeus WH, Veltri P (2015) A kinetic model of plasma turbulence. *Journal of Plasma Physics* 81(1):325810107, DOI 10.1017/S0022377814000841
- Servidio S, Chasapis A, Matthaeus WH, Perrone D, Valentini F, Parashar TN, Veltri P, Gershman D, Russell CT, Giles B, Fuselier SA, Phan TD, Burch J (2017) Magnetospheric Multiscale Observation of Plasma Velocity-Space Cascade: Hermite Representation and Theory. *Physical Review Letters* 119(20):205101, DOI 10.1103/PhysRevLett.119.205101, [1707.08180](https://doi.org/10.1103/PhysRevLett.119.205101)
- Sharma Pyakurel P, Shay MA, Phan TD, Matthaeus WH, Drake JF, TenBarge JM, Haggerty CC, Klein KG, Cassak PA, Parashar TN, Swisdak M, Chasapis A (2019) Transition from ion-coupled to electron-only reconnection: Basic physics and implications for plasma turbulence. *Physics of Plasmas* 26(8):082307, DOI 10.1063/1.5090403
- Shay MA, Drake JF, Denton RE, Biskamp D (1998) Structure of the dissipation region during collisionless magnetic reconnection. *Journal of Geophysical Research: Space Physics* 103(A5):9165–9176, DOI 10.1029/97JA03528
- Shay MA, Drake JF, Rogers BN, Denton RE (1999) The scaling of collisionless, magnetic reconnection for large systems. *Geophysical Research Letters* 26(14):2163–2166, DOI 10.1029/1999GL900481
- Shay MA, Drake JF, Swisdak M, Dorland W, Rogers BN (2003) Inherently three-dimensional magnetic reconnection: A mechanism for bursty bulk flows? *Geophys Res Lett* 30:1345

- Shay MA, Drake JF, Swisdak M, Rogers BN (2004) The scaling of embedded collisionless reconnection. *Phys Plasmas* 11(5):2199–2213
- Shay MA, Drake JF, Swisdak M (2007) Two-scale structure of the electron dissipation region during collisionless magnetic reconnection. *Phys Rev Lett* 99:155002, DOI 10.1103/PhysRevLett.99.155002
- Shay MA, Haggerty CC, Matthaeus WH, Parashar TN, Wan M, Wu P (2018) Turbulent heating due to magnetic reconnection. *Phys Plasmas* 25:012304
- Shepherd LS, Cassak PA (2010) Comparison of secondary islands in collisional reconnection to Hall reconnection. *Phys Rev Lett* 105:015004
- Shepherd LS, Cassak PA (2012) Guide field dependence of 3D X-line spreading during collisionless magnetic reconnection. *J Geophys Res* 117:A10101
- Shi F, Lin Y, Wang X (2013) Global hybrid simulation of mode conversion at the dayside magnetopause. *Journal of Geophysical Research: Space Physics* 118(10):6176–6187
- Shi F, Lin Y, Wang X, Wang B, Nishimura Y (2021) 3-d global hybrid simulations of magnetospheric response to foreshock processes. *Earth, Planets and Space* 73(1):1–17
- Shiroto T (2023) An improved Darwin approximation in the classical electromagnetism. *Physics of Plasmas* 30(4):044501, DOI 10.1063/5.0138048
- Shou Y, Tenishev V, Chen Y, Tóth G, Ganushkina N (2021) Magnetohydrodynamic with Adaptively Embedded Particle-in-Cell model: MHD-AEPIC. *Journal of Computational Physics* 446:110656, DOI 10.1016/j.jcp.2021.110656
- Sitnov M, Birn J, Ferdousi B, Gordeev E, Khotyaintsev Y, Merkin V, Motoba T, Otto A, Panov E, Pritchett P, et al. (2019) Explosive magnetotail activity. *Space science reviews* 215:1–95
- Sonnerup BUÖ (1979) Magnetic field reconnection. In: Lanzerotti LJ, Kennel CF, Parker EN (eds) *Solar System Plasma Physics*, vol 3, North Holland Publishing, Amsterdam, p 46
- Sonnerup BUÖ, Paschmann G, Papamastorakis I, Scopke N, Haerendel G, Bame SJ, Asbridge JR, Gosling JT, Russell CT (1986) Evidence for magnetic field reconnection at the earth’s magnetopause. *Journal of Geophysical Research: Space Physics* 86(A12):10049–10067
- Sorathia K, Merkin V, Ukhorskiy A, Mauk B, Sibeck D (2017) Energetic particle loss through the magnetopause: A combined global mhd and test-particle study. *Journal of Geophysical Research: Space Physics* 122(9):9329–9343
- Sorathia K, Michael A, Merkin VG, Ukhorskiy AY, Turner DL, Lyon J, Garretson J, Gkioulidou M, Toffoletto F (2021) The role of mesoscale plasma sheet dynamics in ring current formation. *Frontiers in Astronomy and Space Sciences* 8:761875
- Sorriso-Valvo L, Perrone D, Pezzi O, Valentini F, Servidio S, Zouganelis I, Veltri P (2018) Local energy transfer rate and kinetic processes: the fate of turbulent energy in two-dimensional hybrid vlasov–maxwell numerical simulations. *Journal of Plasma Physics* 84(2):725840201, DOI 10.1017/S0022377818000302
- Spence HE, Kivelson MG, Walker RJ, McComas DJ (1989) Magnetospheric plasma pressures in the midnight meridian: Observations from 2.5 to 35 re. *Journal of Geophysical Research: Space Physics* 94(A5):5264–5272

- Stanier A, Daughton W, Chacón L, Karimabadi H, Ng J, Huang YM, Hakim A, Bhattacharjee A (2015) Role of Ion Kinetic Physics in the Interaction of Magnetic Flux Ropes. *Physical Review Letters* 115(17):175004, DOI 10.1103/PhysRevLett.115.175004, URL <http://link.aps.org/doi/10.1103/PhysRevLett.115.175004>
- Stawarz JE, Eastwood JP, Phan TD, Gingell IL, Pyakurel PS, Shay MA, Robertson SL, Russell CT, Le Contel O (2022) Turbulence-driven magnetic reconnection and the magnetic correlation length: Observations from Magnetospheric Multiscale in Earth's magnetosheath. *Physics of Plasmas* 29(1):012302, DOI 10.1063/5.0071106
- Strang G (1968) On the Construction and Comparison of Difference Schemes. *SIAM Journal on Numerical Analysis* 5(3):506–517, DOI 10.1137/0705041
- Sulem PL, Passot T (2015) Landau fluid closures with nonlinear large-scale finite larmor radius corrections for collisionless plasmas. *Journal of Plasma Physics* 81(1):325810103, DOI 10.1017/S0022377814000671
- Sun W, Dewey RM, Aizawa S, Huang J, Slavin JA, Fu S, Wei Y, Bowers CF (2022) Review of mercury's dynamic magnetosphere: Post-messenger era and comparative magnetospheres. *Science China Earth Sciences* 65:25
- Sun WJ, Fu SY, Slavin JA, Raines JM, Zong QG, Poh GK, Zurbuchen TH (2016) Spatial distribution of mercury's flux ropes and reconnection fronts: Messenger observations. *Journal of Geophysical Research* 121:7590
- Suni J, Palmroth M, Turc L, Battarbee M, Johlander A, Tarvus V, Alho M, Bussov M, Dubart M, Ganse U, Grandin M, Horaites K, Manglayev T, Papadakis K, Pfau-Kempf Y, Zhou H (2021) Connection between foreshock structures and the generation of magnetosheath jets: Vlasiator results. *Geophysical Research Letters* 48(20):e2021GL095655, DOI <https://doi.org/10.1029/2021GL095655>, e2021GL095655 2021GL095655, <https://agupubs.onlinelibrary.wiley.com/doi/pdf/10.1029/2021GL095655>
- Sweet PA (1958) The neutral point theory of solar flares. In: Lehnert B (ed) *Electromagnetic Phenomena in Cosmical Physics*, Cambridge University Press, New York, p 123
- Swift DW (1996) Use of a Hybrid Code for Global-Scale Plasma Simulation. *Journal of Computational Physics* 126:109–121
- Swift DW, Lin Y (2001) Substorm onset viewed by a two-dimensional, global-scale hybrid code. *Journal of Atmospheric and Solar-Terrestrial Physics* 63(7):683–704
- Swisdak M, Drake JF, Price L, Burch JL, Cassak PA, Phan TD (2018) Localized and intense energy conversion in the diffusion region of asymmetric magnetic reconnection. *Geophysical Research Letters* 45(11):5260–5267
- Tan B, Lin Y, Perez J, Wang X (2011) Global-scale hybrid simulation of dayside magnetic reconnection under southward imf: Structure and evolution of reconnection. *Journal of Geophysical Research: Space Physics* 116(A2)
- Tan B, Lin Y, Perez J, Wang X (2012) Global-scale hybrid simulation of cusp precipitating ions associated with magnetopause reconnection under southward imf. *Journal of Geophysical Research: Space Physics* 117(A3)
- Tatsuno T, Dorland W, Schekochihin AA, Plunk GG, Barnes M, Cowley SC, Howes GG (2009) Nonlinear Phase Mixing and Phase-Space Cascade of Entropy in Gyrokinetic Plasma Turbulence. *Physical Review Letters* 103(1):015003, DOI 10.1103/

- PhysRevLett.103.015003, [0811.2538](https://doi.org/10.1103/PhysRevLett.103.015003)
- Thoma C, Welch DR, Hsu SC (2013) Particle-in-cell simulations of collisionless shock formation via head-on merging of two laboratory supersonic plasma jets. *Phys Plasmas* 20:082128, DOI 10.1063/1.4819063, URL <http://dx.doi.org/10.1063/1.4819063>
- Toffoletto F (2020) "Modelling Techniques" in Ring current investigations: The quest for space weather prediction. Elsevier, edited by Jordanova, Vania K and Ilie, Raluca and Chen, Margaret W
- Toffoletto F, Sazykin S, Spiro R, Wolf R (2003a) Inner magnetospheric modeling with the Rice Convection Model. *Space Sci Rev* 107:175–196, DOI 10.1023/A:1025532008047
- Toffoletto F, Sazykin S, Spiro R, Wolf R (2003b) Inner magnetospheric modeling with the rice convection model. *Space science reviews* 107:175–196
- Toledo-Redondo S, André M, Aunai N, Chappell CR, Dargent J, Fuselier SA, Glocer A, Graham DB, Haaland S, Hesse M, Kistler LM, Lavraud B, Li W, Moore TE, Tenfjord P, Vines SK (2021) Impacts of Ionospheric Ions on Magnetic Reconnection and Earth's Magnetosphere Dynamics. *Reviews of Geophysics* 59:e2020RG000707, DOI 10.1029/2020RG000707, URL <https://doi.org/10.1029/2020RG000707>
- Tóth G, Sokolov IV, Gombosi TI, Chesney DR, Clauer C, Zeeuw DLD, Hansen KC, Kane KJ, Manchester WB, Powell KG, Ridley AJ, Roussev II, Stout QF, Volberg O, Wolf RA, Sazykin S, Chan A, Yu B, Kóta J (2005) Space Weather Modeling Framework: A new tool for the space science community. *J Geophys Res* 110:A12226, DOI 10.1029/2005JA011126
- Tóth G, Sokolov IV, Gombosi TI, Chesney DR, Clauer CR, De Zeeuw DL, Hansen KC, Kane KJ, Manchester WB, Oehmke RC, et al. (2005) Space weather modeling framework: A new tool for the space science community. *Journal of Geophysical Research: Space Physics* 110(A12)
- Tóth G, Ma YJ, Gombosi TI (2008) Hall magnetohydrodynamics on block adaptive grids. *J Comput Phys* 227:6967
- Tóth G, Van der Holst B, Sokolov IV, De Zeeuw DL, Gombosi TI, Fang F, Manchester WB, Meng X, Najib D, Powell KG, et al. (2012) Adaptive numerical algorithms in space weather modeling. *Journal of Computational Physics* 231(3):870–903
- Tóth G, van der Holst B, Sokolov IV, Zeeuw DLD, Gombosi TI, Fang F, Manchester WB, Meng X, Najib D, Powell KG, Stout QF, Glocer A, Ma YJ, Opher M (2012) Adaptive numerical algorithms in space weather modeling. *J Comput Phys* 231:870–903, DOI 10.1016/j.jcp.2011.02.006
- Tóth G, Jia X, Markidis S, Peng B, Chen Y, Daldorff L, Tenishev V, Borovikov D, Haiducek J, Gombosi T, Glocer A, Dorelli J (2016) Extended magnetohydrodynamics with embedded particle-in-cell simulation of ganymede's magnetosphere. *J Geophys Res* 121, DOI 10.1002/2015JA021997
- Tóth G, Chen Y, Gombosi TI, Cassak P, , Markidis S, Peng B (2017) Scaling the ion inertial length and its implications for modeling reconnection in global simulations. *J Geophys Res* 122:10336, DOI 10.1002/2017JA024189
- Tronci C, Camporeale E (2015) Neutral vlasov kinetic theory of magnetized plasmas. *Physics of Plasmas* 22(2):020704, DOI 10.1063/1.4907665, URL <https://doi.org/10.1063/1.4907665>

[1063/1.4907665](https://doi.org/10.1063/1.4907665), <https://doi.org/10.1063/1.4907665>

- Trottenberg U, Oosterlee CW, Schuller A (2000) Multigrid. Academic Press, San Diego
- Turc L, Fontaine D, Savoini P, Modolo R (2015) 3d hybrid simulations of the interaction of a magnetic cloud with a bow shock. *J Geophys Res: Space Physics* 120:6133–6151, DOI 10.1002/2015JA021318, URL <https://doi.org/10.1002/2015JA021318>
- Turc L, Roberts OW, Verscharen D, Dimmock AP, Kajdič P, Palmroth M, Pfau-Kempf Y, Johlander A, Dubart M, Kilpua EKJ, Soucek J, Takahashi K, Takahashi N, Battarbee M, Ganse U (2023) Transmission of foreshock waves through earth's bow shock. *Nature Physics* 19(1):78–86
- Ugai M, Tsuda T (1977) Magnetic field line reconnection by localized enhancement of resistivity, 1, evolution in a compressible mhd fluid. *J Plasma Phys* 17:337
- Ukhorskiy A, Sitnov M, Merkin V, Gkioulidou M, Mitchell D (2017) Ion acceleration at dipolarization fronts in the inner magnetosphere. *Journal of Geophysical Research: Space Physics* 122(3):3040–3054
- Ukhorskiy AY, Sorathia KA, Merkin VG, Sitnov MI, Mitchell DG, Gkioulidou M (2018) Ion trapping and acceleration at dipolarization fronts: High-resolution mhd and test-particle simulations. *Journal of Geophysical Research: Space Physics* 123(7):5580–5589
- Umeda T, Togano K, Ogino T (2009) Two-dimensional full-electromagnetic Vlasov code with conservative scheme and its application to magnetic reconnection. *Computer Physics Communications* 180(3):365–374, DOI 10.1016/j.cpc.2008.11.001
- Umeda T, Miwa Ji, Matsumoto Y, Nakamura TKM, Togano K, Fukazawa K, Shinohara I (2010) Full electromagnetic Vlasov code simulation of the Kelvin-Helmholtz instability. *Physics of Plasmas* 17(5):052311, DOI 10.1063/1.3422547
- Valentini F, Trávníček P, Califano F, Hellinger P, Mangeney A (2007) A hybrid-vlasov model based on the current advance method for the simulation of collisionless magnetized plasma. *Journal of Computational Physics* 225(1):753–770, DOI <https://doi.org/10.1016/j.jcp.2007.01.001>, URL <https://www.sciencedirect.com/science/article/pii/S0021999107000022>
- Valentini F, Califano F, Veltri P (2010) Two-dimensional kinetic turbulence in the solar wind. *Phys Rev Lett* 104:205002, DOI 10.1103/PhysRevLett.104.205002, URL <https://link.aps.org/doi/10.1103/PhysRevLett.104.205002>
- Valentini F, Califano F, Perrone D, Pegoraro F, Veltri P (2011a) New Ion-Wave Path in the Energy Cascade. *Physical Review Letters* 106(16):165002, DOI 10.1103/PhysRevLett.106.165002
- Valentini F, Perrone D, Veltri P (2011b) Short-wavelength Electrostatic Fluctuations in the Solar Wind. *The Astrophysical Journal* 739(1):54, DOI 10.1088/0004-637X/739/1/54
- Valentini F, Vecchio A, Donato S, Carbone V, Briand C, Bougeret J, Veltri P (2014) The Nonlinear and Nonlocal Link between Macroscopic Alfvénic and Microscopic Electrostatic Scales in the Solar Wind. *The Astrophysical Journal Letters* 788(1):L16, DOI 10.1088/2041-8205/788/1/L16

- Valentini F, Perrone D, Stabile S, Pezzi O, Servidio S, De Marco R, Marcucci F, Bruno R, Lavraud B, De Keyser J, Consolini G, Brienza D, Sorriso-Valvo L, Retinò A, Vaivads A, Salatti M, Veltri P (2016) Differential kinetic dynamics and heating of ions in the turbulent solar wind. *New Journal of Physics* 18(12):125001, DOI 10.1088/1367-2630/18/12/125001, [1611.04802](https://doi.org/10.1088/1367-2630/18/12/125001)
- van Leer B (1977) Towards the Ultimate Conservative Difference Scheme. IV. A New Approach to Numerical Convection. *Journal of Computational Physics* 23:276, DOI 10.1016/0021-9991(77)90095-X
- Varney R, Wiltberger M, Zhang B, Lotko W, Lyon J (2016) Influence of ion outflow in coupled geospace simulations: 1. physics-based ion outflow model development and sensitivity study. *Journal of Geophysical Research: Space Physics* 121(10):9671–9687
- Vasyliunas VM (1970) Mathematical models of magnetospheric convection and its coupling to the ionosphere. In: *Particles and Fields in the Magnetosphere: Proceedings of a Symposium Organized by the Summer Advanced Study Institute, Held at the University of California, Santa Barbara, Calif., August 4–15, 1969*, Springer, pp 60–71
- Vasyliunas VM (1975) Theoretical models of magnetic field line merging, 1. *Rev Geophys* 13(1):303
- Vega C, Roytershteyn V, Delzanno GL, Boldyrev S (2020) Electron-only Reconnection in Kinetic-Alfvén Turbulence. *The Astrophysical Journal Letters* 893(1):L10, DOI 10.3847/2041-8213/ab7eba
- Villasenor J, Bunemann O (1992) Rigorous charge conservation for local electromagnetic field solvers. *Computer Physics Communication* 63:306
- von Althaus S, Pokhotelov D, Kempf Y, Hoilijoki S, Honkonen I, Sandroos A, Palmroth M (2014) Vlasiator: First global hybrid-vlasov simulations of earth’s foreshock and magnetosheath. *Journal of Atmospheric and Solar-Terrestrial Physics* 120:24–35, DOI <https://doi.org/10.1016/j.jastp.2014.08.012>, URL <https://www.sciencedirect.com/science/article/pii/S1364682614001916>
- Wang CP, Wang X, Liu TZ, Lin Y (2020a) Evolution of a foreshock bubble in the midtail foreshock and impact on the magnetopause: 3-d global hybrid simulation. *Geophysical Research Letters* 47(22):e2020GL089844
- Wang H, Lin Y, Wang X, Guo Z (2019) Generation of kinetic alfvén waves in day-side magnetopause reconnection: A 3-d global-scale hybrid simulation. *Physics of Plasmas* 26(7):072102
- Wang L, Germaschewski K, Hakim A, Dong C, Raeder J, Bhattacharjee A (2018) Electron physics in 3-d two-fluid 10-moment modeling of ganymede’s magnetosphere. *Journal of Geophysical Research: Space Physics* 123(4):2815–2830, DOI <https://doi.org/10.1002/2017JA024761>
- Wang R, Lu Q, Lu S, Russell CT, Burch JL, Gershman DJ, Gonzalez W, Wang S (2020b) Physical Implication of Two Types of Reconnection Electron Diffusion Regions With and Without Ion-Coupling in the Magnetotail Current Sheet. *Geophysical Research Letters* 47(21):e2020GL088761, DOI 10.1029/2020GL088761
- Wang X, Bhattacharjee A (1993) Nonlinear dynamics of the $m = 1$ instability and fast sawtooth collapse in high-temperature plasmas. *Phys Rev Lett* 70(11):1627–1630

- Wang X, Lin Y, Chang SW (2009) Hybrid simulation of foreshock waves and ion spectra and their linkage to cusp energetic ions. *Journal of Geophysical Research: Space Physics* 114(A6)
- Wang X, Chen Y, Toth G (2022a) Global magnetohydrodynamic magnetosphere simulation with an adaptively embedded particle-in-cell model. *J Geophys Res* 127:e2021JA030091, DOI 10.1029/2021JA030091
- Wang X, Chen Y, Tóth G (2022b) Global magnetohydrodynamic magnetosphere simulation with an adaptively embedded particle-in-cell model. *Journal of Geophysical Research: Space Physics* 127(8):e2021JA030091
- Wang X, Chen Y, Toth G (2022c) Simulation of magnetospheric sawtooth oscillations: the role of kinetic reconnection in the magnetotail. *Geophys Res Lett* 49:e2022GL099638, DOI 10.1029/2022GL099638
- Wang X, Chen Y, Tóth G (2022d) Simulation of Magnetospheric Sawtooth Oscillations: The Role of Kinetic Reconnection in the Magnetotail. *Geophysical Research Letters* 49(15):e2022GL099638, DOI 10.1029/2022GL099638
- Warmuth A, Mann G (2016) Constraints on energy release in solar flares from rhesi and goes x-ray observations-ii. energetics and energy partition. *Astronomy & Astrophysics* 588:A116
- Weimer D (1996) A flexible, IMF dependent model of high-latitude electric potential having "space weather" applications. *Geophys Res Lett* 23:2549
- Weimer D (2001) An improved model of ionospheric electric potentials including substorm perturbations and application to the Geospace Environment Modeling November 24, 1996, event. *J Geophys Res* 106:407
- Wiegmann T, Büchner J (2001) Evolution of magnetic helicity in the course of kinetic magnetic reconnection. *Nonlinear Processes in Geophysics* 8(3):127–140, DOI 10.5194/npg-8-127-2001, URL <https://npg.copernicus.org/articles/8/127/2001/>
- Wilder FD, Ergun RE, Burch JL, Ahmadi N, Eriksson S, Phan TD, Goodrich KA, Shuster J, Rager AC, Torbert RB, Giles BL, Strangeway RJ, Plaschke F, Magnes W, Lindqvist PA, Khotyaintsev YV (2018) The Role of the Parallel Electric Field in Electron-Scale Dissipation at Reconnecting Currents in the Magnetosheath. *Journal of Geophysical Research: Space Physics* 123(8):6533–6547, DOI 10.1029/2018JA025529
- Wiltberger M, Merkin V, Lyon J, Ohtani S (2015) High-resolution global magnetohydrodynamic simulation of bursty bulk flows. *Journal of Geophysical Research: Space Physics* 120(6):4555–4566
- Wiltberger M, Merkin V, Zhang B, Toffoletto F, Oppenheim M, Wang W, Lyon J, Liu J, Dimant Y, Sitnov M, et al. (2017) Effects of electrojet turbulence on a magnetosphere-ionosphere simulation of a geomagnetic storm. *Journal of Geophysical Research: Space Physics* 122(5):5008–5027
- Winglee RM (submitted, 2004) Ion cyclotron and heavy ion effects on reconnection in a global magnetotail. *J Geophys Res*
- Winske D, Yin L, Omidi N, Karimabadi H, Quest K (2003) Hybrid simulation codes: Past, present and future - a tutorial. In: Büchner J, Scholer M, Dum CT (eds) *Space Plasma Simulation, Lecture Notes in Physics*, vol 615, Springer Berlin Heidelberg, Berlin, Heidelberg, pp 136–165, DOI 10.1007/3-540-36530-3_8, URL https://doi.org/10.1007/3-540-36530-3_8

[org/10.1007/3-540-36530-3_8](https://doi.org/10.1007/3-540-36530-3_8)

- Wolf R (1983) The quasi-static (slow-flow) region of the magnetosphere. In: *Solar-Terrestrial Physics: Principles and Theoretical Foundations Based Upon the Proceedings of the Theory Institute Held at Boston College, August 9–26, 1982*, Springer, pp 303–368
- Wolf R, Spiro R, Sazykin S, Toffoletto F, Yang J (2016) Forty-seven years of the rice convection model. *Magnetosphere-ionosphere coupling in the solar system* pp 215–225
- Wolf RA, Harel M, Spiro RW, Voigt G, Reiff PH, Chen CK (1982) Computer simulation of inner magnetospheric dynamics for the magnetic storm of July 29, 1977. *J Geophys Res* 87:5949–5962, DOI 10.1029/JA087iA08p05949
- Wu P, Wan M, Matthaeus WH, Shay MA, Swisdak M (2013) von kármán energy decay and heating of protons and electrons in a kinetic turbulent plasma. *Physical Review Letters* 111:121105
- Yamada M, Levinton FM, Pomphrey N, Budny R, Manickam J, Nagayama Y (1994) Investigation of magnetic reconnection during a sawtooth crash in a high-temperature tokamak plasma. *Phys Plasmas* 1:3269–3276
- Yang J, Toffoletto FR, Wolf RA (2014a) Rcm-e simulation of a thin arc preceded by a north-south-aligned auroral streamer. *Geophysical Research Letters* 41(8):2695–2701
- Yang J, Wolf RA, Toffoletto FR, Sazykin S, Wang CP (2014b) Rcm-e simulation of bimodal transport in the plasma sheet. *Geophysical Research Letters* 41(6):1817–1822
- Yang J, Toffoletto FR, Wolf RA, Sazykin S (2015) On the contribution of plasma sheet bubbles to the storm time ring current. *Journal of Geophysical Research: Space Physics* 120(9):7416–7432
- Yang J, Toffoletto FR, Wolf RA (2016) Comparison study of ring current simulations with and without bubble injections. *Journal of Geophysical Research: Space Physics* 121(1):374–379
- Yang J, Wolf R, Toffoletto F, Sazykin S, Wang W, Cui J (2019) The inertialized rice convection model. *Journal of Geophysical Research: Space Physics* 124(12):10294–10317
- Yee K (1966) Numerical solution of initial boundary value problems involving maxwell's equations in isotropic media. *IEEE Transactions on Antennas and Propagation* 14:302
- Yi Y, Zhou M, Song L, Pang Y, Deng X (2022) Electron-Only Magnetic Reconnection: Lessons Learned From Magnetic Island Coalescence. *Geophysical Research Letters* 49(6):e2022GL098124, DOI 10.1029/2022GL098124
- Yin Z, Drake J, Swisdak M (2024) A computational model for ion and electron energization during macroscale magnetic reconnection. *arXiv preprint arXiv:240114500*
- Zaharia S, Cheng C, Johnson JR (2000) Particle transport and energization associated with substorms. *Journal of Geophysical Research: Space Physics* 105(A8):18741–18752
- Zaharia S, Jordanova V, Thomsen M, Reeves G (2006a) Self-consistent modeling of magnetic fields and plasmas in the inner magnetosphere: Application to a

- geomagnetic storm. *Journal of Geophysical Research: Space Physics* 111(A11)
- Zaharia S, Jordanova VK, Thomsen MF, Reeves GD (2006b) Self-consistent modeling of magnetic fields and plasmas in the inner magnetosphere: Application to a geomagnetic storm. *J Geophys Res* 111:A11S14, DOI 10.1029/2006JA011619
- Zalesak ST (1979) Fully multidimensional flux-corrected transport algorithms for fluids. *J Comput Phys* 31:335
- Zalesak ST (1981) High order “zip” differencing of convective terms. *Journal of Computational Physics* 40(2):497–508, DOI [https://doi.org/10.1016/0021-9991\(81\)90225-4](https://doi.org/10.1016/0021-9991(81)90225-4), URL <https://www.sciencedirect.com/science/article/pii/0021999181902254>
- Zeiler A, Biskamp D, Drake JF, Rogers BN, Shay MA, Scholer M (2002) Three-dimensional particle simulations of collisionless magnetic reconnection. *J Geophys Res* 107(A9):1230, DOI 10.1029/2001JA000287
- Zenitani S, Umeda T (2014) Some remarks on the diffusion regions in magnetic reconnection. *Physics of Plasmas* 21(3):034503, DOI 10.1063/1.4869717
- Zerroukat M, Allen T (2012) A three-dimensional monotone and conservative semi-Lagrangian scheme (SLICE-3D) for transport problems. *Quarterly Journal of the Royal Meteorological Society* 138(667):1640–1651, DOI 10.1002/qj.1902
- Zhang B, Sorathia KA, Lyon JG, Merkin VG, Garretson JS, Wiltberger M (2019) Gamera: A three-dimensional finite-volume mhd solver for non-orthogonal curvilinear geometries. *The Astrophysical Journal Supplement Series* 244(1):20
- Zhang B, Brambles OJ, Lotko W, Lyon JG (2020) Is nightside outflow required to induce magnetospheric sawtooth oscillations. *Geophysical Research Letters* 47(6):e2019GL086419
- Zhang Q, Guo F, Daughton W, Li H, Li X (2021) Efficient nonthermal ion and electron acceleration enabled by the flux-rope kink instability in 3d nonrelativistic magnetic reconnection. *Physical Review Letters* 127(18):185101
- Zhong ZH, Tang RX, Zhou M, Deng XH, Pang Y, Paterson WR, Giles BL, Burch JL, Tobert RB, Ergun RE, Khotyaintsev YV, Lindquist PA (2018) Evidence for Secondary Flux Rope Generated by the Electron Kelvin-Helmholtz Instability in a Magnetic Reconnection Diffusion Region. *Physical Review Letters* 120(7):075101, DOI 10.1103/PhysRevLett.120.075101
- Zhong ZH, Zhou M, Liu YH, Deng XH, Tang RX, Graham DB, Song LJ, Man HY, Pang Y, Khotyaintsev YV (2022) Stacked Electron Diffusion Regions and Electron Kelvin-Helmholtz Vortices within the Ion Diffusion Region of Collisionless Magnetic Reconnection. *The Astrophysical Journal Letters* 926(2):L27, DOI 10.3847/2041-8213/ac4dee
- Zhou H, Tóth G, Jia X, Chen Y, Markidis S (2019) Embedded Kinetic Simulation of Ganymede’s Magnetosphere: Improvements and Inferences. *Journal of Geophysical Research: Space Physics* 124(7):5441–5460, DOI 10.1029/2019JA026643
- Zhou H, Tóth G, Jia X, Chen Y (2020) Reconnection-Driven Dynamics at Ganymede’s Upstream Magnetosphere: 3-D Global Hall MHD and MHD-EPIC Simulations. *Journal of Geophysical Research: Space Physics* 125(8):e2020JA028162, DOI 10.1029/2020JA028162

- Zhou M, Man HY, Deng XH, Pang Y, Khotyaintsev Y, Lapenta G, Yi YY, Zhong ZH, Ma WQ (2021) Observations of Secondary Magnetic Reconnection in the Turbulent Reconnection Outflow. *Geophysical Research Letters* 48(4):e2020GL091215, DOI 10.1029/2020GL091215
- Zhu Z, Winglee RM (1996) Tearing instability, flux ropes, and the kinetic current sheet kink instability in the earth's magnetotail: A three-dimensional perspective from particle simulations. *Journal of Geophysical Research: Space Physics* 101(A12):4885–4897
- Zocco A, Chacón L, Simakov AN (2009) Current sheet bifurcation and collapse in electron magnetohydrodynamics. *Physics of Plasmas* 16(11):110703, DOI 10.1063/1.3264102